DEVELOPMENT OF CRYSTAL PLASTICITY MODELS IN A THERMOMECHANICAL VARIATIONAL FRAMEWORK FOR MAGNESIUM ALLOYS

by
Necdet Ali Özdür
B.S., Mechanical Engineering, Boğaziçi University, 2016
M.S., Mechanical Engineering, Boğaziçi University, 2019

Submitted to the Institute for Graduate Studies in
Science and Engineering in partial fulfillment of
the requirements for the degree of
Doctor of Philosophy

Graduate Program in Mechanical Engineering
Boğaziçi University
2025

ACKNOWLEDGEMENTS

As I approach the completion of this thesis, I am reminded that I am nearing the end of my academic journey as a student. The transition from student to earning the title "doctor" has long seemed like a distant milestone. Now, as this goal becomes a reality, I find myself reflecting on this significant academic achievement with both anticipation and gratitude for the journey that has brought me to this point.

In making this a reality, first and foremost, I would like to express my deepest gratitude to my beloved wife, Gizem, for her unwavering support and encouragement throughout this long academic journey. As my PhD extended into its sixth year, her patience, understanding, and constant presence made even the most challenging moments endurable. Even during the toughest times, she remained my steadfast source of strength and comfort. Her love, encouragement, and belief in me have been the driving force behind my perseverance and ultimate achievements. I am profoundly grateful for her being there for me every step of the way, and I cannot imagine having completed this work without her by my side.

My sincere thanks go to my thesis supervisor, Prof. C. Can Aydıner, for considering me qualified and offering me the opportunity to be part of this project. Through his generous invitation, I was introduced to Prof. Laurent Stainier, who, although not officially my supervisor, proved to be as attentive and involved as any supervisor and advisor could be throughout the entirety of my work on this thesis. I am immensely grateful for their invaluable guidance, mentorship, and the enriching scientific discussions that have shaped both this research and my development as a scholar. I deeply appreciate how they introduced me to new, timely, and exciting fields of mechanics that have broadened my perspective and opened up fascinating avenues of research that I would never have encountered otherwise. I also appreciate the contributions of Dr. Rian Seghir, as well as the other members of my jury—Prof. Günay Anlaş, Assoc. Prof. Ali Özgün Konca, and Prof. Demirkan Çöker—for their valuable comments and suggestions.

I want to express my deepest gratitude to my colleagues in the Mechanics of Advanced Materials lab, both past and present: Dr. Enver Kapan, Dr. Olcay Türkoğlu, Dr. Nima Şafak, İbrahim Buğra Üçel, Hasan Can Kubat, Sefer Can Erman, and Batuhan Kal. Their camaraderie and friendship provided essential support during demanding periods and made collaborative work both productive and enjoyable. My gratitude also goes to all assistants in the Mechanical Engineering department for their invaluable friendship and support throughout my studies.

Finally, I offer my heartfelt gratitude to my family for their constant love and support. Their belief in me has been a source of motivation and strength, sustaining me through the challenges of this academic endeavor.

This work was supported by the Scientific and Technological Research Council of Turkey (TÜBİTAK) [grant number 120N722]. I also acknowledge the funding from Campus France (Programme Bosphore) [grant number 46626ZM].

ABSTRACT

DEVELOPMENT OF CRYSTAL PLASTICITY MODELS IN A THERMOMECHANICAL VARIATIONAL FRAMEWORK FOR MAGNESIUM ALLOYS

This thesis addresses the critical challenge of accurately modeling the complex behavior of magnesium alloys, whose highly anisotropic deformation is dominated by profuse twinning. The primary objective is to develop a thermodynamically consistent crystal plasticity model for magnesium that captures both mechanical and energy dissipation characteristics during plastic deformation, particularly twinning, and validate the model jointly by thermal–mechanical data. Experimentally, simultaneous stress, strain, and in-situ thermal measurements are employed during uniaxial testing of both single crystal and polycrystalline magnesium specimens using combined infrared thermography and digital image correlation. Key findings demonstrate that deformation mechanisms in magnesium possess distinct energetic signatures, with quantified energy dissipation providing physically-based benchmarks for model validation. Theoretically, a thermomechanically coupled crystal plasticity model incorporating slip and twinning mechanisms is developed within a variational framework, ensuring energetic consistency. The variational approach enables prediction of energy partitioning during plastic deformation, opening an additional verification channel. Model verification effort reveals that the commonly employed power-law rate dependency is unable to represent full range of thermomechanical behavior, necessitating the addition of rate-independent terms. This work advances the field by establishing a rigorous validation protocol using thermal measurements as independent verification and represents a significant idea toward truly predictive multi-physics material models.

ÖZET

MAGNEZYUM ALAŞIMLARI İÇİN TERMOMEKANİK VARYASYONEL ÇERÇEVEDE KRİSTAL PLASTİSİTE MODELLERİNİN GELİŞTİRİLMESİ

Bu tez, ikizlenmenin baskın olduğu, yüksek oranda anizotropik şekil değiştirme davranışı sergileyen magnezyum alaşımlarının karmaşık davranışlarının modellenmesini ele almaktadır. Temel amaç, magnezyumun plastik şekil değiştirme (özellikle ikizlenme) sırasında hem mekanik tepkisini hem de enerji dağılımını doğru bir şekilde yansıtan, termodinamik açıdan tutarlı bir kristal plastisite modeli geliştirmek ve bu modeli mekanik–ısıl verilerle eş zamanlı doğrulamaktır. Deneysel açıdan, tek ve çok kristalli magnezyum numuneler üzerinde yükleme testleri gerçekleştirilirken, kızılötesi termografi ve dijital imge korelasyonu yöntemleriyle eşzamanlı gerilme, şekil değiştirme ve yerinde sıcaklık ölçümleri yapılmıştır. Elde edilen bulgular, magnezyumdaki şekil değiştirme mekanizmalarının kendilerine özgü enerjik izler taşıdığını ortaya koymakta; hesaplanan ısı yayılımı değerleri ise model doğrulaması için fiziksel temelli güvenilir ölçütler sunmaktadır. Kuramsal düzlemde ise, kayma ve ikizlenme mekanizmalarını içeren ve termomekanik olarak bağlanmış bir kristal plastisite modeli, enerjik tutarlılığı sağlayan varyasyonel bir çerçevede geliştirilmiştir. Varyasyonel yaklaşım, plastik şekil değiştirme sürecinde enerjinin nasıl paylaştırıldığını öngörmeyi mümkün kılarak, modele ilave bir doğrulama kanalı açmaktadır. Model doğrulama çabaları, yükleme hızına bağımlı plastisitede yaygın kullanılan kuvvet fonksiyonunun, magnezyumun termomekanik davranışını tümden temsil edemediğini ve modele yükleme hızından bağımsız plastik terimlerinin eklenmesinin gerekli olduğunu göstermiştir. Bu çalışma, ısıl ölçümleri bağımsız bir teyit aracı olarak kullanan titiz bir doğrulama protokolü ortaya koyarak, çok-fizikli malzeme modellerinin öngörü gücünü temelden artırabilecek bir fikir sunmaktadır.

TABLE OF CONTENTS

ACKNOWLEDGEMENTS iii
ABSTRACT v
ÖZET vi
LIST OF FIGURES x
LIST OF TABLES xiv
LIST OF SYMBOLS xv
LIST OF ACRONYMS/ABBREVIATIONS xviii
1. INTRODUCTION 1
1.1. Motivation 1
1.2. Aim and Scope 5
1.3. Thesis Structure 7
2. LITERATURE REVIEW 9
2.1. Mechanical Properties and Behavior of Magnesium 9
2.1.1. Multiscale Deformation Measurement with DIC 10
2.2. Modeling Efforts for Magnesium Alloys 12
2.2.1. Variational Crystal Plasticity Models 13
2.2.2. Model Validation for Magnesium Alloys 14
2.2.3. Length Scale in Crystal Plasticity Models 15
2.2.3.1. Mean-Field Models 15
2.2.3.2. Full-Field Models 16
2.2.4. Implementation of Deformation Twinning 17
2.3. In-situ Temperature Measurements of Deforming Structures 18
2.3.1. Thermal Measurement of Magnesium 20
3. METHODOLOGY 22
3.1. Theoretical Framework 22
3.1.1. Kinematic Description 22
3.1.2. Constitutive Model 25
3.2. Numerical Implementation 28

3.2.1. Inner Problem: Variational Constitutive Updates 29
3.2.1.1. Projected Gradient Method 31
3.2.1.2. Twinning–Detwinning–Retwinning 32
3.2.2. Outer Problem: Equilibration of the System 34
3.2.2.1. Root-finding Problem 34
3.2.3. Interaction Model for Polycrystal Simulations 35
3.3. Experimental 37
3.3.1. Experimental Setup 37
3.3.2. Sample Preparation 39
3.3.2.1. Magnesium AZ31 39
3.3.2.2. Single Crystal Magnesium 40
3.3.3. IRT Experiment Procedure 41
3.3.3.1. Polycrystalline Compression–Tension Tests 41
3.3.3.2. Single Crystal Compression Tests 44
3.3.4. Processing of Experimental Data 45
3.4. Parameter Calibration and Model Validation 46
4. RESULTS 51
4.1. Polycrystalline Mg AZ31 Compression–Tension Experiments 51
4.2. Pure Magnesium Single Crystal Compression Results 54
4.3. Model Validation by Crystal Plasticity Simulations 59
4.3.1. Pure Mg Single Crystal Simulations 60
4.3.2. Mg AZ31 Polycrystal Simulation 67
5. DISCUSSION 75
5.1. Merits, Dependencies, and Features of the Experimental Data 75
5.2. The Importance of Energetic Characterization of Twinning 77
5.3. Reflections on the Magnesium Crystal Plasticity Model 79
5.3.1. Thermomechanical Consistency through Variational Framework . 80
5.3.2. Adaptations and Future Directions for Dissipation Modeling . . 81
5.3.3. Limitations in Modeling Latent Hardening Effects 82
5.3.4. Implications of Taylor Approximation in Polycrystal Simulations 83
6. CONCLUSION 86

6.1. Contributions to the Field 87
6.2. Limitations of the Study 88
6.3. Future Work 88
6.4. Concluding Remarks 89
REFERENCES 90
APPENDIX A: THE 0D HEAT EQUATION 109
APPENDIX B: COPYRIGHTS 113

LIST OF FIGURES

Figure 1.1. Depiction of (a) HCP unit cell with its crystallographic axes, (b) basal $\{0001\}\langle 11\bar{2}0\rangle$ and prismatic $\{10\bar{1}0\}\langle 11\bar{2}0\rangle$, (c) $\langle c+a\rangle$ pyramidal $\{11\bar{2}2\}\langle\bar{1}\bar{1}23\rangle$ slip systems over the hexagonal unit cell of magnesium. (d) Similar depiction of the most commonly observed $\{10\bar{1}2\}\langle\bar{1}011\rangle$ tensile twin mechanism. 2

Figure 3.1. Experimental setup for in situ infrared thermography measurements: (a) macro-DIC imaging line; (b) thermal camera; (c) micro-DIC imaging line (not used here but historically relevant, see text); (d) tension-compression loading frame; (e) X–Y–Z positioning stages; (f) outside view of the entire setup covered with an opaque curtain that sits on a vibration isolation table. 38

Figure 3.2. Modified setup for single crystal Mg compression tests. (a) is a stress-free piece of Mg, attached to a copper strip; (b) are the glass disks that insulate the sample from the tension–compression module. White lithium grease is applied to the glass surface to prevent friction. (c) is the single crystal specimen. 39

Figure 3.3. (a, b) IRT and DIC-camera images of Mg AZ31 sample A, with red and green boxes indicating gage and temperature averaging regions, respectively. (c) Cyclic stress–strain curve showing ramp loading (compression, tension) and embedded axial DIC-strain maps at cycle endpoints. (d) Sample mean gage temperature over time, baselined by dummy sample temperature and filtered. 42

Figure 3.4. Stress versus strain on consecutive compression-tension cycles with live-DIC experimentation. The third (time) axis is inserted to distinguish individual cycles. 43

Figure 3.5. Pole figure of the polycrystal orientation distribution used in the simulations. RD is aligned with the loading axis. 46

Figure 3.6. (a), (c) Stress vs strain and (b), (d) β vs plastic strain curves demonstrating the affect of different material parameters. 48

Figure 4.1. Stress and average temperature measurements plotted against average strain for samples A and B over load ramps (A0, B0, A1, B1) defined in Figure 3.3c. Stress plots over (a) A0, B0, (b) A1, B1; temperature plots over (c) A0, B0, (d) A1, B1. (e) exponential fit of temperature decay following the end of the load ramp A0 marked with a '$\times$' sign. 52

Figure 4.2. Energy balance terms (Eq. 3.37) for (a) compression (A0, B0), and (b) tension (A1, B1) load ramps. Taylor–Quinney coefficients for (a) compression (A0, B0), and (b) tension (A1, B1). 53

Figure 4.3. (a) Load direction (blue arrows) and observation angle (orange disk) with respect to the crystal, (b) macro-DIC image, (c) macro-DIC strain fields of the $c^{\parallel}$ single-crystal compression sample. 55

Figure 4.4. (a) Load direction (blue arrows) and observation angle (orange disk) with respect to the crystal, (b) macro-DIC image, (c) macro-DIC strain fields of the $c^{\perp}$ single-crystal compression sample. 56

Figure 4.5. Stress and average temperature measurements plotted against average strain for samples $c^{\perp}$ and $c^{\parallel}$. (a), (b) stress–strain and temperature–strain curves for $c^{\perp}$; (c), (d) stress–strain and temperature–strain curves for $c^{\parallel}$. 57

Figure 4.6. Temperature processing of (a) $c^{\perp}$, (b) $c^{\parallel}$ single-crystal compression tests. 58

Figure 4.7. Energy balance terms (Eq. 3.37) for single crystal compression tests: (a) $c^{\perp}$ sample, (b) $c^{\parallel}$ sample. Taylor–Quinney coefficients for (c) $c^{\perp}$ sample, (d) $c^{\parallel}$ sample. (e) shows a zoomed-in view of the energy terms during the twin plateau of the $c^{\perp}$ sample. 59

Figure 4.8. Single-crystal simulation results using parameters adapted from Chang and Kochmann [33]. Stress–strain, β, and activity rate plots (a), (c), (e) for $c^{\perp}$; and (b), (d), (f) for $c^{\parallel}$ samples. 60

Figure 4.9. Single-crystal simulation results with VD dissipation model using parameters calibrated to stress only (blue); and both stress and β (green). Stress–strain and β plots (a), (c) for $c^{\perp}$ and (b), (d) for $c^{\parallel}$ samples. 62

Figure 4.10. Single-crystal simulation results with VD+PD model. Stress–strain, β, and activity rate plots (a), (c), (e) for $c^{\perp}$ and (b), (d), (f) for $c^{\parallel}$ samples. Activity rates are color coded to match the slip/twin system depictions in Figure 1.1. 64

Figure 4.11. Twin volume fraction evolution from $c^{\perp}$ simulation. 65

Figure 4.12. Temperature variations from single crystal compression simulations. (a) $c^{\perp}$ sample, (b) $c^{\parallel}$ sample. 66

Figure 4.13. Apparent Poisson's ratio from single crystal compression simulations. (a) $c^{\perp}$ sample, (b) $c^{\parallel}$ sample. 67

Figure 4.14. Polycrystal simulation results for Mg AZ31 sample A. (a) Stress–strain; (b) and (c) are β evolution, (d) and (e) are activity rates for compression (A0) and tension (A1) load segments. Activity rates are color coded to match the slip/twin system depictions in Figure 1.1. 70

Figure 4.15. Per-grain β values at the end of (a) compression ramp; (b) tension ramp, shown on the pole figure of the Mg AZ31 polycrystal simulation. 71

Figure 4.16. Temperature variation curves of Mg AZ31 polycrystal simulation for (a) compression (A0) and (b) tension (A1) load segments. . . . 72

Figure 4.17. Apparent Poisson's ratio for Mg AZ31 polycrystal simulation for (a) compression (A0) and (b) tension (A1) load segments. 73

Figure 5.1. A multi-sample comparison of thermal data over the initial twin plateau for four samples A–D, coupled with the DIC-determined strain patterns at the end point of the experiments. A, B (previously considered) and C are loaded up to 2% average compressive strain whereas D is loaded up to 2.6%. 76

LIST OF TABLES

Table 3.1. Elastic and thermal properties utilized for pure magnesium [a] [120], [b] [121] and for magnesium AZ31 [c] [122], [d] [123]. 45

Table 4.1. Parameter sets used in the single crystal simulations with the VD model. 61

Table 4.2. Refined parameters for single crystal simulations with VD+PD model. 63

Table 4.3. Parameter set used in the Mg AZ31 polycrystal simulation. 68

LIST OF SYMBOLS

$\boldsymbol{a}^{(\beta)}$	Shear direction for twinning system β
$\mathcal{A}$	Interaction matrix
C	Heat capacity
$\mathbb{C}$	Elastic stiffness tensor
D	Rate potential
$\mathcal{D}$	Total dissipation
$\mathcal{D}_{\text{int}}$	Intrinsic (mechanical) dissipation
$\mathcal{D}_{\text{the}}$	Thermal dissipation
E	Young's modulus
h	Heat exchange coefficient
$h^{(\alpha)}$	Hardening modulus for slip system α
$\mathcal{H}$	Latent hardening matrix for slip systems
$k^{(\beta)}$	Self-hardening parameter for twin system β
k	Thermal conductivity
$\mathcal{K}$	Latent hardening matrix for twin systems
$\boldsymbol{m}^{(\alpha)}$	Slip plane normal vector for slip system α
m	Rate dependency exponent
$\boldsymbol{M}^{(\,\cdot\,)}$	Symmetric Schmid tensor
$\boldsymbol{n}^{(\beta)}$	Twin plane normal vector for twinning system β
$\boldsymbol{q}$	Heat flux vector
$\boldsymbol{Q}^{(\beta)}$	Reflection operation for twin system β
r	Volumetric heat supply
$\boldsymbol{r}$	Residual vector
$\boldsymbol{s}^{(\alpha)}$	Slip direction vector for slip system α
t	Time
T	Absolute temperature
T_0	Reference temperature
T_{ext}	External temperature

U	Internal energy density potential
W_a	Applied plastic work rate
W_b	Stored energy rate
W_d	Dissipated energy rate
W_l	Heat loss rate
W_s	Heat storage rate
W_{the}	Thermoelastic coupling term
$\mathcal{W}$	Incremental potential
$\boldsymbol{Y}$	Thermodynamic forces conjugate to internal variables
$\boldsymbol{Z}$	Set of internal variables
α_{th}	Thermal expansion coefficient
(α)	Slip system index
β	Taylor–Quinney coefficient
(β)	Twin system index
γ_{tw}	Characteristic shear of twinning
$\gamma^{(\alpha)}$	Slip shear on slip system α
$\dot{\gamma}^{(\alpha)}$	Slip rate on slip system α
$\dot{\gamma}_0^{(\alpha)}$	Reference slip rate for slip system α
$\epsilon^{(\alpha)}$	Cumulated slip shear on slip system α
$\boldsymbol{\varepsilon}$	Total strain tensor
$\boldsymbol{\varepsilon}_{\text{el}}$	Elastic strain tensor
$\boldsymbol{\varepsilon}_{\text{pl}}$	Plastic strain tensor
$\boldsymbol{\varepsilon}_{\text{sl}}$	Slip strain tensor
$\boldsymbol{\varepsilon}_{\text{tw}}$	Twin strain tensor
η	Specific entropy
θ	Temperature variation
κ	Bulk modulus
λ	Lamé parameter
$\lambda^{(\beta)}$	Twin volume fraction for twin system β
$\dot{\lambda}^{(\beta)}$	Rate of twin volume fraction change

$\dot{\lambda}_0^{(\beta)}$	Reference twin rate for twin system β
μ	Shear modulus (Lamé parameter)
ν	Poisson's ratio
ρ	Material density
ρ_0	Reference density
$\boldsymbol{\sigma}$	Cauchy stress tensor
$\sigma_0^{(\cdot)}$	Initial yield stress
$\sigma_\infty^{(\cdot)}$	Saturation yield stress
$\tau_0^{(\cdot)}$	Reference stress
τ_{eq}	Time constant for heat losses
χ	c/a ratio of hexagonal unit cell
ϕ^*	Dual form of dissipation pseudo-potential
ϕ_{sl}^*	Slip dissipation potential
ϕ_{tw}^*	Twin dissipation potential
ψ	Helmholtz free-energy density potential
ψ_{el}	Elastic part of free-energy density
ψ_{pl}	Plastic part of free-energy density
ψ_{sl}	Slip part of plastic free-energy density
ψ_{tw}	Twin part of plastic free-energy density
ψ_{th}	Thermal free-energy density

LIST OF ACRONYMS/ABBREVIATIONS

0D	Zero Dimensional
2D	Two Dimensional
CG	Composite Grain
CP	Crystal Plasticity
CPFE	Crystal Plasticity Finite Element
CRSS	Critical Resolved Shear Stress
DIC	Digital Image Correlation
DT	Detwinning
EBSD	Electron Backscatter Diffraction
EDM	Electrical Discharge Machining
EVPSC	Elastic-Viscoplastic Self-Consistent
FEM	Finite Element Method
FFT	Fast Fourier Transform
GND	Geometrically Necessary Dislocations
HCP	Hexagonal Close-Packed
IBVP	Initial Boundary Value Problem
IR	Infrared
IRT	Infrared Thermography
ND	Normal Direction
OM	Optical Microscopy
PD	Plastic Dissipation
PS	Plastic Storage
PTR	Predominant Twin Reorientation
RD	Rolling Direction
RSS	Resolved Shear Stress
RVE	Representative Volume Element
SEM	Scanning Electron Microscopy
SP	Slip Plasticity

TD	Transverse Direction
TR	Transition Region
VD	Viscous Dissipation
VF	Volume Fraction
XRD	X-Ray Diffraction

1. INTRODUCTION

This study considers the combined mechanical and thermal (energetic) responses of lightweight magnesium alloys under mechanical loading, which are the least dense structural metallic materials. Their exceptional strength-to-weight ratio makes them promising candidates for various applications, particularly in the transportation sector where weight reduction is crucial for improving fuel efficiency and performance.

1.1. Motivation

Magnesium alloys offer a compelling advantage due to their low density but pose significant challenges for mechanical prediction and engineering design. The material exhibits pronounced sensitivity to loading direction in both stiffness and strength properties. This anisotropy arises from the intricate interplay of slip and twinning deformation mechanisms that govern strain accommodation at the microscale. Consequently, magnesium has garnered substantial research attention, with efforts focused on developing fundamental models to accurately capture these complex microscale deformation processes and generate reliable behavioral predictions.

The mechanical complexity primarily stems from two main factors. First, like other hexagonal close-packed (HCP) crystals (Figure 1.1a), magnesium alloys exhibit various slip system families: the commonly observed mechanisms for magnesium—basal, prismatic, and $\langle c + a \rangle$ pyramidal—are shown in Figure 1.1b, c. What uniquely distinguishes magnesium, however, is that the activation stresses for these systems differ by several orders of magnitude, with basal slip being the easiest to activate. This leads to extreme plastic anisotropy [1, 2]. In polycrystalline engineering materials, this results in significant variations in plastic compliance among grains, based solely on their crystal orientation.

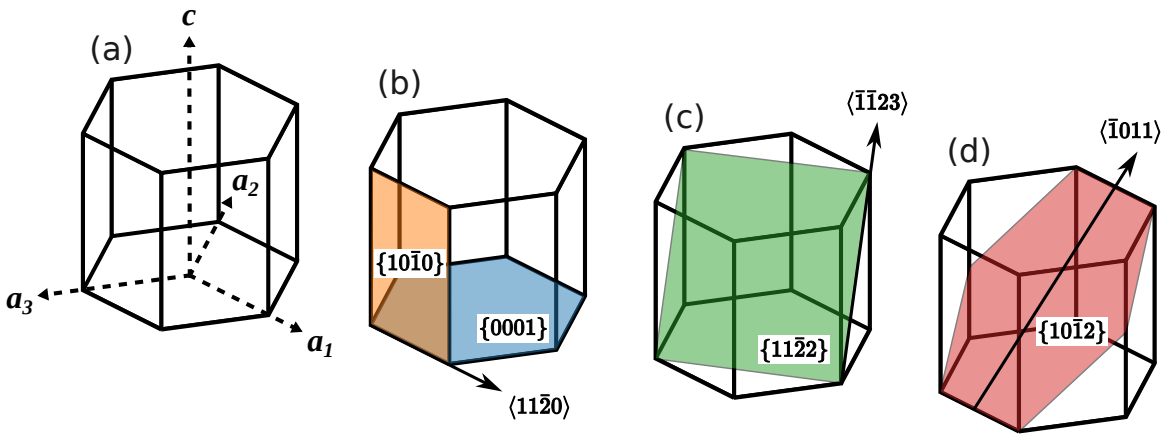


Figure 1.1. Depiction of (a) HCP unit cell with its crystallographic axes, (b) basal $\{0001\}\langle 11\bar{2}0\rangle$ and prismatic $\{10\bar{1}0\}\langle 11\bar{2}0\rangle$, (c) $\langle c+a\rangle$ pyramidal $\{11\bar{2}2\}\langle\bar{1}\bar{1}23\rangle$ slip systems over the hexagonal unit cell of magnesium. (d) Similar depiction of the most commonly observed $\{10\bar{1}2\}\langle\bar{1}011\rangle$ tensile twin mechanism.

The second factor contributing to magnesium's deformation complexity is the prevalence of mechanical twinning mechanisms [3]. Mechanical twinning is an abrupt transformation characterized by a large transformation shear and unipolar activation [4]. Simply put, if a twin system inside a particular crystallite is activated under tension, it will not be activated under compression. Tensile twinning, the most commonly observed variant in magnesium (shown in Figure 1.1d), not only represents one of the few mechanisms in magnesium that accommodates deformation along the c-axis, but also has a critical resolved shear stress (CRSS) that is inferred to be only slightly higher than that of basal slip in lightly alloyed AZ31 [5] and lower than both prismatic and pyramidal slip.

If the intricate effects of these micro-mechanisms remained confined to the crystallite scale, industrial practices could still rely on classical macroscopic continuum models, such as von Mises plasticity for isotropic materials. Though rarely explicitly stated, these classical models consider the average behavior of sufficiently large crystal neighborhoods, often called a "representative volume element" (RVE). This approach deliberately homogenizes, or discounts, the detailed activity of crystallite-scale micro-mechanisms. For cubic metals like steels and aluminum alloys, this approach is largely

adequate. Consequently, there's limited incentive for applications engineers to use crystal plasticity models, which build the response of polycrystalline bulk material from its individual crystallite building blocks [6, 7].

In contrast, magnesium alloys present a greater challenge. When the composition of slip and twin system activity shows fundamental variations with the load path, this also leads to significant variations in strength and stiffness at the component scale. For example, tensile twinning predominantly controls deformation when formed (extruded or rolled) components are compressed along their forming directions. This deformation mode occurs at very low stress and hardening levels. Conversely, the same material exhibits substantial hardening and strength under tension [8] since hard slip mechanisms are required to accommodate strain. Furthermore, the active deformation mechanisms also dictate the spatial characteristics of strain accommodation, or deformation patterning. Tensile twinning, for instance, leads to considerable strain localization in the form of banded deformation [9, 10].

Given this sharp variability in material response with micro-mechanistic roots, few material have seen as much attention as magnesium alloys with regard to crystal plasticity implementations [11–17]. Crystal plasticity defines deformation at the crystallite scale as a superposition of the activity of various slip/twin systems [18]. These models use the orientations and volume fractions of the material's constituent grains as input, enabling them to provide results at both the individual crystallite level and (through averaging) the macroscopic scale. The model therefore automatically accounts for crystallographic texture (orientation distribution). For instance, since the crystallographic textures of materials resulting from rolling, extrusion, and casting operations differ, the model does not require different constants for samples from each of these operations. Furthermore, as a fundamental scale approach that simulates the individual activity of slip/twin micro-mechanisms, the model can inherently represent load path variations.

The crystal plasticity models for magnesium have steadily improved in sophistication and realism with regard to the depiction of granular interactions as well as the adequacy of constitutive forms. Regarding the former, the initial mean-field models [12, 17] are surpassed by the more recent full-field models that consider a realistic grain neighborhood model in a finite element or spectral-solver framework [13, 16]. For the latter, deformation twinning is once more the crucial element that determines the fidelity and target length scale of a model. The incorporation assumptions for this abrupt phenomenon and the ability to account for its reversal (detwinning) are definitive elements.

An important hurdle in developing high-fidelity, physics-based models for magnesium is the large number of phenomenological constants (e.g., for each slip and twin system) that must be derived from limited experimental evidence. These constants typically appear as distinct parameter sets defining the flow behavior of each slip and twin mechanism. Available channels of experimental evidence for calibration of these numerous constants (and model validation), include average strains [1, 14, 17], stress–strain gradients [19], anisotropy ratios [20], and orientation-averaged bulk diffraction data [5, 21–28] that has resolution over certain orientation families. Moreover, numerous studies rely primarily on data from plane-strain single-crystal compression experiments by Kelley and Hosford [29], for crystal-level parameter calibration [2, 16, 30–35]. While these diverse experimental datasets provide essential benchmarks for assessing model fidelity, they also highlight the challenge of achieving robust validation across different loading scenarios and microstructural conditions. Most models are validated loosely against limited experimental data, and their performance under different or non-monotonic loading paths often remains questionable.

Current models often lack the capability to simultaneously capture both mechanical and thermal responses, thereby limiting their applicability and validation potential in realistic thermomechanical and dynamic loading scenarios. Specifically, the energy dissipation and storage during plastic deformation—particularly the fraction of plastic work dissipated versus that stored by the material—remain largely unexplored

within existing crystal plasticity frameworks for magnesium alloys. This gap is critical because different slip and twin micro-mechanisms likely exhibit distinct energetic signatures, offering valuable insights for model validation and mechanism identification. Consequently, understanding the dissipative character of these mechanisms necessitates sophisticated modeling approaches capable of simultaneously representing both mechanical and thermal responses.

The variational framework, which generalizes the principle of maximum dissipation, offers a powerful approach for simultaneously deriving internal-variable rates (in this case, these predominantly stand for the activity rates of individual micro-mechanisms) and the plastic flow direction, even in the presence of rate-sensitivity and non-Newtonian viscosity [36]. Crucially, it inherently ensures the thermodynamic consistency of internal variables by respecting thermodynamic principles and facilitating robust thermomechanical coupling [37]. This is particularly important for materials like magnesium alloys, where thermodynamic effects are often treated as secondary considerations rather than fundamental aspects of the deformation process. This indifference can lead to models that inaccurately represent the coupled nature of thermal and mechanical phenomena.

The variational framework offers substantial benefits for thermomechanical coupling, including ensuring energetic consistency and providing a systematic approach to deriving thermodynamically sound constitutive equations. Furthermore, the framework readily incorporates multi-physics effects by naturally accounting for the energetic aspects of deformation. This enables direct comparison with in situ thermal measurements, thereby delineating the dissipative character of various deformation mechanisms.

1.2. Aim and Scope

This research develops a thermodynamically consistent crystal plasticity model for magnesium alloys that strives to capture both mechanical behavior and energy dissipation characteristics of deformation. The model builds upon existing calibration practices using mechanical data while incorporating thermomechanical coupling

through a variational framework to ensure energetic consistency. The comprehensive dataset including stress, strain, and temperature measurements required to validate this thermomechanically coupled model is specifically collected as part of the body of work in this thesis, following rigorous standardization procedures to ensure high-quality, repeatable results. Accordingly, simultaneous multi-physics measurements conducted in this study over monotonic and cyclic load paths, as well as using both single crystal and polycrystalline magnesium specimens, provide a robust foundation for model calibration and validation.

The scope of this work hence encompasses two integrated components that together enable comprehensive model validation. The first experimental component focuses on generating multi-physics data across various microstructures of magnesium alloys under complex loading conditions. This experimental work incorporates in-situ thermal measurements alongside traditional mechanical data, enabling investigation of energy dissipation during deformation. The thermal data collection provides unique insights into the dissipative characteristics of slip and twin mechanisms that govern magnesium deformation, particularly quantifying the fraction of plastic work that is dissipated (or conversely stored) by the material.

The experimental validation strategy extends beyond conventional approaches by examining material response under reversed loading paths, which provides a rigorous test for model accuracy. This approach is particularly relevant for magnesium alloys that accommodate strain through extensive twin transformation, where reverse loading induces detwinning (reversal of twins) as the primary deformation mode, resulting in the idiosyncratic sigmoidal stress–strain curves during cyclic loading [8].

The second (modeling) component involves developing crystal plasticity models within a variational viscoplasticity framework [36, 38, 39] that enables direct comparison with energy dissipation characteristics beyond traditional strain field comparisons [40]. This approach to model validation through energetic response comparison with in-situ thermal data represents a significant advancement in crystal plasticity modeling

methodology. The resulting framework ensures thermodynamic consistency of the model while facilitating comprehensive validation against both mechanical and thermal experimental observations from uniaxial tests on single crystal and polycrystalline magnesium specimens.

1.3. Thesis Structure

This thesis is organized into six chapters to address the research objectives. Following this introductory chapter, Chapter 2 presents a comprehensive Literature Review. It critically examines foundational and contemporary research on magnesium alloys, focusing on their deformation mechanisms and the inherent challenges in modeling their plasticity. The chapter surveys established crystal plasticity modeling frameworks, explores the application of variational principles in non-linear plasticity, and reviews existing constitutive models specifically developed for Mg alloys. This review identifies significant gaps in the current literature, particularly concerning the accurate capture of thermomechanical coupling and temperature evolution during deformation, thereby motivating the development of the novel model proposed in this work.

Building directly upon the foundation laid in Chapter 2, Chapter 3 details the Methodology employed. It first describes the experimental approach, which integrates Infrared Thermography (IRT) and Digital Image Correlation (DIC) techniques to quantitatively measure the thermal and mechanical responses of both single-crystal and polycrystalline Mg specimens under deformation. Complementing the experimental work, the theoretical component of this chapter introduces the thermodynamically consistent variational crystal plasticity model. This section elaborates on the model's kinematic framework, constitutive equations, and numerical implementation, highlighting procedures to use the thermal dissipation as an additional physical channel for model calibration.

Chapter 4 presents the results derived from both the experimental campaign and the computational model. It begins by reporting findings from the combined IRT

and DIC experiments, which reveal strain localization patterns, temperature evolution profiles, and the quantified fraction of plastic work dissipated as heat during deformation (also known as the Taylor–Quinney coefficient [41]) for Mg alloys. The chapter then focuses on calibrating and validating the proposed variational model against the acquired experimental data. This includes detailed comparisons between predicted and measured stress–strain curves, thermal responses, and the evolution of energy partitioning. We use quantitative metrics to assess the model's accuracy in simulating critical aspects like slip system activity, hardening behavior, and thermomechanical coupling.

Chapter 5 provides a critical discussion of the novel insights gained, particularly those arising from the unique IRT data concerning adiabatic heating and strain heterogeneity in Mg alloys. It evaluates the performance of the developed variational crystal plasticity model in predicting complex multiscale thermomechanical behavior. The discussion candidly addresses the model's limitations, such as assumptions made regarding latent hardening (the increase in slip/twin resistance caused by activity from other systems) and the treatment (or simplification) of deformation twinning. Finally, it elaborates on the broader implications of the findings for experimental mechanics techniques and potential avenues for future model refinements.

Chapter 6 serves as the conclusion, synthesizing the key findings and contributions of the research. It summarizes the experimental evidence gathered on deformation-induced heating in Mg, underscores the efficacy of the variational framework in unifying plasticity and thermodynamics, and highlights the model's predictive capabilities under complex loading scenarios.

2. LITERATURE REVIEW

2.1. Mechanical Properties and Behavior of Magnesium

Magnesium alloys have garnered significant scientific interest in the field of mechanics largely due to their potential as high-specific-strength materials (strong yet low-density) and their role as a model system for studying the physics of twin transformation. Classical mechanical testing has clearly demonstrated the extraordinary load path dependence these materials exhibit, characterized by sigmoidal stress–strain curves [8, 42, 43].

Diffraction techniques have been crucial in elucidating the twinning phenomenon. This is because diffraction is resolved over orientations, and microscopically, twinning involves the abrupt formation of a material band with a vastly different orientation. For instance, in the magnesium tensile twin, the c-axis of the hexagonal unit cell is rotated by 86.6° in the twin zone. This rotation means that the signal from twinned zones becomes detectable in diffraction experiments.

Bulk diffraction techniques like neutron diffraction, which sample volumes on the order of cm^3, begin to detect a new peak corresponding to the twin families [21,23,44–46]. This detection relies on the heavy texture of the original material, which is typical for formed magnesium alloys. Both extruded rods and rolled plates of magnesium are known to have notoriously heavy textures: the extrusion texture characterized by c-axes that are perpendicular to the extrusion axis (but with polar symmetry about it) and the rolling texture imparting c-axes alignment of the grains (with the normal direction of the formed plate). More specialized diffraction techniques can focus on the volume of a single grain [47], revealing the mechanical state of the twins that form within it. A critical advantage of reciprocal space diffraction techniques is their direct probing of lattice strain (considered equivalent to the elastic strain component of total strain), which allows for the evaluation of the stress state of the measured material volume.

Another notable experimental technique sensitive to the operation of twins is acoustic emission. Twins form abruptly, a characteristic reflected in the elevated sound wave signature recorded by acoustic emission techniques [48–50]. Interestingly, detwinning (the reverse transformation) is not as abrupt as twin formation, likely due to the absence of a nucleation step [48]. Acoustic emission can typically be used as a supplementary technique, supporting measurements from methods like neutron diffraction [28] and digital image correlation [49].

2.1.1. Multiscale Deformation Measurement with DIC

Image-based determination of strain fields with high spatial resolution has become a staple in experimental mechanics in recent years. Unlike diffraction techniques, these real-space methods probe total strain. While alternatives like the grid technique [51] exist, digital image correlation (DIC) is the most common implementation for this type of measurement due to its lack of an inherent length-scale [52].

Given that magnesium alloys exhibit macroscopic strain localization, high-spatial resolution imaging is crucial for understanding how strain is accommodated across a material. Consequently, even macroscopic DIC implementations have significantly advanced our understanding of magnesium deformation [10, 49, 53]. Notably, Kapan et al. [10] demonstrated the inadequacy of relying on sample-average strains in twinning magnesium. Their study compared extruded and rolled samples, revealing drastically different kinematics of underlying deformation bands despite near-equivalent stress–strain curves under cyclic compression-tension.

Microscopic DIC measurements, both optical and electron microscopy-based, have provided the most direct insights into crystalline interactions. These measurements offer generic outcomes for metallic polycrystalline aggregates, applicable to both cubic and hexagonal metals. A network of short-range (few-to-several grains long) strain localization bands forms within the aggregate, oriented in maximum shear directions and largely following grain boundaries [54]. These bands typically initiate around

triple points, and intense strain heterogeneity is observed inside the grains. These measurements thus highlight the critical role of nearest-neighbor strain networks and intra-grain strain variations—aspects often overlooked by mean-field models.

Substantial datasets on magnesium deformation have been generated using both scanning electron microscopy (SEM-DIC) [55–57] and optical microscopy (OM-DIC) [9, 58–60]. To overcome the typical microscopy compromise between magnification and field-coverage, area-scanning can be implemented in both SEM-DIC and OM-DIC, yielding strain maps that bridge length-scales.

Among SEM-DIC studies, Orozco-Caballero et al.'s recent work [57] is noteworthy. They examined rolled Mg-AZ31 after 3% strain in RD-tension—a load condition opposite to that typically used to induce profuse twinning. Their study produced an extremely detailed map of deformation in a 30-grain neighborhood, resolving individual slip bands. A more recent effort [61] presents a similar measurement on the rare-earth alloy WE43. Chen and Daly [55] utilized a lower-resolution, high-coverage (103 grains) SEM-DIC approach on a large-grain (116 μm) WE43 rare-earth alloy sample, focusing on twin identification.

For OM-DIC, systematic efforts have detailed the strain accommodation of Magnesium AZ31 under various load paths, including profuse twinning [9], slip-dominated deformation [60], and cyclic loading [59]. Through comprehensive area-scanning, these studies sampled an enormous number of grains (up to $\sim 10^5$) with subgranular resolution, effectively bridging the crystallite and macroscopic scales. Crucially, these studies performed in situ measurements, presenting the evolution of strain patterns at closely spaced load points—a feature largely absent in SEM-DIC efforts. These studies elucidated the substructure of twin-driven macroscopic shear bands with high detail and statistical significance. They revealed that each macroscopic shear band comprises an intergranular-band network carrying a characteristic amount of strain [59]. Furthermore, in the cyclic loading study, the nature of reverse transformation (detwinning) was uniquely identified, alongside a second wave of twin bands emerging within plastically

hardened regions.

2.2. Modeling Efforts for Magnesium Alloys

Recently, the mechanical behavior magnesium alloys has been the subject of intense multiscale research activity that span all length-scales from atomistic to the component scale. Each modeling tool has their practical length-scale band, e.g., density functional theory span from a single atom scale to a small crystal domain, typically used for modeling the behavior of individual crystal defects [62–64]. Atomistic modeling tools are rather associated with material development (e.g., by studying the interaction of solute elements with a dislocation core [65]). For building the response of a polycrystalline aggregate made of a fixed material, however, the practical fundamental models are the crystal plasticity (CP) models. In other words, it is impossible to bring the atomistic models to the component scale both with regard to the lack of information (e.g., where each defect located) and the computational cost. CP models express plastic strain rate tensor (or plastic rate of deformation tensor depending on the model) as a linear combination of the activity of micro-mechanisms. The compound micro-mechanism set (basal, prismatic and pyramidal slip supplemented with the tensile twin) that is most commonly observed to operate in magnesium alloys is sketched in Figure 1, which also introduces the HCP unit cell and its c-axis. $\langle a \rangle$-axes with $\langle 11\bar{2}0 \rangle$ Miller indices are the closest lattice translation directions in the basal plane.

CP models will directly account for the effect of crystallographic texture since their primary input is a list of the grain orientations and their volume fractions [22]. These are essentially continuum models that construct the rate of deformation tensor in each crystallite as a summation of the shear activity in discrete slip systems [7]. The profound complication for magnesium alloys is once more related to how the mechanical twin is introduced into this class of models. The twin physically comes with an abrupt transformation strain and fundamentally alters the crystallographic orientation of its locality [47]. The latter factor means that, further slip inside the twin lamella occurs in different orientations compared to the parent grain [5]. The latter factor is ignored

by cruder models and many models are not detwinning capable (i.e., reversal of the twin domain on opposite load). Thus, the detail that is adopted when it comes to the twin transformation is the defining aspect of a magnesium alloy CP model. Detailed constitutive models with twinning-detwinning implementations are still discussed even when they are incorporated into the crude mean-field interaction [17].

2.2.1. Variational Crystal Plasticity Models

The theory of generalized standard materials (GSM), introduced by Halphen and Nguyen [66], offers a thermodynamically consistent framework for elastoplastic models. Central to this theory is the normal dissipativity hypothesis, which posits that the evolution laws for internal variables (such as plastic strain) are derived from a convex dissipation potential. This approach generalizes the classical associative flow rule and guarantees satisfaction of the second law of thermodynamics.

Building upon this thermodynamic foundation, Ortiz and Stainier developed a general variational formulation for viscoplastic constitutive updates [36]. Rather than explicitly integrating the rate equations for internal variables over a time step, this approach determines the updated material state by minimizing an incremental energy functional that combines the change in the Helmholtz free energy and the total dissipation within the time step.

The variational formulation is inherently consistent with thermodynamic principles, and the implicit updates derived from the minimization principle provide the method with significant numerical robustness, often allowing for larger time steps compared to explicit integration schemes. Furthermore, the incremental stress–strain relations derive from a pseudo-elastic strain energy density, which ensures the symmetry of the consistent tangent moduli—a highly desirable feature for finite element implementations. This unified framework accommodates diverse material behaviors, including finite strains and rate-sensitivity, and was later extended to coupled thermo-mechanical problems where both momentum and energy conservation laws are derived from a single joint

potential [37, 67].

For magnesium and its alloys, the variational framework proves particularly advantageous from a computational standpoint. By treating twin volume fractions as internal variables governed by energy minimization, these models determine the evolution of both plastic slip and twin volume fractions simultaneously through minimization of an incremental energy functional [2, 16, 30, 31, 33]. This approach naturally captures the competition between these two primary deformation mechanisms in magnesium. Through combination of a phase-field model for twinning with a crystal plasticity model for slip, this concept is further advanced, allowing for a more detailed description of the twin morphology and its evolution [68], which is often simplified in "pseudo-slip" approaches where twinning is treated as just another shear system.

2.2.2. Model Validation for Magnesium Alloys

Model validation for magnesium alloys has traditionally relied on several distinct experimental data sources, each providing unique insights into material behavior. Conventional stress–strain measurements from macroscopic mechanical tests are routinely used to calibrate and validate constitutive models, providing benchmarks for overall material response under diverse loading conditions including tension, compression, and cyclic loading [1, 14, 17].

Complementing stress–strain data, neutron diffraction techniques are extensively employed to obtain orientation-averaged measurements of elastic lattice strain as a function of applied stress, offering direct characterization of internal stress distributions and texture evolution in bulk polycrystalline samples [5, 21–28].

At the crystal level, single crystal plane-strain compression experiments pioneered by Kelley and Hosford [29] remain fundamental for parameter calibration (particularly for pure magnesium) [2, 16, 30–35], as they enable the isolated activation and quantification of individual slip and twin mechanisms within well-defined crystallographic orientations.

To capture the environmental sensitivity of deformation mechanisms, crystal plasticity models also utilize stress–strain measurements conducted across broad ranges of both temperature and strain rate. These experiments provide essential data for characterizing the temperature dependence [35, 69–72] and rate sensitivity [73] of slip and twinning processes in magnesium alloys.

Despite the proven utility of these established datasets, validation efforts that incorporate spatially-resolved strain fields—obtained through techniques such as digital image correlation (DIC) or electron microscopy—remain relatively limited [61]. Most current models are assessed against averaged or aggregate data, which can mask critical aspects of local deformation heterogeneity, strain localization patterns, and grain-to-grain mechanical interactions. Consequently, the capacity of existing models to accurately represent the complete deformation behavior of magnesium alloys, particularly the microstructural-level phenomena that govern macroscopic response, represents a significant ongoing challenge.

2.2.3. Length Scale in Crystal Plasticity Models

2.2.3.1. Mean-Field Models. Mean-field theories, including Taylor-type [41] and self-consistent models such as Elasto-Visco-Plastic Self-Consistent (EVPSC) models [17, 74], offer computational efficiency for simulating average response and texture evolution in large grain aggregates. The Taylor model assumes that each grain undergoes the same total (macroscopically applied) deformation, providing an upper bound on the stress–strain relation and serving as a traditional tool for texture calculations. In contrast, self-consistent models treat each grain as an ellipsoidal inclusion embedded within a homogeneous medium that represents the averaged behavior of surrounding grains.

Typical mean-field models employ Eshelby's inclusion theorem [75], treating each grain as an ellipsoidal inclusion that interacts with a homogenized medium whose tangent stiffness averages across all grains in the polycrystal. However, these models

typically homogenize grain neighborhoods without explicitly modeling grain boundaries or resolving local mechanical fields. The assumption of constant intra-grain fields inherent to this framework prevents crystallite-scale fidelity and contradicts recent experimental observations.

Within mean-field frameworks, twinning approaches include the "composite grain" (CG) model [76] and the "predominant twin reorientation" (PTR) model [77,78], both of which track new orientations resulting from twinning. These models provide exceptional computational efficiency—approximately three to four orders of magnitude faster than full-field models—making them ideal for analyzing relationships between large-scale grain aggregate microstructure and macroscopic properties.

Despite their efficiency, mean-field models have notable limitations. They may underestimate twin volume fractions at large strains in random textures [28], can exhibit abrupt increases in lattice strain when twinning is favored [79], and generally fail to capture local deformation concentration or stress reversal phenomena near twin bands [80].

2.2.3.2. Full-Field Models. Achieving crystallite-scale fidelity for any material requires geometric models that encompass sufficiently large grain neighborhoods, with each grain domain sampled using numerous elements or voxels to represent intra-grain strain localizations. This approach forms the basis of full-field models, which exist in both finite-element method variants [15] and spectral-solver variants [81, 82].

Full-field theories, including Crystal Plasticity Finite Element (CPFE) models [83, 84] and Green's function Fast Fourier Transform (FFT) crystal plasticity models [15, 16], explicitly account for grain-to-grain interactions and resolve spatially varying mechanical fields within deformed microstructures. These models capture detailed microstructural evolution, including the complex geometries of twinned regions such as lenticular and partially propagated twin bands.

However, the primary challenge for magnesium alloys remains the accurate representation of twin transformation mechanisms within these sophisticated modeling frameworks. The level of detail required to faithfully introduce twinning behavior continues to present significant computational and theoretical obstacles.

2.2.4. Implementation of Deformation Twinning

Early crystal plasticity finite element (CPFE) models treated twinning phenomenologically by incorporating it as an additional slip system, often referred to as a "pseudo-slip" mechanism. This approach, first developed by Kalidindi [85], introduces twinning-induced plasticity through the product of twin volume fraction and the fixed transformation strain. Accordingly, slip-induced plasticity is simultaneously handled as a mixture of slip in the parent grain and slip in the twin 'lamellae'.

This pseudo-slip formalism allows for the incorporation of twinning into the constitutive framework without explicitly modeling the twin nucleation and propagation processes. The twin volume fraction evolves according to hardening rules (similar to slip), which govern the growth of the twin volume as a function of current material state. This approach has been widely adopted in subsequent models, where each model defines unique hardening relations [2, 15, 33, 86].

Pseudo-slip models often aim to capture physically motivated heterogeneous deformation by explicitly representing the nucleation, propagation, and growth of twins in polycrystals. One common strategy involves reorienting materials or finite elements when the twinned volume fraction exceeds a specified threshold. This reorientation can be achieved by directly inserting twin lamellae within grains [87] or through a multi-step process: first determining nucleation points, selecting predominant twins, and then allowing twin expansion as applied stress increases [11, 27, 76, 88]. An alternative approach defines grain boundary energy as a function of twin volume fraction field gradients, as implemented in phase-field models. Through energy minimization, this method naturally produces lamellar twin morphologies [68]. Additionally, explicit

twin formation models have been developed, sometimes incorporating adaptive mesh generation methods to enhance computational accuracy [89].

However, pseudo-slip homogenization is an oversimplification of the actual physics, where twin-transformation lamellae form and grow inside the grains. Consequently, such models are generally not capable of predicting localization triggered by heterogeneous micro-twins. For any material point, the volume fraction is actually either 1 (if the point belongs to the twin transformation lamella of certain twin system) or 0 (if the point belongs to the parent, i.e., the untransformed region of the grain). Discrete-twin implementations that try to replicate the morphology and kinetics of the twin operation are actually very recent developments [13, 90]. Discrete-twin models aim to explicitly model the kinematics and kinetics of twin nucleation, propagation, and growth (thickening).

2.3. In-situ Temperature Measurements of Deforming Structures

The study of energy partitioning during plastic deformation stems from the pioneering calorimetric work of Taylor and Quinney. Their foundational experiments established the framework for modern thermomechanical analysis by quantifying how mechanical energy is either stored within the material or dissipated as heat during deformation [91]. This work introduced a relationship between plastic dissipation and applied plastic work through a proportionality constant, β, known as the Taylor–Quinney coefficient, which describes the fraction of plastic work converted to heat. Historically, β was commonly assumed to be a constant value of 0.9 across different materials and conditions. However, recent research challenges this assumption, demonstrating that the coefficient varies significantly with material type, loading conditions, and deformation mechanisms. This variability reveals a complex interplay between mechanical work input, thermal energy generation, and internal energy storage processes [92].

From a thermodynamic perspective, the deformation of solid materials always leads to temperature changes, driven by various thermal sources. These sources include

intrinsic dissipation (e.g., from plasticity, viscosity, or damage) and thermomechanical coupling mechanisms (e.g., thermoelasticity, latent heat of phase transformations) [93]. The local heat diffusion equation, derived from thermodynamic principles, directly links these heat generation mechanisms to temperature evolution. Extracting quantitative heat source distributions from measured surface temperature fields, however, poses a numerically challenging inverse problem due to the smoothing effects of heat diffusion and the presence of noise in thermal data [94]. To address this, simplified models, such as two-dimensional (2D) or zero-dimensional (0D) diffusion models, are often employed for thin specimens. These models are coupled with sophisticated image processing techniques for accurate derivative estimation [94,95]. The reliability of such calorimetric analyses hinges on the precision of temperature measurements, accurate determination of thermophysical parameters (density, specific heat, thermal conductivity), and the robustness of the image processing methodologies [93].

In the study of thermomechanical couplings, the advent of infrared (IR) detectors and cameras revolutionized the field, shifting from macroscopic, global calorimetric measurements [96] to non-contact, full-field thermal analyses of deforming surfaces [93, 97]. Modern IR cameras offer high spatial and temporal resolution, capable of detecting subtle temperature variations from hundredths to hundreds of degrees Celsius—a crucial capability for capturing the transient nature of deformation processes. IRT can be further combined with DIC to simultaneously measure thermal and strain fields in the same area of interest, enabling localized analysis of thermomechanical couplings. This combined approach has been successfully applied to various materials during cyclic loading, including polymers [95] and polycrystalline metals [98, 99]. The calorimetric information derived from these thermal measurements provides invaluable insight into the irreversibility of deformation mechanisms and the thermal sensitivity of materials. Furthermore, it offers crucial validation for thermomechanical models, as coupling sources and dissipation are intrinsically linked to a material's constitutive equations.

2.3.1. Thermal Measurement of Magnesium

Current fundamental-scale models for magnesium alloys, which aim to capture the intricate interplay of twinning, detwinning, and slip micro-mechanisms through mechanical field measurements, often overlook the energetic (calorimetric) consequences of deformation derived from in situ thermal measurements. This omission is significant because the processes of energy storage and dissipation during deformation provide a distinct signature that can unveil the physics, chronology, and causality of the underlying microscopic activity.

Temperature measurements as a byproduct of deformation in magnesium alloys primarily fall into two categories, though a deeper mechanistic understanding is increasingly emphasized. The first category comprises high-cycle fatigue studies that investigate cyclic hardening/softening via the temperature signal. These include research on tensile loading [100, 101], the performance of welded joints [102], and three-point bending [103]. The tensile loading and welded joint studies involve stress cycling that opposes significant twin activity, where twinning plays a secondary role. While the bending study inherently induces twinning on one side of the beam, the analysis predominantly focuses on the opposite edge where failure occurred. Nevertheless, these fatigue studies typically do not aim for a deep mechanistic understanding of the material at the microstructural level; instead, they focus on the evolution of microstructure and its thermal signature over cycles.

Regarding studies that specifically investigate the dissipative behavior of individual deformation mechanisms through mechanical testing, the literature for magnesium alloys remains very limited. To our knowledge, it currently consists of only two recent high strain-rate studies [104, 105] conducted with Hopkinson bars (nominal strain rates around 10^3 s^{-1}). Interestingly, these studies do not cite any prior thermal measurements on magnesium alloys. The closest reference to our intended spatially resolved infrared thermography approach in a system exhibiting twin propagation bands is an iron-based Fe–3wt.% Si material [106].

For magnesium, Kingstedt and Lloyd [105] is in particular relevant from a mechanistic understanding perspective, since they consider multiple shear compression samples cut from a rolled plate but in different directions to incite twinning- and slip-dominated deformation. The Taylor–Quinney coefficient for the twinning sample is pretty meager (0.4) and less than that of the slip-dominated orientations (0.6).

Despite this, research on magnesium that incorporates in situ thermal measurements and calorimetric analysis remains limited in scope. The existing literature primarily consists of fatigue studies that do not delve into constitutive behavior, alongside a few high-strain-rate investigations attempting to separate the stored and dissipated components of plastic work. In Kolsky bar experiments, the thermoelastic effect—an isentropic form of thermomechanical coupling—is typically overshadowed by dissipative phenomena and consequently neglected. Furthermore, the inherent constraints of Kolsky bar testing restrict investigations to monotonic loading conditions, despite the fact that many significant deformation phenomena in magnesium, especially those involving twinning mechanisms, manifest under non-monotonic loading histories.

3. METHODOLOGY

3.1. Theoretical Framework

This section outlines the theoretical framework used for the crystal plasticity model of magnesium alloys, focusing on the kinematic description, thermodynamic principles, and variational formulation. The model incorporates both slip and twinning mechanisms, addressing the unique challenges posed by the complex mechanical behavior of magnesium alloys.

3.1.1. Kinematic Description

Plastic deformation in crystalline magnesium is characterized by two distinct families of deformation mechanisms operating simultaneously. The first involves slip systems, which is the primary mode of plastic deformation in most crystalline materials, each defined by a direction vector $\boldsymbol{s}^{(\alpha)}$ and its corresponding slip plane normal $\boldsymbol{m}^{(\alpha)}$ (both unit vectors). The second family encompasses twinning systems, where each system is characterized by a twinning plane normal $\boldsymbol{n}^{(\beta)}$ and the associated shear direction $\boldsymbol{a}^{(\beta)}$ along which twinning occurs. The superscript convention distinguishes slip systems (α) from twin systems (β), following established crystallographic nomenclature [85].

The mathematical representation of plastic deformation thus incorporates two primary kinematic variables. Dislocation-mediated plasticity is quantified through slip shear $\boldsymbol{\gamma} = \{\gamma^{(\alpha)}\}$, representing the set of shear strains on each slip system α. In this work, only basal, prismatic, and $\langle c + a \rangle$ pyramidal slip systems are considered (Figure 1.1b, c). Concurrently, twin-induced deformation is characterized by twin volume fractions $\boldsymbol{\lambda} = \{\lambda^{(\beta)}\}$, which specify the portion of material that has undergone twinning in each system (β). These twin volume fractions must satisfy fundamental physical constraints to ensure that they remain within physically meaningful bounds.

Specifically, the following constrains are imposed:

$$0 \leq \lambda^{(\beta)} \leq 1 \quad \text{for} \quad (\beta) = 1, \ldots, n_{\text{tw}} \tag{3.1a}$$

$$0 \leq \sum_{\beta=1}^{n_{\text{tw}}} \lambda^{(\beta)} \leq 1. \tag{3.1b}$$

These constrains ensure that twin volume fractions remain individually and collectively bounded between being fully twinned or not twinned at all. For this work, only tensile twinning systems are considered (Figure 1.1d), as they are the predominant twinning mode in magnesium under the loading conditions of interest.

A critical limitation of this kinematic approach lies in its inability to resolve the microscopic complexities of individual twin structures, which typically manifest at length scales significantly smaller than those relevant for mesoscopic dislocation behavior in polycrystalline aggregates. This contrasts markedly with alternative modeling strategies such as discrete twin approaches [13,107] or explicit continuum formulations that directly track individual twin boundaries [31, 87]. By employing volume fraction averaging, this formalism deliberately separates length scales, enabling efficient characterization of bulk material behavior at the mesoscopic level while sacrificing twin morphology information.

Twinning deformation leads to a specific geometric reorientation of the crystallographic lattice. This reorientation mirrors the lattice across twin planes, which are characterized by the normal vector $\boldsymbol{n}^{(\beta)}$, and mathematically described by the following reflection operation

$$\boldsymbol{Q}^{(\beta)} = \boldsymbol{I} - 2\boldsymbol{n}^{(\beta)} \otimes \boldsymbol{n}^{(\beta)}. \tag{3.2}$$

This mirroring systematically transforms all existing slip systems from their original configuration in the parent grain into corresponding orientations within the newly formed twin domains

$$\boldsymbol{s}'^{(\alpha,\beta)} = \boldsymbol{Q}^{(\beta)}\boldsymbol{s}^{(\alpha)} \tag{3.3a}$$

$$\boldsymbol{m}'^{(\alpha,\beta)} = \boldsymbol{Q}^{(\beta)}\boldsymbol{m}^{(\alpha)}. \tag{3.3b}$$

Here, $(\boldsymbol{s}^{(\alpha)}, \boldsymbol{m}^{(\alpha)})$ denotes the original slip system, while $(\boldsymbol{s}'^{(\alpha,\beta)}, \boldsymbol{m}'^{(\alpha,\beta)})$ represents its transformed counterpart in the twinned orientation (β).

For this thesis, a small-strain formulation is employed. This approach is justified because the maximum applied strains in the experiments are within the ±2% range (see Section 3.3). Consequently, the for material's kinematic description, an additive decomposition of the total strain tensor, $\boldsymbol{\varepsilon}$, and its rate, $\dot{\boldsymbol{\varepsilon}}$, into elastic and plastic components is assumed

$$\boldsymbol{\varepsilon} = \boldsymbol{\varepsilon}_{\mathrm{el}} + \boldsymbol{\varepsilon}_{\mathrm{pl}} \tag{3.4a}$$

$$\dot{\boldsymbol{\varepsilon}} = \dot{\boldsymbol{\varepsilon}}_{\mathrm{el}} + \dot{\boldsymbol{\varepsilon}}_{\mathrm{pl}}. \tag{3.4b}$$

Here, the elastic component ($\boldsymbol{\varepsilon}_{\mathrm{el}}$) represents the reversible deformation, whereas the plastic component ($\boldsymbol{\varepsilon}_{\mathrm{pl}}$) is further decomposed into slip and twinning components to account for the irreversible deformations

$$\dot{\boldsymbol{\varepsilon}}_{\mathrm{pl}} = \dot{\boldsymbol{\varepsilon}}_{\mathrm{sl}} + \dot{\boldsymbol{\varepsilon}}_{\mathrm{tw}}. \tag{3.5}$$

Adhering to the 'pseudo-slip' formalism of Kalidindi [85], following flow rules are used to describe each component of plastic flow

$$\dot{\boldsymbol{\varepsilon}}_{\mathrm{sl}} = \left(1 - \sum_{\beta=1}^{n_{\mathrm{tw}}} \lambda^{(\beta)}\right) \sum_{\alpha=1}^{n_{\mathrm{sl}}} \dot{\gamma}^{(\alpha)} \boldsymbol{M}^{(\alpha)} + \sum_{\beta=1}^{n_{\mathrm{tw}}} \lambda^{(\beta)} \left(\sum_{\alpha=1}^{n_{\mathrm{sl}}} \dot{\gamma}^{(\alpha)} \boldsymbol{M}'^{(\alpha,\beta)}\right) \tag{3.6a}$$

$$\dot{\boldsymbol{\varepsilon}}_{\mathrm{tw}} = \sum_{\beta=1}^{n_{\mathrm{tw}}} \gamma_{\mathrm{tw}} \dot{\lambda}^{(\beta)} \boldsymbol{M}^{(\beta)}, \tag{3.6b}$$

where the first term on the right-hand side of Equation 3.6a represents slip in parent grain, while the second term accounts slip in all twinned regions; and

$$\boldsymbol{M}^{(\alpha)} = \left(\boldsymbol{s}^{(\alpha)} \otimes \boldsymbol{m}^{(\alpha)}\right)_{\mathrm{sym}} \tag{3.7a}$$

$$\boldsymbol{M}^{(\beta)} = \left(\boldsymbol{a}^{(\beta)} \otimes \boldsymbol{n}^{(\beta)}\right)_{\mathrm{sym}}, \tag{3.7b}$$

are the symmetric parts of Schmid tensors for slip and twinning, respectively. It is implied that $\boldsymbol{M}'^{(\alpha,\beta)}$ is the reoriented Schmid tensor for slip system (α) in twinned orientation (β), which can be computed using Equation 3.3.

Because twin deformation reorients slip systems (Equation 3.3), the slip component of plastic flow must be expanded beyond standard crystal plasticity models. This expanded model accounts for dislocation motion on both the original slip systems and their twin-reoriented equivalents.

Equation 3.6a effectively homogenizes the slip deformation occurring in both the initial (parent) and twinned orientations. Conversely, Equation 3.6b models twin-mediated shear using a pseudo-slip formalism. In this approach, the rate of twinning shear is defined as the product of the rate of change of twin volume fraction, $\dot{\lambda}^{(\beta)}$, and γ_{tw}, the characteristic shear of the twin system [108]. γ_{tw} is a geometric property of the HCP crystal structure. For $[10\bar{1}2]$ twinning, it is defined as

$$\gamma_{\text{tw}} = \frac{\sqrt{3}}{\chi} - \frac{\chi}{\sqrt{3}}, \tag{3.8}$$

where χ is the c/a ratio of the hexagonal unit cell. For magnesium and its light alloys, $\chi \approx 1.624$ [4], which yields $\gamma_{\text{tw}} \approx 0.129$ for $[10\bar{1}2]$ twinning.

3.1.2. Constitutive Model

The crystal plasticity model in this thesis adapts the variational viscoplastic model developed by Chang and Kochmann [33]. The variational method assumes the existence of a Helmholtz free-energy density potential, ψ, representing the stored energy withing the system, and the dual form of the dissipation (pseudo-)potential, ϕ^*, which characterizes the energy dissipation mechanisms. (Both defined per unit undeformed volume.) Combined, these potentials govern the evolution of internal variables, i.e. as plastic slips and twin volume fractions. This evolution follows the principle of maximum dissipation, achieved by minimizing the stress power

$$0 \in \frac{\partial}{\partial \dot{\gamma}^{(\alpha)}} \left(\dot{\psi} + \phi^* \right) \tag{3.9a}$$

$$0 \in \frac{\partial}{\partial \dot{\lambda}^{(\beta)}} \left(\dot{\psi} + \phi^* \right). \tag{3.9b}$$

ψ is assumed to be additively composed of elastic, plastic, and thermal parts. The plastic part is, in turn, decomposed into components for slip and twinning:

$$\psi(\boldsymbol{\varepsilon}, \boldsymbol{\gamma}, \boldsymbol{\lambda}, T) = \psi_{\text{el}}(\boldsymbol{\varepsilon}_{\text{el}}, T) + \psi_{\text{pl}}(\boldsymbol{\gamma}, \boldsymbol{\lambda}) + \psi_{\text{th}}(T) \tag{3.10a}$$

$$\psi(\boldsymbol{\varepsilon}, \boldsymbol{\gamma}, \boldsymbol{\lambda}, T) = \psi_{\text{el}}(\boldsymbol{\varepsilon}_{\text{el}}, T) + \psi_{\text{sl}}(\boldsymbol{\gamma}) + \psi_{\text{tw}}(\boldsymbol{\lambda}) + \psi_{\text{th}}(T). \tag{3.10b}$$

Here, it is implied that ψ_{pl} depends on $\boldsymbol{\varepsilon}_{\text{pl}}$ only through $\boldsymbol{\gamma}$ and $\boldsymbol{\lambda}$.

The equilibrium equations then take the following forms

$$\rho\eta = -\frac{\partial\psi}{\partial T} = -\frac{\partial\psi_{\text{el}}}{\partial T} - \frac{\partial\psi_{\text{th}}}{\partial T} \tag{3.11a}$$

$$\boldsymbol{\sigma} = \frac{\partial\psi}{\partial\boldsymbol{\varepsilon}} = \frac{\partial\psi_{\text{el}}}{\partial\boldsymbol{\varepsilon}_{\text{el}}}, \tag{3.11b}$$

where η is the entropy density, $\boldsymbol{\sigma}$ is the Cauchy stress tensor, and $\boldsymbol{Y}$ are the thermodynamic forces conjugate to the plastic slip and twin volume fractions.

The thermal energy density ψ_{th} accounts for thermally stored energy, and is defined as

$$\psi_{\text{th}}(T) = \frac{1}{2}\rho C\frac{(T-T_0)^2}{T_0}, \tag{3.12}$$

where C is the heat capacity, and T_0 is the reference temperature. This formulation assumes a linear temperature dependence, which is a reasonable approximation for the temperature ranges considered in this thesis.

The elastic free-energy density ψ_{el} is modeled using a linear thermoelastic formulation, consistent with the assumptions made during experimental data processing (and discussed further in Section 3.3.4.) The specific form is

$$\psi_{\text{el}}(\boldsymbol{\varepsilon}_{\text{el}}, T) = \frac{1}{2}\boldsymbol{\varepsilon}_{\text{el}} : \mathbb{C} : \boldsymbol{\varepsilon}_{\text{el}} - 3\kappa\alpha_{\text{th}}(T-T_0)\,\text{tr}(\boldsymbol{\varepsilon}_{\text{el}}), \tag{3.13}$$

where T is the temperature, T_0 is the initial temperature, α_{th} is the thermal expansion coefficient, and κ is the bulk modulus. $\mathbb{C}$ is the fourth-order elastic stiffness tensor, which, although magnesium is transversely isotropic, can be closely approximated as isotropic for the purposes of this model. In that case, ψ_{el} can simply be expressed as

$$\psi_{\text{el}}(\boldsymbol{\varepsilon}_{\text{el}}, T) = \frac{1}{2}\lambda\,\text{tr}(\boldsymbol{\varepsilon}_{\text{el}})^2 + \mu\;\boldsymbol{\varepsilon}_{\text{el}} : \boldsymbol{\varepsilon}_{\text{el}} - (3\lambda+2\mu)\alpha_{\text{th}}(T-T_0)\,\text{tr}(\boldsymbol{\varepsilon}_{\text{el}}), \tag{3.14}$$

where λ and μ are the Lamé parameters. The same practice can be found in the literature, e.g. [16, 34, 109].

The free energy related to plastic slip ψ_{sl} is defined as a function of cumulated slip shear on each system

$$\epsilon^{(\alpha)} = \int_{t_0}^{t} \dot{\gamma}^{(\alpha)} dt. \tag{3.15}$$

The functional form of ψ_{sl} combines an exponential self-hardening law, which mimics Voce hardening, and a linear hardening part that accounts for latent hardening

$$\psi_{\text{sl}}(\boldsymbol{\epsilon}) = \sum_{\alpha=1}^{n_{\text{sl}}} \left\{ \sigma_0^{(\alpha)} \epsilon^{(\alpha)} + \sigma_\infty^{(\alpha)} \left[\epsilon^{(\alpha)} + \frac{\sigma_\infty^{(\alpha)}}{h^{(\alpha)}} \exp\left(-\frac{h^{(\alpha)} \epsilon^{(\alpha)}}{\sigma_\infty^{(\alpha)}} \right) \right] \right\} + \frac{1}{2} \boldsymbol{\epsilon} \cdot \mathcal{H} \boldsymbol{\epsilon}, \tag{3.16}$$

where $\sigma_0^{(\alpha)}$ is the initial yield stress, $\sigma_\infty^{(\alpha)}$ is the saturation yield stress on each slip system (α), $h^{(\alpha)}$ is the hardening modulus, and $\mathcal{H}$ is a symmetric matrix containing the latent hardening moduli on its off-diagonals.

Similarly, the twinning part of the free-energy density W_{tw} incorporates both self-hardening and latent hardening contributions, but with a simpler functional form

$$\psi_{\text{tw}}(\boldsymbol{\lambda}) = \sum_{\beta=1}^{n_{\text{tw}}} \left\{ \sigma_0^{(\beta)} \lambda^{(\beta)} + \frac{1}{2} k^{(\beta)} (\lambda^{(\beta)})^2 \right\} + \frac{1}{2} \boldsymbol{\lambda} \cdot \mathcal{K} \boldsymbol{\lambda}, \tag{3.17}$$

where $k^{(\beta)}$ is the self-hardening parameter of twin system β, and $\mathcal{K}$ is a symmetric matrix containing the latent hardening moduli on its off-diagonals.

Unlike other variational thermomechanical models (e.g. [35, 37]), explicit temperature dependence is not included in the plastic energy density, a reasonable assumption given the self-heating range (on the order of mK) observed in this thesis (see experimental results under Chapter 4).

The dissipation potential ϕ^* is introduced to describe the dissipative characteristic of slip and twinning. It is additively decomposed into contributions from slip and twinning, with both components exhibiting the same functional form. Initially, a power-law form pure rate-dependent dissipation (viscous dissipation, VD) is used, as defined in [33]:

$$\phi_{\text{sl}}^*(\dot{\boldsymbol{\gamma}}) = \sum_{\alpha=1}^{n_{\text{sl}}} \frac{\tau_0^{(\alpha)} \dot{\gamma}_0^{(\alpha)}}{m+1} \left(\frac{\dot{\gamma}^{(\alpha)}}{\dot{\gamma}_0^{(\alpha)}} \right)^{m+1} \tag{3.18a}$$

$$\phi_{\text{tw}}^*(\dot{\boldsymbol{\lambda}}) = \sum_{\beta=1}^{n_{\text{tw}}} \frac{\tau_0^{(\beta)} \dot{\lambda}_0^{(\beta)}}{m+1} \left(\frac{\dot{\lambda}^{(\beta)}}{\dot{\lambda}_0^{(\beta)}} \right)^{m+1} . \tag{3.18b}$$

Here, τ_0 values represent reference stress values for slip and twinning systems, and m is the rate dependency exponent, which controls the rate sensitivity of the material response. The reference slip/twin rates, denoted as $\dot{\gamma}_0$ and $\dot{\lambda}_0$, are used to normalize

the rate-dependent terms.

However, this form of viscous dissipation on its own is found to be not sufficient to model the observed energetic characteristic in magnesium (see Section 4.3). Therefore, the dissipation potential is amended by an additional term that introduces rate-independent dissipation (plastic dissipation, PD)

$$\begin{aligned}\phi_{\mathrm{sl}}^{*}(\dot{\boldsymbol{\gamma}};\ \boldsymbol{\epsilon}) = &\underbrace{\sum_{\alpha=1}^{n_{\mathrm{sl}}} \frac{\tau_0^{(\alpha)}\dot{\gamma}_0^{(\alpha)}}{m+1}\left(\frac{\dot{\gamma}^{(\alpha)}}{\dot{\gamma}_0^{(\alpha)}}\right)^{m+1}}_{VD} \\ &+\underbrace{\sum_{\alpha=1}^{n_{\mathrm{sl}}} \dot{\gamma}^{(\alpha)}\sigma_{\infty}^{(\alpha)}\left[1-\exp\left(-\frac{h^{(\alpha)}\epsilon^{(\alpha)}}{\sigma_{\infty}^{(\alpha)}}\right)\right]}_{PD}.\end{aligned} \tag{3.19}$$

Mechanically, PD results in a Voce-like hardening behavior, akin to that of its plastic storage (PS) counterpart within the free-energy density of slip plasticity ψ_{sl}. Energetically, however, the portion of plastic work contributing to hardening through PD dissipates entirely.

A helpful analogy can be drawn to classical rheological models to understand these two dissipative components. The viscous dissipation (VD) term, with its power-law dependence on the rate of slip or twinning, functions like a dashpot element, where the dissipative force is sensitive to the rate of deformation. In contrast, the plastic dissipation (PD) term is rate-independent and acts like a friction element, providing a dissipative resistance once motion is initiated, regardless of its rate. However, unlike a simple friction element, the resistance from PD, as defined in Equation 3.19, evolves with deformation.

3.2. Numerical Implementation

The material's response depends on its initial state and past deformation history (initial conditions), and it is subjected to prescribed forces or displacements along its spatial boundaries (boundary conditions), with its behavior evolving continuously over time. The numerical solution of such initial boundary value problems (IBVPs) within a

variational framework for dissipative solids, particularly those exhibiting viscoplastic behavior, is typically achieved through an incremental procedure, by transforming the continuous evolution problem into a sequence of time-discrete, incremental boundary value problems, each formulated as a nested optimization problem.

This methodology, as outlined by [36] and later expanded to include coupled thermomechanical effects by [37], ensures that the incremental stress–strain relations derive from a pseudo-elastic strain-energy density, thereby conferring a variational structure to the incremental problem.

The core of this numerical procedure involves two nested numerical optimization steps, designed to update the material state from time t_n to t_{n+1}. At the beginning of each time increment, the external load conditions are applied and held fixed throughout the inner minimization problem.

3.2.1. Inner Problem: Variational Constitutive Updates

The first, inner minimization step determines the rates of internal variables through variational constitutive updates. These updates represent time-discretized versions of the continuous variational statements of constitutive relations. Their primary objective is to characterize updated internal variables and kinematic parameters as minimizers of a suitably chosen rate potential function (that concurrently maximizes dissipation), ensuring that incremental stress–deformation relations derive from a potential—crucial for maintaining the variational structure [36].

The evolution of internal variables is governed by a rate potential (Equation 3.9), such that

$$\dot{\boldsymbol{Z}} \leftarrow \arg\min_{\dot{\boldsymbol{Z}}} D(\dot{\boldsymbol{\varepsilon}}, \dot{\eta}, \dot{\boldsymbol{Z}}, T;\ \boldsymbol{\varepsilon}, \eta, \boldsymbol{Z}), \tag{3.20}$$

where $\dot{\boldsymbol{Z}} = \{\dot{\boldsymbol{\gamma}}^{(\alpha)}, \dot{\boldsymbol{\lambda}}^{(\beta)}\}$ represents the rates of internal variables. This rate potential is

fundamentally defined as:

$$D(\dot{\boldsymbol{\varepsilon}}, \dot{\eta}, \dot{\boldsymbol{Z}}, T;\ \boldsymbol{\varepsilon}, \eta, \boldsymbol{Z}) = \frac{d}{dt}U(\boldsymbol{\varepsilon}, \eta, \boldsymbol{Z}) - \rho_0 \dot{\eta} T + \phi^* \left(\frac{T}{\Theta}\dot{\boldsymbol{\varepsilon}}, \frac{T}{\Theta}\dot{\boldsymbol{Z}};\ \boldsymbol{\varepsilon}, \Theta(\boldsymbol{\varepsilon}, \eta, \boldsymbol{Z}), \boldsymbol{Z} \right). \tag{3.21}$$

Here, $U(\boldsymbol{\varepsilon}, \eta, \boldsymbol{Z})$ represents the internal energy density potential, from which the equilibrium (or internal) temperature Θ is derived as

$$\Theta(\boldsymbol{\varepsilon}, \eta, \boldsymbol{Z}) \equiv \frac{1}{\rho_0}\frac{\partial U}{\partial \eta}(\boldsymbol{\varepsilon}, \eta, \boldsymbol{Z}), \tag{3.22}$$

and ρ_0 is the reference density.

For an arbitrary time interval $[t_n, t_{n+1}]$, given the initial state $\{\boldsymbol{\varepsilon}_n, \eta_n, \boldsymbol{Z}_n\}$ and updated external variables $\{\boldsymbol{\varepsilon}_{n+1}, T_{n+1}\}$, the objective is to compute the updated internal variables $\boldsymbol{Z}_{n+1}$ and other kinematic variables defining the material's internal evolution. This is achieved by minimizing the incremental form of the energy density (Equation 3.9), denoted as $\mathcal{W}_n$, which acts as a potential for updated stresses and entropy [110]. While noting that $\dot{U} - \rho_0 \dot{\eta} T = \dot{\psi} - \rho_0 \eta \dot{T}$, the incremental energy density can be expressed as

$$\begin{aligned} &\mathcal{W}_n(\boldsymbol{\varepsilon}_{n+1}, T_{n+1};\ \boldsymbol{\varepsilon}_n, T_n, \boldsymbol{Z}_n) \equiv \\ &\inf_{\boldsymbol{Z}_{n+1}} \Bigg[\psi(\boldsymbol{\varepsilon}_{n+1}, T_{n+1}, \boldsymbol{Z}_{n+1}) - \psi(\boldsymbol{\varepsilon}_n, T_n, \boldsymbol{Z}_n) \\ &\quad + \rho_0 \eta_n (T_{n+1} - T_n) \\ &\quad + \Delta t \left\langle \phi^* \left(\frac{T_{n+1}}{T_n}\frac{\Delta \boldsymbol{\varepsilon}}{\Delta t}, \frac{T_{n+1}}{T_n}\frac{\Delta \boldsymbol{Z}}{\Delta t};\ \boldsymbol{\varepsilon}(t), T(t), \boldsymbol{Z}(t) \right) \right\rangle \Bigg], \end{aligned} \tag{3.23}$$

where the term with angled brackets $\langle \cdot \rangle$ denotes averaging of dissipation pseudo-potential over the time step. For this term, the following consistent approximation is used:

$$\begin{aligned} &\left\langle \phi^* \left(\frac{T_{n+1}}{T_n}\frac{\Delta \boldsymbol{\varepsilon}}{\Delta t}, \frac{T_{n+1}}{T_n}\frac{\Delta \boldsymbol{Z}}{\Delta t};\ \boldsymbol{\varepsilon}(t), T(t), \boldsymbol{Z}(t) \right) \right\rangle \\ &\approx \frac{T_{n+1}}{T_n}\phi^* \left(\frac{T_{n+1}}{T_n}\frac{\Delta \boldsymbol{\varepsilon}}{\Delta t}, \frac{T_{n+1}}{T_n}\frac{\Delta \boldsymbol{Z}}{\Delta t};\ \boldsymbol{\varepsilon}_{n+\alpha}, T_n, \boldsymbol{Z}_{n+\alpha} \right) \\ &+ \frac{\Delta T}{T_{n+1}}\phi^* \left(\frac{T_{n+1}}{T_n}\frac{\Delta \boldsymbol{\varepsilon}}{\Delta t}, \frac{T_{n+1}}{T_n}\frac{\Delta \boldsymbol{Z}}{\Delta t};\ \boldsymbol{\varepsilon}_{n+\alpha}, T_{n+\alpha}, \boldsymbol{Z}_{n+\alpha} \right), \end{aligned} \tag{3.24}$$

where $\alpha \in [0, 1]$ is an algorithmic parameter that denotes a linearization between current

and next material states such that $\{\cdot\}_{n+\alpha} = (1-\alpha)\{\cdot\}_n + \alpha\{\cdot\}_{n+1}$.

This formulation guarantees that the incremental heat equation remains consistent with its continuous counterpart as $\Delta t \to 0$. Such consistency is essential when developing numerical updates for thermomechanical constitutive models that incorporate explicit temperature-dependent dissipation. Notably, the most straightforward approximation for average dissipation—a fully implicit approach, such as $\phi^*\left(\frac{T_{n+1}}{T_n}\frac{\Delta \boldsymbol{\varepsilon}}{\Delta t}, \frac{T_{n+1}}{T_n}\frac{\Delta \boldsymbol{Z}}{\Delta t};\ \boldsymbol{\varepsilon}_{n+1}, T_{n+1}, \boldsymbol{Z}_{n+1}\right)$—fails to produce fully consistent results as the time increment approaches zero [110].

3.2.1.1. Projected Gradient Method. The minimization problem in Equation 3.23 is solved using the projected gradient method, an iterative Newton-like minimization technique for optimization problems with simple constraints [111]. This method is particularly well-suited when internal variable rates $\dot{\boldsymbol{Z}}$ are subject to straightforward constraints, such as non-negativity (e.g., $\dot{\boldsymbol{\gamma}} \geq 0$ for slip systems in crystal plasticity, or twin volume fraction constraints as described in Equation 3.1.

The general form of this iterative algorithm is:

$$x_{k+1} = [x_k - \alpha_k B_k \nabla f(x_k)]^{\#}, \tag{3.25}$$

where x_k represents the current iterate for $\dot{\boldsymbol{Z}}$, $f(x_k)$ is the objective function (the incremental potential given in Equation 3.23), $\nabla f(x_k)$ is its gradient with respect to $\dot{\boldsymbol{Z}}$ (in practice, corresponding to the net difference between RSS and CRSS), α_k is a positive step size determined by an Armijo-like rule, and B_k is a positive-definite symmetric matrix (typically the inverse of the analytical Hessian $H_k = \nabla^2 f(x_k)$, or a close approximation to it). The projection operator $[\cdot]^{\#}$ maps the unconstrained gradient-descent step back onto the feasible set of internal variable rates.

Once this inner minimization converges, the updated internal variables are computed by integrating their rates over the time step. The minimum value of this inner minimization, $\mathcal{W}_n$—corresponds to the actual process that maximizes the rate of energy

dissipation—then forms an "effective rate potential" for the stresses and entropy [110].

Due to the large differences between hardening terms of different deformation mechanisms (e.g., between basal and pyramidal slip), the Hessian may contain numerical entries that differ by orders of magnitude. This disparity necessitates a robust factorization of the Hessian matrix using the modified Cholesky factorization method, as described in [112] and detailed in their earlier work [113].

This method ensures numerically stable factorization of the Hessian matrix, H_k, by producing a positive-definite matrix through the modification

$$\tilde{H}_k = H_k + E_k, \tag{3.26}$$

where E_k is a diagonal matrix that is zero if H_k is already sufficiently positive definite. Otherwise, the sum in Equation 3.26 produces a positive-definite matrix $\tilde{H}_k$ that differs from the original Hessian only in its diagonal elements. This modification is essential because the Hessian of the objective function in nonlinear optimization problems may not always be positive definite, which can lead to numerical instability. By ensuring positive definiteness, the modified Cholesky method guarantees that the search direction p_k derived from solving $\tilde{B}_k p_k = -\nabla f(x_k)$ is always a descent direction, even when the original Hessian is indefinite, thus maintaining the numerical stability and convergence properties essential for reliable minimization.

3.2.1.2. Twinning–Detwinning–Retwinning. In the pseudo-slip implementation used in this thesis, the detwinning and retwinning capability is realized by considering two distinct volume fractions (VFs) for each twin system: $\lambda_+^{(\alpha)}$ for twinning and $\lambda_-^{(\alpha)}$ for detwinning. This approach mirrors how slip systems are divided into positive and negative directions. However, instead of restricting the individual twin system volume fractions, the difference between the twinning and detwinning VFs are constrained to be between 0 and 1

$$0 \leq \lambda_+^{(\beta)} - \lambda_-^{(\beta)} \leq 1 \ . \tag{3.27}$$

It is important to note that the increments of both twinning and detwinning VFs ($\Delta\lambda$) are nonnegative

$$0 \leq \Delta\lambda_{+}^{(\beta)} \tag{3.28a}$$

$$0 \leq \Delta\lambda_{-}^{(\beta)} \ , \tag{3.28b}$$

as opposite directions are handled separately in terms of magnitude. This ensures that the VFs themselves remain nonnegative

$$0 \leq (\lambda_{+,\,n}^{(\beta)} + \Delta\lambda_{+}^{(\beta)}) - (\lambda_{-,\,n}^{(\beta)} + \Delta\lambda_{-}^{(\beta)}) \leq 1 \ . \tag{3.29}$$

Therefore, the only additional constraints needed (beyond the lower bound of zero) at the start of constitutive updates are the upper bounds for the twin VF increments. Furthermore, since the total twin volume fraction is always greater than or equal to the VF of a single twin system, the upper bounds of each twin VF increment depend solely on the total twin VF at the start of the time step n. If Equation 3.29 is rearranged and the VF increments are assumed to be small relative to the volume fractions themselves, upper bounds for VF increments can be written as

$$\Delta\lambda_{+}^{(\beta)} \leq 1 - \sum_{\beta=1}^{n_{\text{tw}}} \lambda_{+,\,n}^{(\beta)} - \lambda_{-,\,n}^{(\beta)} \tag{3.30a}$$

$$\Delta\lambda_{-}^{(\beta)} \leq \sum_{\beta=1}^{n_{\text{tw}}} \lambda_{+,\,n}^{(\beta)} - \lambda_{-,\,n}^{(\beta)} \ . \tag{3.30b}$$

To enhance the numerical stability of twin activation, a subroutine at the beginning of each time step identifies the most active twin system; or if no twin system is active, it marks the twin variant with the largest RSS–CRSS difference. Rather than relying on numerical suppression to allow only one twin variant at a material point (as done by, e.g., [33]), this method deactivates all other twin systems once the most active variant is determined. These systems remain inactive until the total twin volume fraction returns to zero, signifying full detwinning. This approach effectively restricts activity to a single twin system at a material point without introducing artificial hardening rules. With this improvement, twin systems can, in theory, twin, detwin, and retwin repeatedly within the viscoplastic material model.

3.2.2. Outer Problem: Equilibration of the System

3.2.2.1. Root-finding Problem. The second, outer step utilizes the effective rate potential to determine the actual strain state at the current time step. This step involves finding a root of the residual (free stress components, $\boldsymbol{\sigma}_{\text{free}}$, plus effective entropy increase, $\rho\Delta\eta_{\text{eff}}$) derived from the effective potential $\mathcal{W}_n$ with respect to the external variables (strain and temperature)

$$\boldsymbol{r}(\boldsymbol{\varepsilon}, T) = \begin{bmatrix} \boldsymbol{\sigma}_{\text{free}} \\ \rho\Delta\eta_{\text{eff}} \end{bmatrix} = \begin{bmatrix} \boldsymbol{\sigma}_{\text{free}} \\ \rho\Delta\eta - \frac{\Delta\mathcal{D}_{\text{int}}}{T} \end{bmatrix} = \begin{bmatrix} \frac{\partial\mathcal{W}_n}{\partial\boldsymbol{\varepsilon}} \\ -\frac{\partial\mathcal{W}_n}{\partial T} \end{bmatrix}, \tag{3.31}$$

$\mathcal{D}_{\text{int}}$ is the intrinsic dissipation (see Appendix A). Thus, the (adiabatic) root-finding problem aims to find the strain increment $\Delta\boldsymbol{\varepsilon}$ and the temperature increment ΔT such that the residual $\boldsymbol{r}$ components are driven to zero. At this point, the calculated stress and entropy from the incremental update equilibrates the system. The root-finding problem is solved using the `scipy.optimize.root` function that solves the system of nonlinear equations in a least squares sense using a modification of the Levenberg-Marquardt algorithm [114].

In simulations of a uniaxial test with heat exchange, the stress–strain relation is enforced through a hybrid approach: only the strain component along the load axis, ε_{11}, is specified; the remaining strain components are iteratively determined by zeroing their corresponding stress components in the residual to satisfy equilibrium. Using Voigt notation, the driving strain vector and its stress counterpart can be expressed as

$$\boldsymbol{\varepsilon} = \begin{bmatrix} \bar{\varepsilon}_{11} & \varepsilon_{22} & \varepsilon_{33} & \gamma_{23} & \gamma_{13} & \gamma_{12} \end{bmatrix}^{\mathsf{T}} \quad \rightarrow \quad \boldsymbol{\sigma} = \begin{bmatrix} \sigma_{11} & 0 & 0 & 0 & 0 & 0 \end{bmatrix}^{\mathsf{T}}, \tag{3.32}$$

where $\bar{\varepsilon}_{11}$ is the prescribed axial strain in the current time step. As an initial guess, other terms in the strain components were extrapolated from the previous time step.

The heat exchange with the surroundings is modeled by prescribing heat flux that drives the temperature variation to zero (towards thermal equilibrium). The adiabatic form of residual in Equation 3.31 is modified by adding a term to its entropy component,

such that

$$\boldsymbol{r}(\boldsymbol{\varepsilon}, T) = \begin{bmatrix} \boldsymbol{\sigma}_{\text{free}} \\ \rho \Delta \eta_{\text{eff}} - \Delta t \, h \frac{\theta}{T_{\text{ext}}} \end{bmatrix}, \tag{3.33}$$

where h is the heat transfer coefficient, θ is the temperature variation at the current time step, and T_{ext} is the external temperature.

3.2.3. Interaction Model for Polycrystal Simulations

In addition to the constitutive model, polycrystal simulations require an interaction model (Section 2.2.3). For its tractability, the simulations in this thesis will utilize a variant of Taylor-type (isostrain) homogenization. This method assumes that all individual grains (each modeled as a single material point) within a polycrystalline aggregate experience the same macroscopic strain as the overall specimen. Put simply, the strain is considered uniform across all grains, regardless of their crystallographic orientation:

$$\boldsymbol{\varepsilon}^{(i)} = \boldsymbol{\varepsilon} = \begin{bmatrix} \bar{\varepsilon}_{11} & \varepsilon_{22} & \varepsilon_{33} & \gamma_{23} & \gamma_{13} & \gamma_{12} \end{bmatrix}^{\mathsf{T}} \quad \text{for all } i = 1, \ldots, n_{\text{grains}}. \tag{3.34}$$

This assumption implies perfect strain compatibility between grains.

While the strain is assumed uniform, each grain will develop a unique stress state to activate the necessary deformation mechanisms to match the imposed macroscopic strain. The resulting overall stress is calculated as the weighted average of individual grain stresses:

$$\begin{aligned} \boldsymbol{\sigma} =& \frac{1}{\sum_{i=1}^{n_{\text{grains}}} w_i} \sum_{i=1}^{n_{\text{grains}}} w_i \boldsymbol{\sigma}^{(i)} \\ =& \frac{1}{\sum_{i=1}^{n_{\text{grains}}} w_i} \sum_{i=1}^{n_{\text{grains}}} w_i \begin{bmatrix} \sigma_{11}^{(i)} & \sigma_{22}^{(i)} & \sigma_{33}^{(i)} & \sigma_{23}^{(i)} & \sigma_{13}^{(i)} & \sigma_{12}^{(i)} \end{bmatrix}^{\mathsf{T}}, \end{aligned} \tag{3.35}$$

where w_i are weights that correspond to the volume fractions of each grain in the polycrystal aggregate. For simplicity, these weights are taken as equal, $w_i = 1/n_{\text{grains}}$, for all grains in the polycrystal.

Global equilibrium is satisfied, in an average sense, by iterating on the free terms in the strain vector until the corresponding terms in the global stress average is zeroed

$$\boldsymbol{\sigma} = \frac{1}{\sum_{i=1}^{n_{\text{grains}}} w_i} \sum_{i=1}^{n_{\text{grains}}} w_i \boldsymbol{\sigma}^{(i)} \approx \begin{bmatrix} \sigma_{11} & 0 & 0 & 0 & 0 & 0 \end{bmatrix}^{\mathsf{T}}. \tag{3.36}$$

In practice, this means that, for each time increment, the strain components not directly prescribed by boundary conditions are adjusted iteratively across all grains in the polycrystal aggregate. After each update, the stress response of every grain is computed, and the volume-weighted average of these stresses is evaluated. The process continues until the unconstrained components of the averaged global stress vector converge to zero within a specified tolerance, ensuring that the polycrystal as a whole is in mechanical equilibrium under the imposed loading. By enforcing this condition, the Taylor-type homogenization approach guarantees compatibility of strain and equilibrium of stress at the aggregate level, even though individual grains may experience distinct local stress states due to their crystallographic orientations.

The system's entropy is also calculated as a volume-weighted average of the individual grain entropies, analogous to the stress averaging. The combined global stress equilibrium and heat exchange problems thus take the same form as Equation 3.33 and are solved accordingly, as described in Section 3.2.2.1.

It is important to note that the hybrid Taylor-type averaging approach employed in this work differs fundamentally from conventional iso-strain methods. In classical iso-strain (full Taylor) homogenization, the entire strain tensor is prescribed identically for all grains, meaning every component of the strain vector is fixed by boundary conditions and imposed uniformly across the aggregate. This assumption enforces perfect strain compatibility but does not allow for any redistribution of strain components in response to the evolving internal stress state of the polycrystal.

In contrast, the hybrid approach used here prescribes only the axial component of the strain (typically corresponding to the loading direction), while the remaining

strain components are treated as free variables. These unconstrained components are iteratively adjusted so that the corresponding averaged global stress components are driven to zero, thereby satisfying equilibrium. This procedure allows the polycrystal to internally redistribute transverse and shear strains in response to the anisotropic activation of deformation mechanisms within individual grains. As a result, the hybrid method more accurately captures the mechanical response of the aggregate under realistic boundary conditions, especially in cases where lateral or shear constraints are absent or minimal.

By allowing the non-axial strain components to evolve according to the equilibrium condition, the hybrid Taylor-type averaging approach provides a more flexible and physically representative framework for simulating polycrystalline deformation. This is particularly advantageous for modeling uniaxial tests, where only the axial strain is controlled, and the material is free to contract or expand laterally. In summary, while iso-strain methods enforce uniform strain in all directions, the hybrid approach enforces uniformity only in the prescribed direction and achieves equilibrium in the remaining directions through iterative adjustment, resulting in a more realistic simulation of polycrystal behavior.

3.3. Experimental

This section describes the experimental setup and procedures used to validate the crystal plasticity model. The experiments are designed to capture the thermomechanical response of magnesium alloys under various loading conditions, including slip and twinning behavior.

3.3.1. Experimental Setup

The experimental setup integrates advanced imaging and mechanical testing capabilities for synchronized deformation and temperature measurements (Figure 3.1). The core components include a FLIR A655sc thermal camera (Figure 3.1b) equipped

with an uncooled bolometer, fitted with a 1.5X close-up IR lens, providing 25 μm/pixel geometric resolution. Accompanying that is a macro-DIC imaging line (Figure 3.1a), which incorporates a 1X Edmund Optics zoom inspection microscope (Figure 3.1b). The camera assembly is positioned vertically above a Kammrath & Weiss 10 kN tension–compression module (Figure 3.1d), which applies load through symmetric extension/contraction of crossheads at rates up to 20 μm/s. The loading frame is mounted on top of a Newport X–Y–Z positioning stage (Figure 3.1e), enabling precise positioning of the sample under different imaging lines. The entire assembly sits on a vibration isolation table, and enclosed within an opaque curtain (Figure 3.1f) to eliminate ambient light interference during thermal measurements.

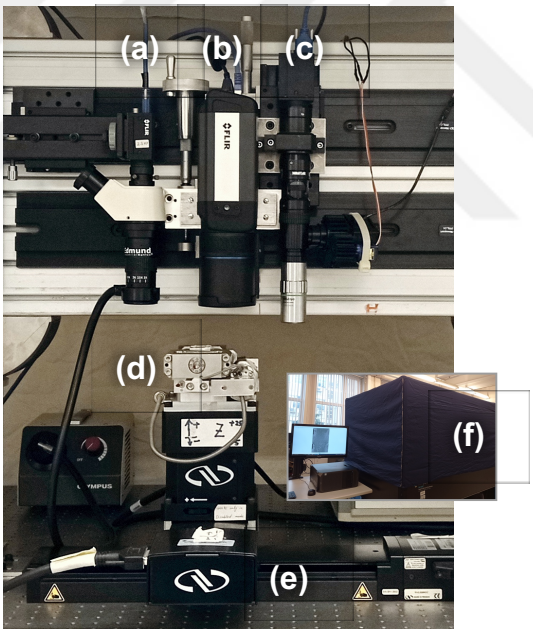


Figure 3.1. Experimental setup for in situ infrared thermography measurements: (a) macro-DIC imaging line; (b) thermal camera; (c) micro-DIC imaging line (not used here but historically relevant, see text); (d) tension-compression loading frame; (e) X–Y–Z positioning stages; (f) outside view of the entire setup covered with an opaque curtain that sits on a vibration isolation table.

The loading setup is slightly modified later for single crystal compression tests to mount the approximately $4 \times 2 \times 2$ mm^3 samples (Figure 3.2c). Custom compression bulk heads were manufactured out of tempered steel, and cylindrical neodymium magnets

are glued to them. At the compression surface, disks that are cut out of microscope glass are glued to the magnets, and any metal-to-metal contact surface between the sample and the setup is blocked entirely (Figure 3.2b). The compression heads and the attached glass disks are painted black (taking extra care to avoid painting the compression surface itself) to prevent reflections and ensure a uniform emissivity.

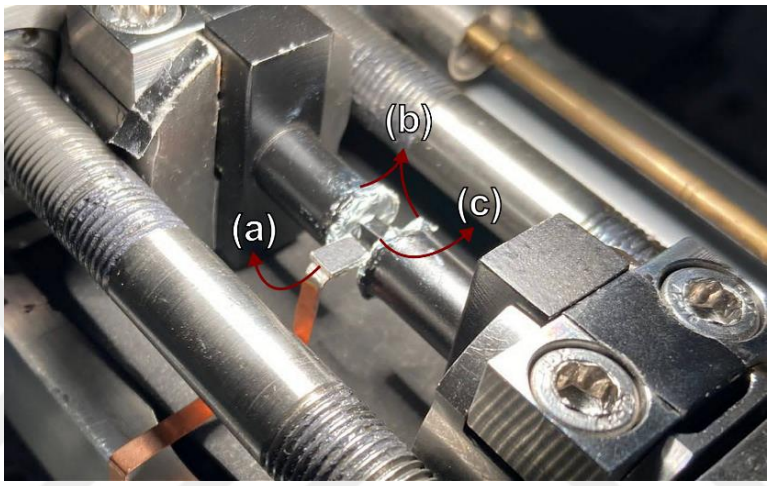


Figure 3.2. Modified setup for single crystal Mg compression tests. (a) is a stress-free piece of Mg, attached to a copper strip; (b) are the glass disks that insulate the sample from the tension–compression module. White lithium grease is applied to the glass surface to prevent friction. (c) is the single crystal specimen.

3.3.2. Sample Preparation

3.3.2.1. Magnesium AZ31. For the polycrystalline magnesium, dog-bone samples were wire-EDM cut along the rolling direction from an Alfa Aesar hot rolled magnesium AZ31 plate. The gage sections of the samples feature a 3×3 mm^2 square cross-section, designed to prevent buckling about either axis. Figure 3.3a shows a top-view IRT image of the sample alongside a free-hanging piece of the same material serving as a stress-free IRT reference. Both surfaces were treated identically with a thin coat of black paint to ensure uniform and high (close to 1) emissivity. A representative image of the sample, recorded by the macro-DIC line (under Figure 3.1a) is shown in Figure 3.3b.

3.3.2.2. Single Crystal Magnesium. A 20 mm diameter, 2 mm thick disk was procured from Princeton Scientific Corporation. The disk was specifically chosen with a $\langle 11\bar{2}0 \rangle$ (an a-axis of the unit cell) as the orientation aligned with the disk's normal. The selection of $\langle 11\bar{2}0 \rangle$ orientation was a strategic decision to obtain multiple crystallographic orientations from a single disk, which is ideal for the purposes of this thesis. To maximize the number of test pieces, smaller compression samples were machined from the disk instead of larger dog-bone specimens.

With the $\langle a \rangle$-axis normal, the two orthogonal in-plane directions become accessible: $\langle 0001 \rangle$ and $\langle 10\bar{1}0 \rangle$, corresponding to the $\langle c \rangle$-axis of the crystal and the prismatic plane normal, respectively. Samples cut for compression along these axes offer a distinct contrast: the sample with the $\langle 0001 \rangle$ compression axis (denoted as $c^{\parallel}$) will preclude twinning and necessitate deformation via the harder mechanism of $\langle c+a \rangle$ pyramidal slip; conversely, the sample with the $\langle 10\bar{1}0 \rangle$ compression axis (denoted as $c^{\perp}$) is well-suited for tensile twinning, exhibiting a maximal Schmid factor close to 0.5. The comparison between these two sample types aims to provide a sharp contrast between twinning and non-twinning behaviors.

While the normal direction of the disk was known upon receipt, the in-plane directions necessary to extract samples with the desired pattern had to be determined via diffraction. For this purpose, a three-axis Bruker Discover X-ray diffractometer (XRD), located at Boğaziçi University's Chemical Engineering SNG&HydTec Laboratory, was used. The XRD was equipped with an additional sample rotation axis (ϕ, about the sample normal). Once the sample c-axis direction is determined and marked, the disk was precisely oriented in the wire-EDM machine to yield the desired $\langle 10\bar{1}0 \rangle$ and $\langle 0001 \rangle$ compression samples. The compression samples, both with a square cross-section of 2×2 mm^2, have lengths of 4 mm and 4.2 mm for the $c^{\parallel}$ and $c^{\perp}$ samples, respectively.

Similar to the polycrystal IRT samples, the observation surfaces of single-crystal samples were lightly polished and then coated with black spray paint. By their nature, IRT experiments, which capture transient temperature signals, must be conducted in

real time under an IRT camera. In contrast, DIC is performed using reference and final point images to provide a detailed depiction of the overall deformation [52, 115, 116]. Even with the black coating, the contrast variations within it still yielded a suitable DIC pattern for macroscopic analysis.

3.3.3. IRT Experiment Procedure

All IRT experiments are conducted at room temperature with specimens initially at thermal equilibrium. Tests are performed at the maximum attainable crosshead speed of the loading frame. During loading, the thermal camera records at 100 Hz, capturing 640×240 px^2 images. Load cell and crosshead position signals are acquired synchronously with the IRT images using a National Instruments BNC-2110 block. Before and after loading, positioning stages (Figure 3.1e) move the loading frame under the macro-DIC line (Figure 3.1a). The images captured before and after loading are subsequently compared using DIC to calculate final-point strains. During actual loading, the specimen is positioned under the IRT camera (Figure 3.1b), where the transient temperature signal is continuously recorded in situ.

3.3.3.1. Polycrystalline Compression–Tension Tests. Two specimens, named A and B, are subjected to identical initial compression ramps, labeled A0 and B0 in Figure 3.3c. Following thermal equilibration and macro-DIC imaging, the tension ramp for specimen A (A1) begins from this loading point. In contrast, specimen B is manually unloaded before starting the tensile ramp (B1). Specimen A1 represents a cyclic loading study, while specimen B1 explores a twin-infused material state that can be removed from the grips after unloading and analyzed separately. The compression–tension loading is executed using position-controlled ramps for each stage. The crosshead speed corresponds to a nominal strain rate of 2×10^{-3} s^{-1} for the dog-bone specimens.

A representative DIC image is shown in Figure 3.3b, and the resulting strain fields at the end of A0 and A1 ramps are presented in Figure 3.3c. For the energy balance analysis, a standardized 6×2.5 mm^2 averaging box is defined centered on the specimen,

outlined in red in both IRT and DIC fields of Figures 3.3a and b. The temperature averaged from the box outlined in green in Figure 3.3a on the other hand serves as a reference for the gage section temperature.

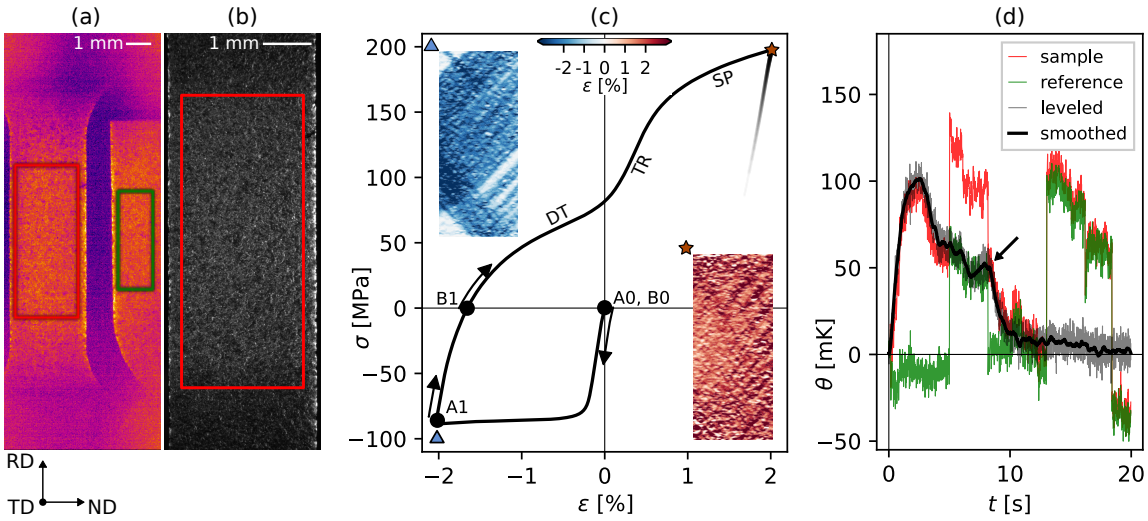


Figure 3.3. (a, b) IRT and DIC-camera images of Mg AZ31 sample A, with red and green boxes indicating gage and temperature averaging regions, respectively. (c) Cyclic stress–strain curve showing ramp loading (compression, tension) and embedded axial DIC-strain maps at cycle endpoints. (d) Sample mean gage temperature over time, baselined by dummy sample temperature and filtered.

Given the tension–compression asymmetry in deformation regimes, complementary live-DIC experiments are conducted with identical ramp loading. These experiments, performed under the macro-DIC camera with real-time strain calculation, are used to calibrate target crosshead positions to achieve ±2% gage-box averages in the IRT experiments. In these complementary live-DIC experiments, which are conducted entirely under the macro-DIC camera (without an IRT component), necessary instrumentation is implemented such that loading is stopped when live-measured DIC strain reaches the target value.

The engineering stress versus gage-section average strain results produced in these experiments over consecutive compression–tension–compression–... loads are

exemplified in with a three-dimensional plot for a clearer presentation in Figure 3.4. Interim strains from these complementary experiments validate the interim strains in IRT experiments obtained by DIC analysis of IRT images. As part of the standardization process, all specimens are mounted carefully to ensure identical grip-to-gage section lengths.

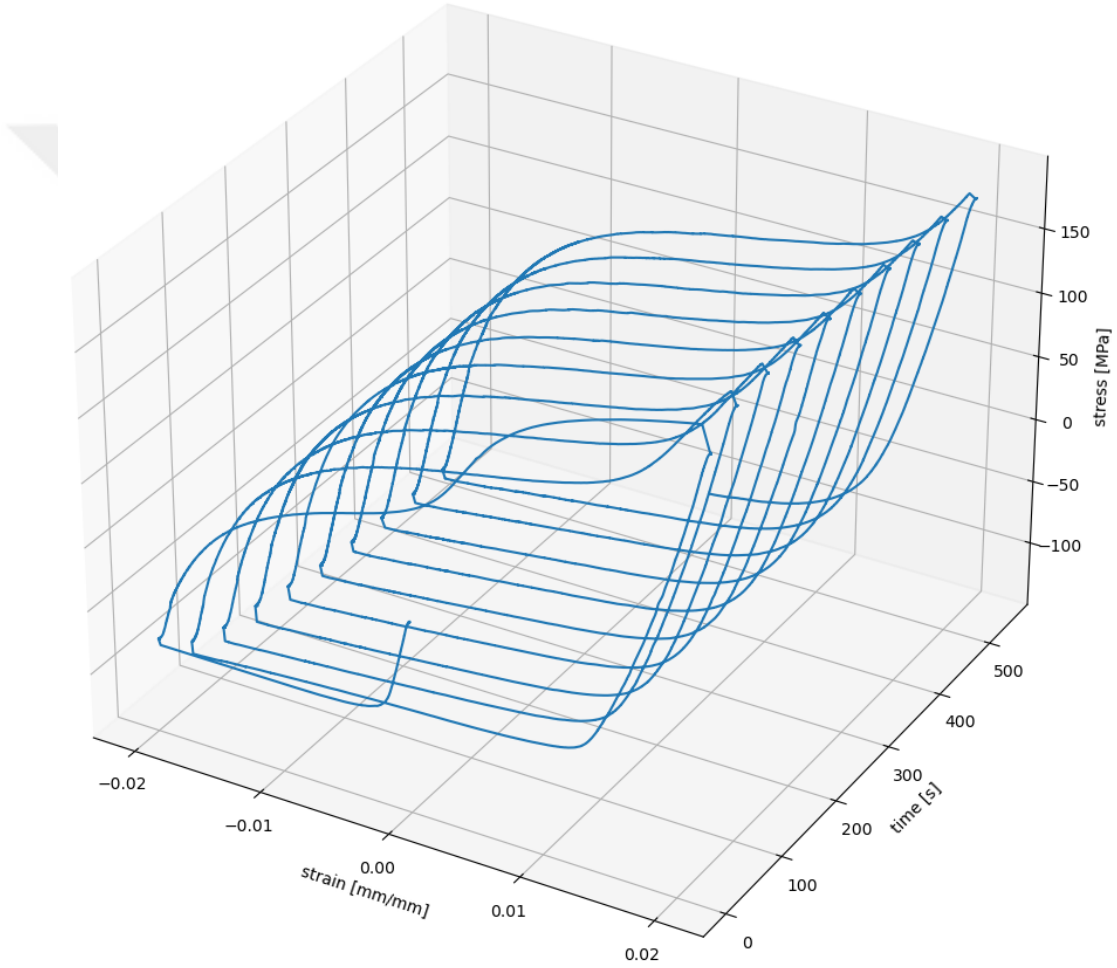


Figure 3.4. Stress versus strain on consecutive compression-tension cycles with live-DIC experimentation. The third (time) axis is inserted to distinguish individual cycles.

The representative stress–strain curve of the experiments is shown in Figure 3.3c over the reversed loading path, exhibiting the features unique to this material: a twinning plateau over the first compression, and most notably, the eccentric sigmoidal shape on the following tension. This behavior is mechanistically composed of the reverse

twin transformation (detwinning, DT) on Figure 3.3c and, upon its exhaustion, slip plasticity (SP), with a transition region (TR) in between [10, 117, 118]. Equivalent samples from the same batch (its basal texture in [60, 119]) and form factor have been utilized as in previous works from the same setup [10, 58–60] for continuity. Thus, a very detailed depiction of the spatial aspects of strain accommodation over the reversed load in Figure 3.3c with full-field microscopic detail (as investigated by the microscopic line, Figure 3.1c) is available (Shafaghi et al. [59]) with stepwise in situ data collection.

3.3.3.2. Single Crystal Compression Tests. These compression tests explore the thermomechanical behavior of slip and twinning in single-crystal magnesium. The $c^{\parallel}$ specimen is expected to deform primarily through pyramidal slip, while the $c^{\perp}$ specimen is anticipated to exhibit tensile twinning followed by slip-dominated deformation.

The single-crystal specimens, shown in Figure 3.2c, are carefully placed between the compression heads and suspended using the adhesion from white lithium grease applied on glass compression pads (Figure 3.2b). The compression heads are carefully closed to avoid premature deformation, a critical step, especially for the $c^{\perp}$ specimen, given the ease with which tensile twins are activated in this configuration. A piece of black spray-painted magnesium is attached to the side surface of the setup with a copper strip to serve as a stress-free reference for temperature measurements (Figure 3.2(a)).

The crosshead speed corresponds to a nominal strain rate of 5×10^{-3} s^{-1} for the single-crystal specimen geometry. The $c^{\parallel}$ specimen is loaded to approximately 3.5% compressive strain, while the $c^{\perp}$ specimen is loaded to approximately 10% compressive strain to ensure complete tensile twin exhaustion and sufficient progression into slip-dominated deformation.

For single crystal samples, IRT images of the entire 4×2 mm^2 observation surface are used in DIC analysis to calculate the average compressive strain, treating the whole surface as a single subset that deforms affinely. The resulting DIC deformation data are then used to align the temperature averaging box, ensuring accurate measurements

despite the large deformation present in these tests.

3.3.4. Processing of Experimental Data

The treatment of the temperature data is illustrated in Figure 3.3d, where the load is applied until the marker arrow, followed by thermal equilibration. First, the sample data are leveled using data from the stress-free reference. This allows for eliminating spurious fluctuations in thermal sensor readings that arise from the use of an uncooled bolometer (see Figure 3.3d). Next, the noise floor of about 10 mK is filtered out by a quadratic Savitzky–Golay filter [114] with window sizes corresponding 0.5 s and 2.0 s of data for polycrystal samples and single-crystal samples, respectively.

Table 3.1. Elastic and thermal properties utilized for pure magnesium [a] [120], [b] [121] and for magnesium AZ31 [c] [122], [d] [123].

Mg	E [GPa]	ν	α [1/K]	ρ [kg/m^3]	k [W/m·K]	C_p [J/kg·K]
pure	45.0[a]	0.29[a]	26.1×10^{-6} [b]	1740[b]	156.0[b]	1024.0[b]
AZ31	41.6[c]	0.29[c]	24.4×10^{-6} [c]	1754[d]	84.7[d]	1005.9[d]

The material constants used for pure magnesium and AZ31 are presented in Table 3.1. Regarding the use of isotropic elastic constants, the near-elastic isotropy of this material should be noted, contrasting its extreme plastic anisotropy. The zero-dimensional energy balance equation (see e.g. [95, 124]) suited to a uniaxial test has the form

$$\beta \underbrace{\sigma \dot{\varepsilon}_{\mathrm{pl}}}_{W_a} \underbrace{-\alpha_{\mathrm{th}} T(\dot{\sigma} + 9\kappa\alpha_{\mathrm{th}}\dot{\theta})}_{W_{the}} = \underbrace{\rho C \dot{\theta}}_{W_c} + \underbrace{\frac{\rho C \theta}{\tau_{\mathrm{eq}}}}_{W_l}, \tag{3.37}$$

where, aside from material properties provided in Table 3.1, σ is the uniaxial stress; $\varepsilon_{\mathrm{pl}} = \varepsilon - \sigma/E$ is the plastic strain; T is the (leveled) temperature averaged over the sample gage section; κ is the bulk modulus; $\theta = T - T_0$ is the temperature variation from its initial value; τ_{eq} is the time constant approximating conductive losses from grips and convective losses from free surfaces; β and is the instantaneous ratio of

dissipation ($W_d = W_c + W_l - W_{the}$) to plastic power ($W_a$). Here, W_l represents losses (note that Equation 3.37 is a non-adiabatic form necessary for moderate strain rates), W_c is thermal energy rate, and W_{the} is the thermoelastic contribution. The sense of thermoelastic effect switches with loading sense, making it a cooling effect in tension but a heating effect in compression. A detailed derivation of the 0D energy balance equation is provided in Appendix A.

3.4. Parameter Calibration and Model Validation

Single-crystal compression simulations are conducted on a single material point, with compression axes aligned along the $\langle 0001 \rangle$ and $\langle 10\bar{1}0 \rangle$ directions for the $c^{\parallel}$ and $c^{\perp}$ samples, respectively.

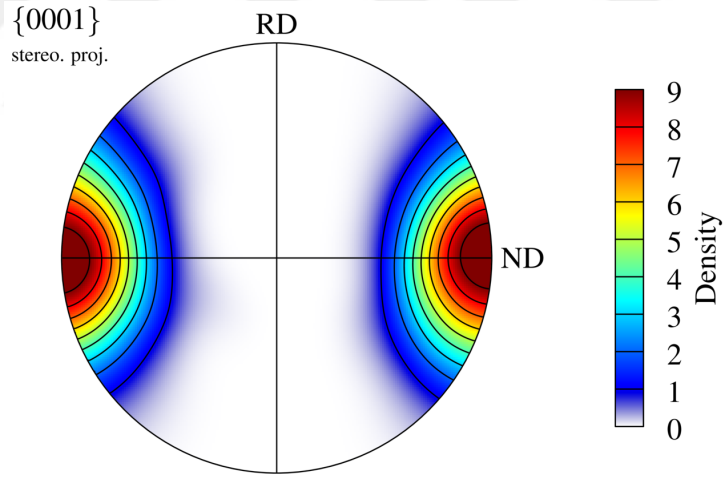


Figure 3.5. Pole figure of the polycrystal orientation distribution used in the simulations. RD is aligned with the loading axis.

In contrast, polycrystal simulations employ a Taylor-type polycrystal model with 1100 grains; though polycrystals with fewer grains are also used to expedite the parameter calibration process. Polycrystals with as few as 63 or 14 grains prove sufficient, depending on the stability of the model parameters. The choice of a large number of grains is justified for visualizing the directional distribution of dissipative properties (see Section 4.3.2).

The polycrystal orientation distribution is generated using Neper's fiber texture function [125]. The $\langle 0001 \rangle$ direction of each grain in the polycrystal is aligned with the normal direction (ND), incorporating a 15° spread to represent cold rolling texture [126]. Figure 3.5 shows the pole figure of the resulting texture (for comparison, see the pole figure in [60] of the same Mg plate). The rolling direction (RD) is then oriented to the loading axis, and the transverse direction (TD) is aligned with the observation surface for the simulation. (Note that in the Taylor-type polycrystal homogenization, there is no actual surface definition as with FEM; the orientation assignment is purely for convenience.)

Calibration and validation of the crystal plasticity model are done using stress–strain curves and β evolution obtained from the IRT experiments. While the mechanical calibration is relatively straightforward, calibrating the model's energetic response requires careful processing of both the experimental (as described in Section 3.3.4) and the simulation results to extract β.

As discussed in Section 2.3, many traditional thermomechanical models assume that the fraction of plastic work dissipated as heat is constant, typically taking values of 0.8–1.0 for most materials. However, this assumption is generally not accurate [92]. A key advantage of the variational framework is its ability to enable an a posteriori calculation of the evolution of β predicted by the model, rather than requiring an a priori assumption [110]. For a single crystal, β can be computed using the following expression, adapted from [38]:

$$\beta = \frac{\boldsymbol{\sigma} : \dot{\boldsymbol{\varepsilon}}_p - \frac{\partial W_p}{\partial \boldsymbol{\epsilon}} \dot{\boldsymbol{\gamma}} - \frac{\partial W_p}{\partial \boldsymbol{\lambda}} \dot{\boldsymbol{\lambda}}}{\boldsymbol{\sigma} : \dot{\boldsymbol{\varepsilon}}_p}, \tag{3.38}$$

where $\boldsymbol{\sigma} : \dot{\boldsymbol{\varepsilon}}_p$ represents the plastic power—the rate of mechanical work done to the material. The remaining terms in the numerator correspond to the rates at which energy is irreversibly stored in the material due to plastic slip and twinning, respectively. For the polycrystal (using Taylor approximation), the terms in both the numerator and denominator of Equation 3.38 are simply replaced with their volume-weighted averages over all grains.

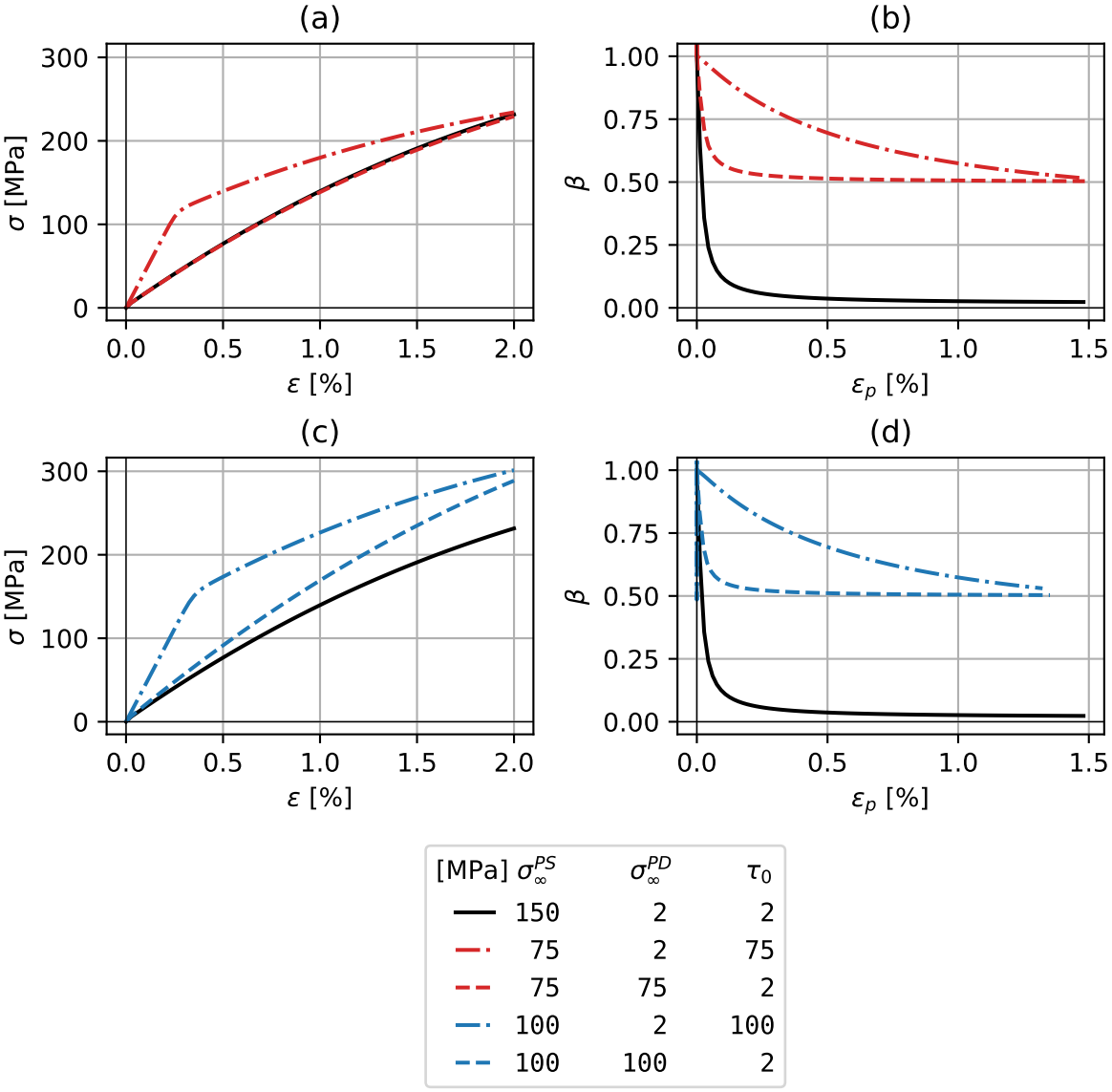


Figure 3.6. (a), (c) Stress vs strain and (b), (d) β vs plastic strain curves demonstrating the affect of different material parameters.

An example characterization of the mechanical and energetic response of the model is shown in Figure 3.6, to demonstrate the ability of modifying σ and β through the alteration of specific material parameters. For this purpose, a single material point is loaded to 2% strain with different sets of material parameters for $\langle c+a \rangle$ pyramidal slip in a simple uniaxial compression simulation along $\langle c \rangle$ direction. This loading orientation results a positive resolved shear stress (RSS) only on the pyramidal slip systems.

By strategically adjusting the material parameters σ_0, $\sigma_\infty^{\mathrm{PS}}$, $\sigma_\infty^{\mathrm{PD}}$ and τ_0, the model's overall dissipative character can be modified independently of its mechanical response, and vice versa. Specifically, the sum $\sigma_{\mathrm{total}} = \sigma_0 + \sigma_\infty^{\mathrm{PS}} + \tau_0 + \sigma_\infty^{\mathrm{PD}}$ influences the maximum stress, while the ratio $(\tau_0 + \sigma_\infty^{\mathrm{PD}})/\sigma_{\mathrm{total}} = \sigma_{\mathrm{diss.}}/\sigma_{\mathrm{total}}$ determines the Taylor–Quinney coefficient.

Figures 3.6a and b illustrate how the final stress value can be held constant by fixing $\sigma_{\mathrm{total}} \approx 150$ MPa, even as β is adjusted (from approximately 0 to 0.5 in this case). Conversely, Figures 3.6c and d demonstrate that saturation stresses can be increased by raising σ_{total} to 200 MPa, while maintaining β constant at 0.5. (Note that σ_0 is set to 0 in all five cases shown in Figure 3.6.)

The mechanism by which the β value is increased significantly affects both the stress–strain and Taylor-Quinney coefficient-strain curve characteristics. When β is increased primarily through viscous dissipation (VD) via τ_0, both curves exhibit altered characteristic forms. Most notably, a distinct yield point emerges in the stress–strain curves, particularly when the rate dependence exponent is low ($m = 0.05$ in this case). Under these conditions, τ_0 together with σ_0 controls the initial critical resolved shear stress (CRSS). In contrast, when β is increased predominantly through plastic dissipation (PD) via $\sigma_\infty^{\mathrm{PD}}$, the gradual, exponential hardening response in the stress–strain curves is preserved. For further discussion on the relevance of these observations, the reader should refer to Section 4.3.1.

While manually adjusting the combined mechanical and dissipative response of the model is straightforward for simple test cases involving the activation of only a single slip system variant, this approach becomes impractical for more complex loading scenarios. For instance, in a magnesium polycrystal featuring multiple slip and twin systems, modifications to model parameters can inadvertently alter relative slip/twin system activity, leading to nonlinear changes in the resulting material response. Therefore, after an initial manual approximation of the experimental response, the model parameters are further refined using a least-squares optimization algorithm.

This algorithm minimizes the discrepancy between the experimental and simulated stress–strain curves, as well as the evolution of the Taylor–Quinney coefficient. This optimization is efficiently performed using the `optimize.least_squares` function from the SciPy library [114, 127].

The proposed model is further verified by inspecting slip and twin activity, comparing the apparent Poisson's ratio of the resulting strains, and analyzing the temperature variations during deformation against their experimentally measured counterparts. This last point necessitates characterizing the simulated heat exchange with the environment. The heat exchange coefficient, h, is calculated by combining heat exchange term in Equation 3.33 with the zero-dimensional loss term in Equation 3.37, and by noting that $T_0 = T_{\text{ext}}$,

$$h = \frac{\rho C}{\tau_{\text{eq}}}. \tag{3.39}$$

The validity of this heat exchange parameter is also confirmed by matching the simulated temperature decay to experimental data (though this is not shown in the current manuscript).

4. RESULTS

4.1. Polycrystalline Mg AZ31 Compression–Tension Experiments

The stress versus strain results for the samples are presented in Figure 4.1a and b. Figure 4.1a shows the initial compressive load segments A0, B0, while Figure 4.1b shows the subsequent tensile stages A1, B1. The tangent moduli at various points of interest are shown on these curves, with the initial Young's modulus calculated in Figure 4.1a in large agreement with the literature value (Table 1). Corresponding temperature variation (θ) results are plotted versus strain in Figure 4.1c and d. The initial compressive ramps A0, B0 are equivalent, and their data serves as a successful confirmation of each other in both Figure 4.1a and c. The initial bump in temperature, marked with an arrow in Figure 4.1c is due to the thermoelastic effect that is positive in compression. After this, the temperature also goes to a plateau over the twinning-dominated deformation regime.

On the following tensile straining, the first obvious disparity (in Figure 4.1d) between the A1 and B1 load ramps is the lower initial strain in B1 (at about -1.6%) due to the strain released during the unloading from -2%.

Although both curves exhibit an initial thermoelastic effect that is now cooling-type (indicated by single arrows over A1 and B1 in Figure 4.1d), the cooling dip is more pronounced in A1. This is due to the additional thermoelastic effect during the unloading, which occurs primarily through elastic strain release. As shown in Figure 4.1b, the tangent modulus of 38 GPa during the initial stretch of unload approaches the elastic modulus (42 GPa). The initial thermoelastic effect is particularly subdued in B1, since there is no pure elastic behavior in this region. Similarly, the low tangent modulus of 12 GPa in Figure 4.1b at the start of this segment (B1) reflects this behavior. Moreover, the complementary activity with detwinning (and surrounding plasticity) would synchronously generate heat and counteract the thermoelastic cooling.

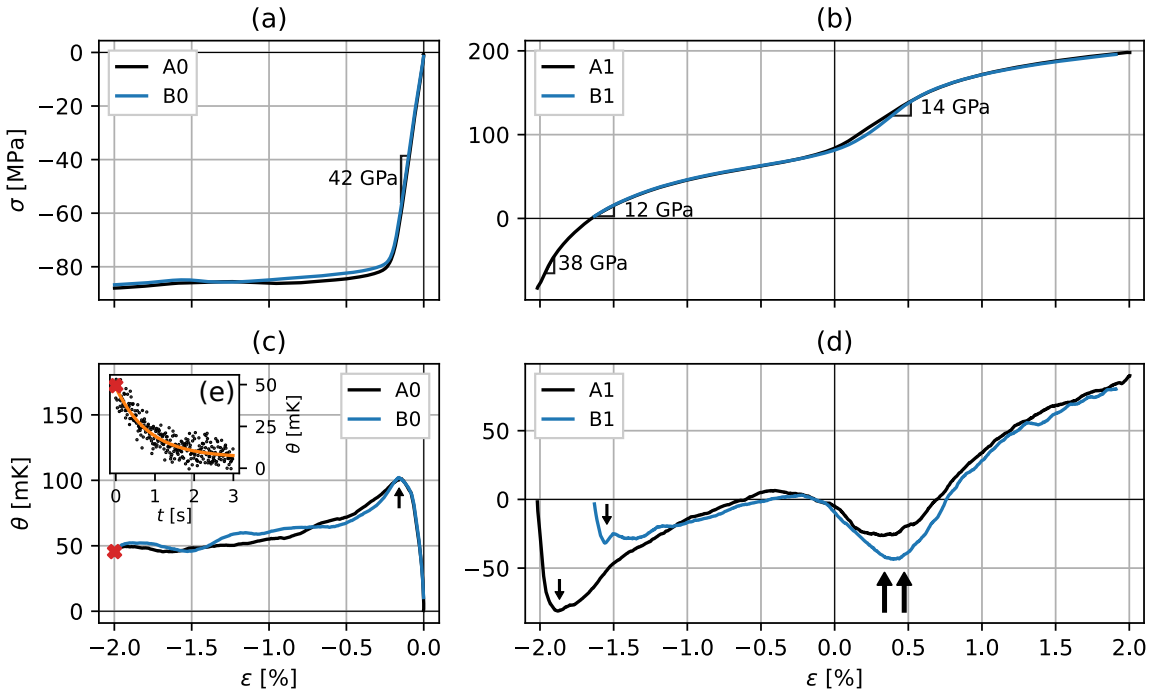


Figure 4.1. Stress and average temperature measurements plotted against average strain for samples A and B over load ramps (A0, B0, A1, B1) defined in Figure 3.3c. Stress plots over (a) A0, B0, (b) A1, B1; temperature plots over (c) A0, B0, (d) A1, B1. (e) exponential fit of temperature decay following the end of the load ramp A0 marked with a '×' sign.

During the detwinning segment under tensile stress, the temperature in both A1 and B1 gently increases until about zero strain. At this point, the temperature dips a second time in both curves, marked by bold double arrows. The only energy contribution in Equation 3.37 that can cause this temperature drop is the thermoelastic effect. Thus, the curves clearly show a distinct secondary thermoelastic effect in the transition region between the end of detwinning and the onset of slip plasticity. The heating introduced by the latter causes a sharp temperature rise in the rest of the straining until +2%.

It is highly unusual for a material to show a secondary thermoelastic effect at an intermediate point along a load path. The typical absence of this behavior is further exemplified in the literature using a titanium sample (the more common structural metal

with hexagonal symmetry) produced in the same geometry and loaded analogously over the cyclic path [128]. The unique secondary thermoelastic dip in the transition region of magnesium can be explained by the lack of any slip mechanisms operating at the same low stress level as detwinning. Once detwinning is physically exhausted—i.e., with all possible twin lamellae reverted to the parent grain's orientation—the stress must first rise to the level that activates large-scale slip. Nevertheless, the behavior in this transition region is not purely elastic, as evidenced by the tangent moduli (the maximal moduli of 14 GPa in this region shown in Figure 4.1b is considerably lower than 42 GPa) and arguments in literature [117, 118]. Hence, how pronounced these dips are quite interesting and worthy of being added to the peculiarities of magnesium response.

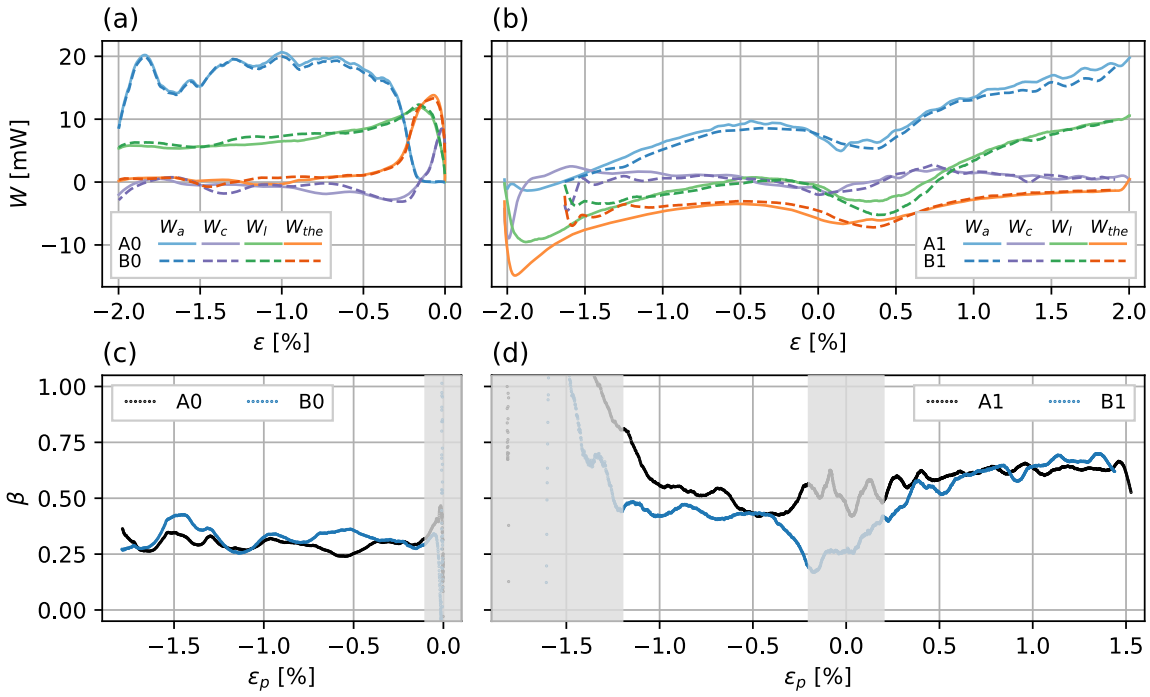


Figure 4.2. Energy balance terms (Eq. 3.37) for (a) compression (A0, B0), and (b) tension (A1, B1) load ramps. Taylor–Quinney coefficients for (a) compression (A0, B0), and (b) tension (A1, B1).

For the energetic analysis of the data using Equation 3.37, τ_{eq} is first determined to be 0.85 seconds by fitting an exponential decay [129, 130] to the temperature data (Figure 4.1e) after the loading is stopped (Figure 3.3d). The strain and load (stress)

channels are also smoothed using Savitzky-Golay filters, similar to the temperature data. The resulting energy components of Equation 3.37 (after multiplication with the gage volume to obtain units of mW) are shown in Figure 4.2a and b for the compressive (A0, B0) and tensile (A1, B1) load segments, respectively. The respective ratio of dissipation to plastic power, $\beta = W_d/W_a$, also known as Taylor–Quinney coefficient [91] is presented in Figure 4.2c and d. Through error analysis, it is noted that in the segments where the denominator term, W_a, is low, the value of β becomes uncertain. These regions are shaded gray in Figure 4.2c and d. In these segments, e.g., in the transition region of Figure 4.2d, elastic effects are prominent, and it is nevertheless not meaningful to investigate the dissipated component of plastic work.

Measurements over Figure 4.2c and d demonstrate that β varies significantly with changes in the dominant deformation mechanism. In the twin-dominated deformation region, β values are notably lower, at approximately 0.3 (Figure 4.2c), while in the slip plasticity segment, values increase to around 0.6 (Figure 4.2d). These values are broadly consistent with previous high strain-rate studies [105]. Samples A and B show strong agreement in both compression and tension, supporting the consistency of these findings. Additionally, this study provides original data on β during non-monotonic loading, revealing values of approximately 0.5 in the detwinning segment preceding the transition region, with consistent values between A1 and B1.

It is worth noting that these findings also do not support the historical practice of using 0.9 as a convenient approximation for β following Taylor and Quinney's work [91]. As stated in literature [92, 105], β is not a fixed parameter but depends on deformation history, material properties, loading conditions, and specific deformation mechanisms [131].

4.2. Pure Magnesium Single Crystal Compression Results

The $c^{\parallel}$ single-crystal sample (Figure 4.3b) was compressed along the c-axis for approximately 9.2 seconds as indicated in Figure 4.3a. This compression resulted

in an average compressive strain of 3.24% as measured by the macro-DIC analysis (Figure 4.3c). The apparent Poisson's ratio was calculated to be 0.586, which approaches the ideal value of 0.5 for isotropic plastic deformation.

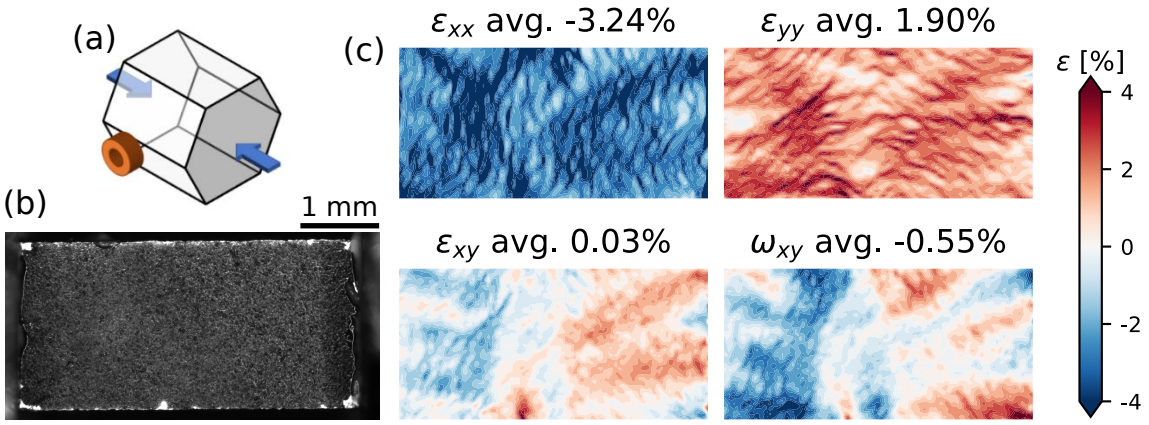


Figure 4.3. (a) Load direction (blue arrows) and observation angle (orange disk) with respect to the crystal, (b) macro-DIC image, (c) macro-DIC strain fields of the $c^{\parallel}$ single-crystal compression sample.

Analogously, the $c^{\perp}$ single-crystal sample (Figure 4.4b) was compressed perpendicular to the c-axis for approximately 22.5 seconds as indicated in Figure 4.4a. After loading, the $c^{\perp}$ sample was accommodating more than 10% compressive strain. The apparent Poisson's ratio of approximately 0.88 (very close to 1) indicates significant in-plane deformation due to twinning. However, the macro-DIC strain maps in Figure 4.4c do not show any twin bands typical of magnesium, because the sample was compressed approximately 3.5% beyond the exhaustion of twinning at 6.5% transformation strain, and twin band signatures are likely obscured by subsequent plastic deformation.

Figure 4.5 shows the stress and temperature history of single-crystal samples with respect to the overall axial strain. Note that the loading follows these curves go from right-to-left to signify the loading sense. Also note the agreement of the end-point strain values from IRT-DIC measurements with the macro-DIC strain measurements in Figure 4.3c and Figure 4.4c, for the $c^{\parallel}$ ($\approx 10.5\%$) and $c^{\perp}$ ($\approx 3\%$) samples, respectively.

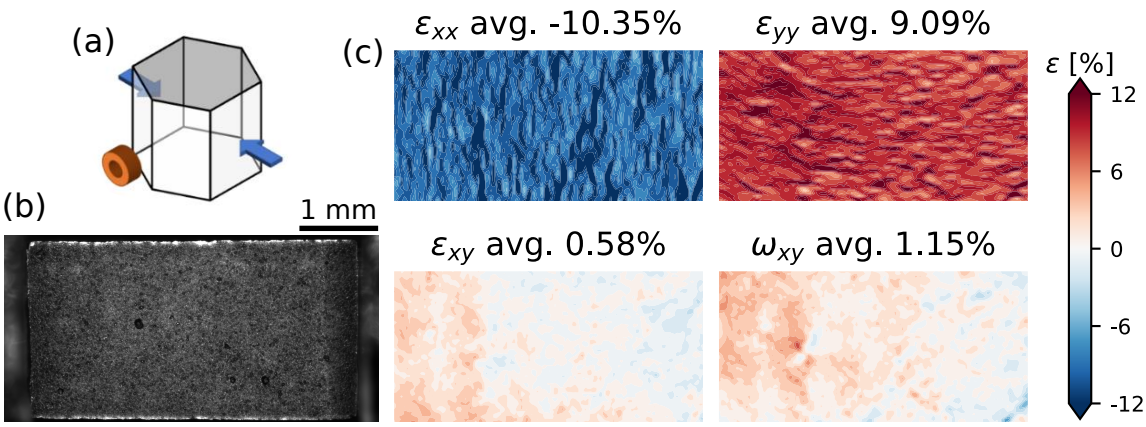


Figure 4.4. (a) Load direction (blue arrows) and observation angle (orange disk) with respect to the crystal, (b) macro-DIC image, (c) macro-DIC strain fields of the $c^{\perp}$ single-crystal compression sample.

The $c^{\parallel}$ sample shows a typical compressive response with a smooth stress–strain curve showing no apparent yield point (Figure 4.5b), reaching approximately 250 MPa at the end of loading. The corresponding temperature–strain curve (Figure 4.5d) displays a similar profile, with the sample heating to approximately 600 mK above the ambient temperature.

In contrast, the behavior of the $c^{\perp}$ sample is remarkably different. It reaches 6.5% compressive strain (twin transformation strain) with a twin plateau of only 40 MPa at peak stress, beyond which the stress rises sharply (Figure 4.5a) with an initial tangent stiffness of 14 GPa. During the twin plateau, the temperature rises to just about 20 mK above the ambient temperature (Figure 4.5c). Following the twin plateau, the temperature rise accompanies mechanical hardening of the material, reaching to nearly 800 mK above the ambient temperature at the end of the loading. The temperature exhibits a small rise just before the end of the twin plateau, marked with an arrow in Figure 4.5c. This may indicate difficulties in strain accommodation by twinning, and the approaching onset of slip plasticity.

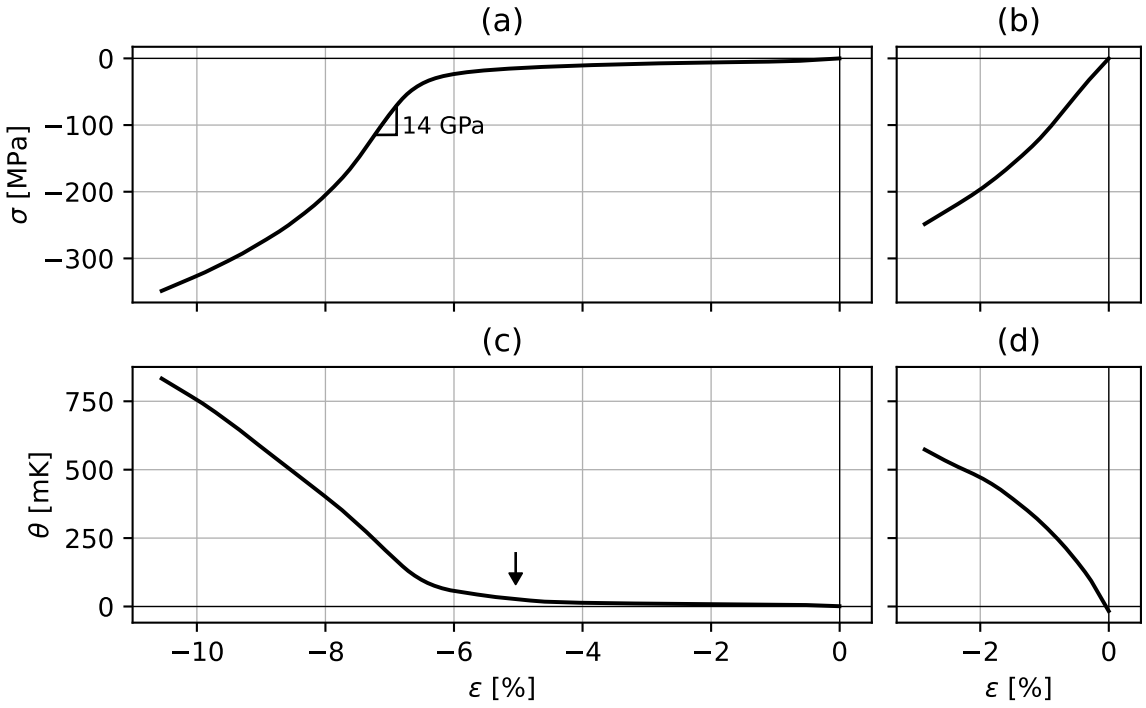


Figure 4.5. Stress and average temperature measurements plotted against average strain for samples $c^{\perp}$ and $c^{\parallel}$. (a), (b) stress–strain and temperature–strain curves for $c^{\perp}$; (c), (d) stress–strain and temperature–strain curves for $c^{\parallel}$.

Figure 4.6 shows the post-processed temperature signal together with the raw box averages from the sample and stress-free reference. These figures demonstrate that the thermal output of single-crystal samples are significantly higher than the polycrystalline samples. This is expected due to (1) the thermal insulation of the compression heads are much better than the the grips used in dog-bone samples, (2) the sample size is much smaller and therefore the maximum crosshead speed of the tension–compression module corresponds to a much higher strain rate. The prior is characterized by the τ_{eq} parameter in Equation 3.37, which is measured to be consistently ≈ 2.75 s for both samples.

The energy balance terms for the single-crystal compression tests are presented in Figure 4.7a, b. In addition to the terms from Equation 3.37, the dissipated ($W_d = W_s + W_l - W_{the}$) and plastically stored ($W_b = W_a - W_d$) energy rates are also explicitly plotted. For the $c^{\perp}$ sample, the plastic power required to activate tensile twins is very

low (approximately 1 mW for this geometry). Consequently, it is difficult to precisely quantify the dissipated energy and compute the Taylor–Quinney coefficient for twinning.

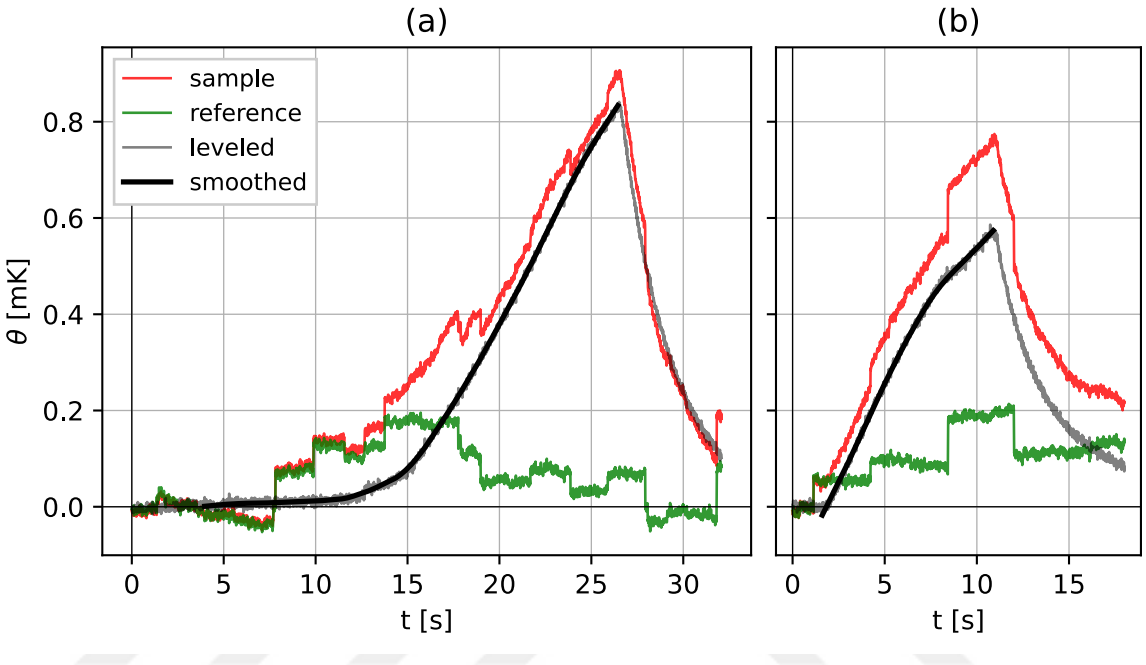


Figure 4.6. Temperature processing of (a) $c^{\perp}$, (b) $c^{\parallel}$ single-crystal compression tests.

The zoomed-in plot in Figure 4.7e reveals that the stored energy W_b exceeds the applied plastic work up to 1% compressive strain, while the dissipated energy occasionally drops below zero—both of which are physical impossibilities. Nevertheless, the trend in this region clearly indicates that nearly all plastic work is stored in the material; hence, β is very close to 0, as seen in Figure 4.7c. The arrow in Figure 4.7c marks a temporary increase in β, which corresponds to the small temperature rise in Figure 4.5c and supports the interpretation that the material is approaching the onset of a slip-dominated deformation regime. Past the twin plateau, the β value for the $c^{\perp}$ sample rises to approximately 0.4. Similarly, Figure 4.7d shows that β for the $c^{\parallel}$ sample steadily approaches approximately 0.5 as deformation progresses. These estimates for β are in close agreement with the values obtained for twin- and slip-dominated deformation in the polycrystalline compression tests (Section 4.1).

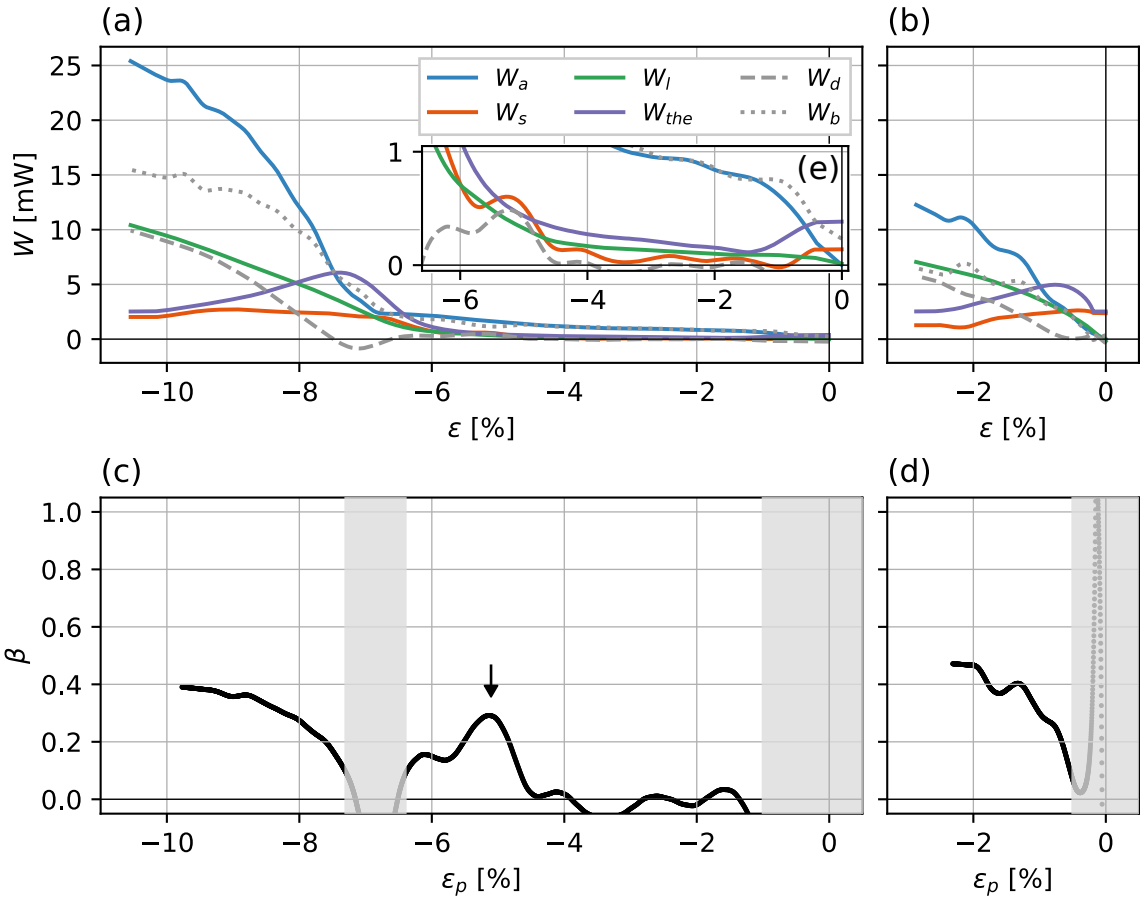


Figure 4.7. Energy balance terms (Eq. 3.37) for single crystal compression tests: (a) $c^{\perp}$ sample, (b) $c^{\parallel}$ sample. Taylor–Quinney coefficients for (c) $c^{\perp}$ sample, (d) $c^{\parallel}$ sample. (e) shows a zoomed-in view of the energy terms during the twin plateau of the $c^{\perp}$ sample.

4.3. Model Validation by Crystal Plasticity Simulations

In this section, the crystal plasticity model is validated against the experimental data. Crystal plasticity simulations are performed individually for the single crystal and polycrystal experiments. Since the single crystal specimens are pure magnesium and the polycrystal specimens are of the AZ31 alloy, a separate set of material parameters must be calibrated for each material to accurately capture their respective thermomechanical responses.

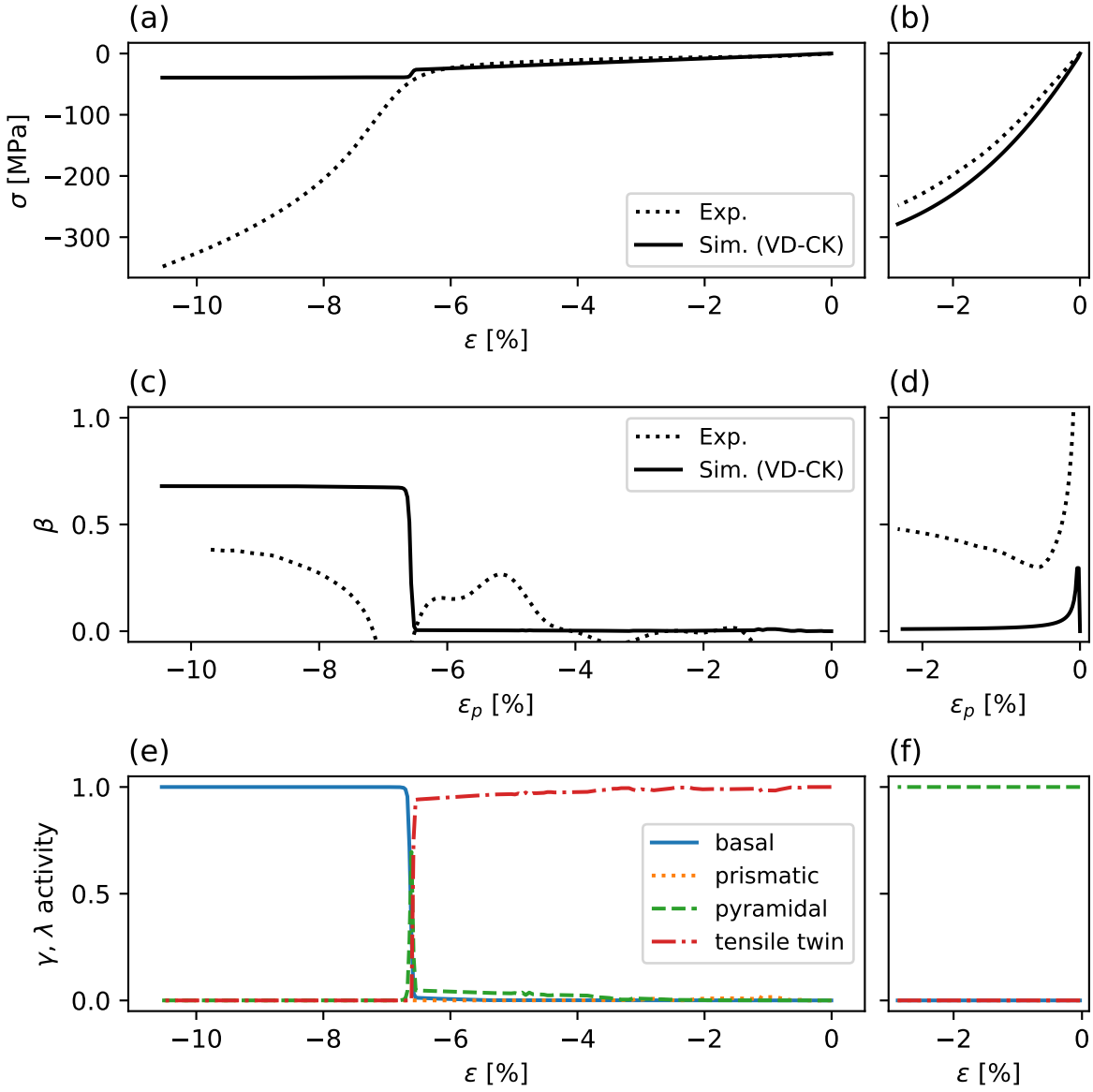


Figure 4.8. Single-crystal simulation results using parameters adapted from Chang and Kochmann [33]. Stress–strain, β, and activity rate plots (a), (c), (e) for $c^{\perp}$; and (b), (d), (f) for $c^{\parallel}$ samples.

4.3.1. Pure Mg Single Crystal Simulations

Initially, the crystal plasticity model was calibrated using only the viscous dissipation (VD) part of the dissipation potential (Equation 3.18), employing parameters from [33]. Results from this simulation (denoted as VD-CK) are shown in Figure 4.8. Uniaxial compression simulations with this parameter set closely approximated the

experimentally obtained stress–strain curve for the $c^{\parallel}$ sample (Figure 4.8b), with the strain accommodated by pyramidal slip as expected (Figure 4.8f). However, as seen in Figure 4.8a for the $c^{\perp}$ sample, the simulation failed to capture the hardening behavior after the twin plateau; the simulated stress was significantly lower than the experimental data in the slip-dominated regime. This discrepancy was attributed to excessive basal slip activity (Figure 4.8e). Furthermore, the simulated β values for $c^{\parallel}$ are significantly lower than what the experimental data suggests (Figure 4.8d), and the simulated β for $c^{\perp}$ after the twin plateau is higher than the experimental data (Figure 4.8c).

The experimental data from [33], which was utilized for calibration in their study, originated from plane-strain single crystal experiments by [29]. The test case within that dataset most analogous to the $c^{\perp}$ sample compression test in this work was a compression test perpendicular to the unconstrained c-axis (labeled case 'e' in [29]). However, that experiment was performed with a constrained basal plane (in the $\langle 1\bar{2}10 \rangle$ direction). This constraint was necessary to isolate individual slip/twin systems; consequently, the parameters calibrated in [33] were not directly suitable for the unconstrained compression experiments conducted in this work.

Table 4.1. Parameter sets used in the single crystal simulations with the VD model.

	Parameters		**VD-CK**	**VD-1**	**VD-2**
Pyramidal	σ_0	(MPa)	0	0	0
	$\sigma_\infty^{\mathrm{PS}}$	(MPa)	150	171	128
	h_α^{PS}	(GPa)	30.0	20.0	15.7
	h_{ij}	(MPa)	25.0	25.0	25.0
	τ_0	(MPa)	1.75	3.50	26.8
	m	—	0.05	0.05	0.05
	$\dot{\gamma}_0$	(s^{-1})	1.0	1.0	1.0
Tensile twin	k_β	(MPa)	1.7	1.7	1.7
	k_{ij}	(GPa)	40	40	40
	τ_0	(MPa)	0	0	0

The parameters were recalibrated using the experimental data from both the $c^{\parallel}$ and $c^{\perp}$ samples. This recalibration was a two-stage process designed to keep the number of parameters manageable. First, the VD model (Equation 3.18) parameters were fitted solely to the stress–strain curves. Second, the Taylor–Quinney coefficient, which governs the partitioning of plastic work into heat, was adjusted to match the remaining experimental data.

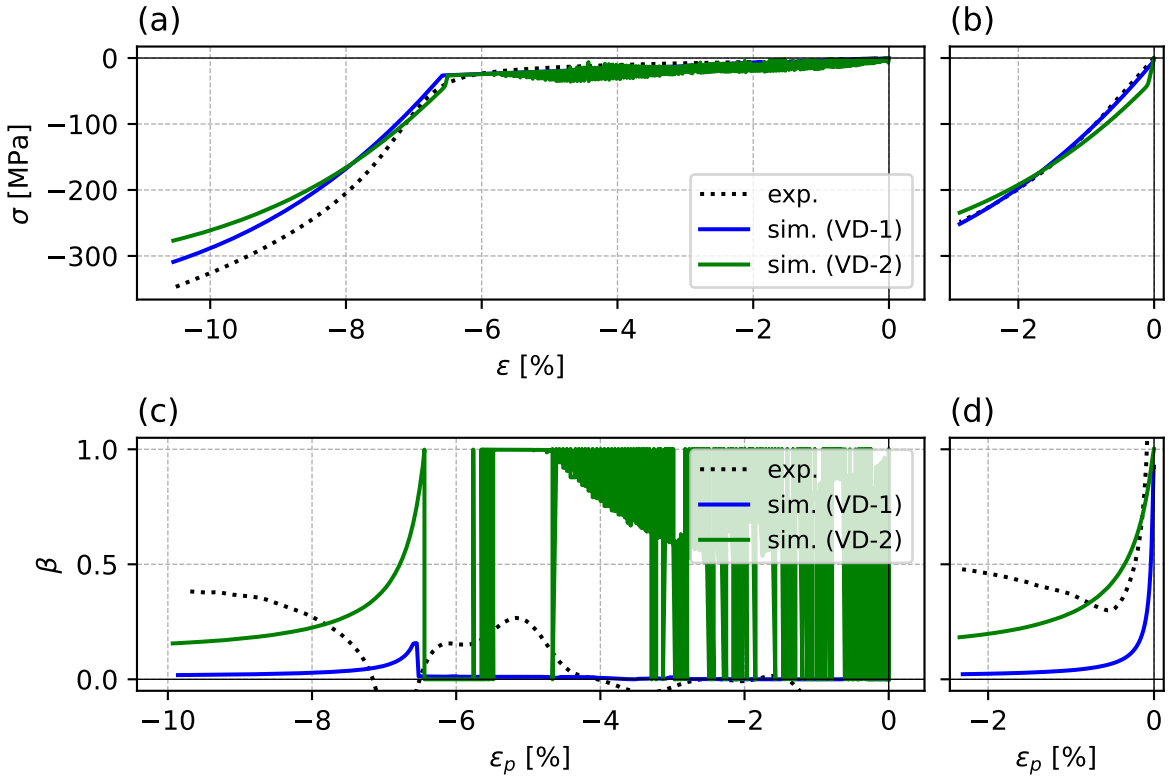


Figure 4.9. Single-crystal simulation results with VD dissipation model using parameters calibrated to stress only (blue); and both stress and β (green). Stress–strain and β plots (a), (c) for $c^{\perp}$ and (b), (d) for $c^{\parallel}$ samples.

The calibrated parameters are given in Table 4.1, along with the values from [33]. In this table, the parameters of only pyramidal slip and tensile twin are given, since there are no data in single crystal experiments detailed in Section 4.2 to calibrate basal and prismatic slip. The only parameter that is changed from VD-CK is the τ_0 of basal slip (from 1.75 MPa to 3.5 MPa), to prevent it from activating with a very low RSS.

The simulation results with the calibrated parameters are shown in Figure 4.9. The stress-only calibration is denoted as VD-1 (blue curves), while the calibration incorporating both stress and the Taylor–Quinney coefficient is denoted as VD-2 (green curves). Although the stress–strain curves for both VD-1 and VD-2 adequately match the experimental results (Figure 4.9a and b), the stress-only calibration (VD-1) yields very low β values (Figure 4.9c and d).

Table 4.2. Refined parameters for single crystal simulations with VD+PD model.

	Parameters		**VD+PD**
Pyramidal	σ_0	(MPa)	0
	$\sigma_\infty^{\mathrm{PS}}$	(MPa)	150
	h_α^{PS}	(MPa)	6,150
	h_{ij}	(MPa)	25.0
	$\sigma_\infty^{\mathrm{PD}}$	(MPa)	290
	h_α^{PD}	(MPa)	6,150
	τ_0	(MPa)	7.2
	m	—	0.05
	$\dot{\gamma}_0$	(s^{-1})	1.0
Tensile twin	k_β	(MPa)	1.7
	k_{ij}	(GPa)	40
	τ_0	(MPa)	0

To match the experimental β values, the VD-2 model required a significant increase in the initial yield strength (τ_0) for pyramidal $\langle c+a \rangle$ slip. This, however, introduced a distinct yield point in the simulated stress–strain curve, visible as a steep initial rise in Figure 4.9b. Even with this adjustment, the simulated β curves did not closely match the experimental data. This simulated yield point was not observed in the experiments (see Figure 4.5b), indicating that a model relying solely on the viscous form of the dissipation potential is insufficient to capture the full thermomechanical response of magnesium single crystals. Furthermore, the increase in τ_0 made the model more unstable, as evidenced by the noise in Figure 4.9c. This instability may stem from

numerical stiffness caused by the power-law form of VD, which was used with a very low rate-dependency exponent, potentially leading to computational challenges (further discussed in Section 5.3.1).

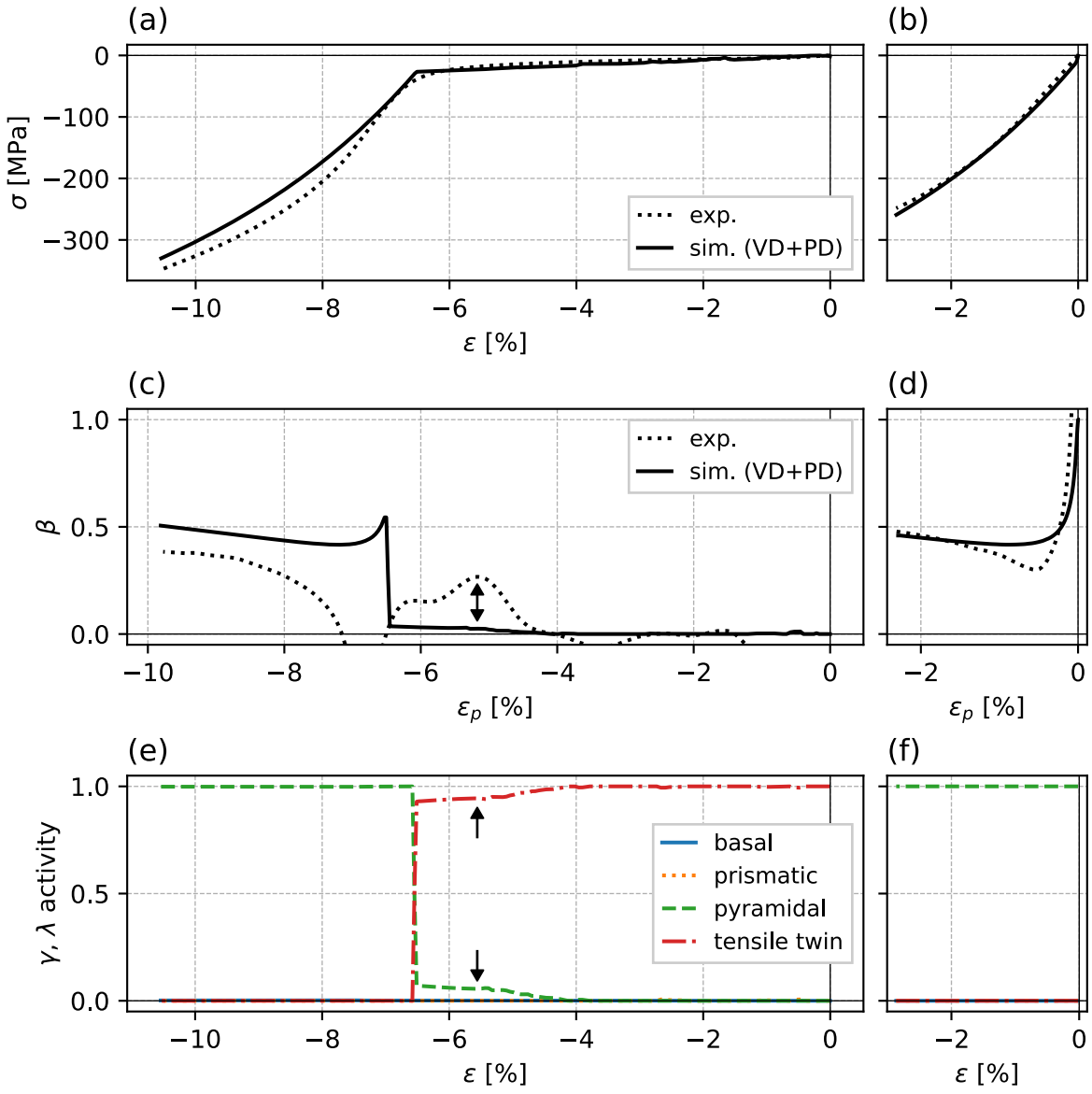


Figure 4.10. Single-crystal simulation results with VD+PD model. Stress–strain, β, and activity rate plots (a), (c), (e) for $c^{\perp}$ and (b), (d), (f) for $c^{\parallel}$ samples. Activity rates are color coded to match the slip/twin system depictions in Figure 1.1.

To address these issues, the extended dissipation potential (Equation 3.19) was introduced, incorporating an additional rate-independent PD term for plastic slip.

This model (denoted as VD+PD) was calibrated by fitting the simulation results to the experimental data of the $c^{\parallel}$ sample, since the slip activity of both samples is expected to mainly consist of pyramidal slip. (For twinning, model parameters from Chang and Kochmann [33] provide a decent fit.) The calibrated parameters for the extended dissipation potential are presented in Table 4.2. Stress, β, and activity rate plots for these crystal plasticity simulations are shown in Figure 4.10. As seen in Figure 4.10b and d, the VD+PD model accurately captures both the mechanical and energetic response of the $c^{\parallel}$ sample without introducing a pronounced, artificial yield point. Figure 4.10f shows that pyramidal slip, being the only system with a positive Schmid factor in this ideal orientation, is the only active slip system as expected.

Stress and β curves for the $c^{\perp}$ sample, as shown in Figure 4.10a and c, also match the experimental data well. Although the simulated β values for the $c^{\perp}$ sample align only loosely with the experimental data, the model captures the twin plateau and subsequent hardening behavior starting at 6.5% strain mark. At this point, the material is fully twinned, as indicated by the volume fraction evolution in Figure 4.11.

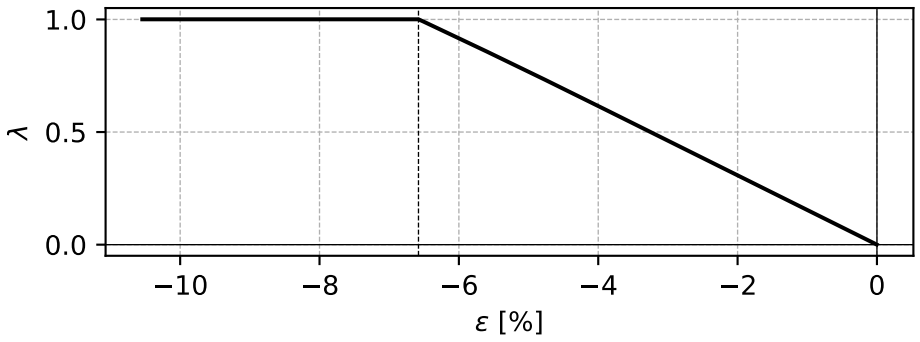


Figure 4.11. Twin volume fraction evolution from $c^{\perp}$ simulation.

Although the magnitude is not perfectly matched, the model captures an early rise in β near the end of the twin plateau, as indicated by the arrow in Figure 4.10c, which is consistent with the experimental data in Figure 4.5c. The same point is also marked in Figure 4.10e, where the activity rate of twinning is shown to drop to approximately 0.93, and correspondingly, the activity rate of pyramidal slip rises to approximately 0.07. In the experiment, this region may potentially include other variants of slip systems,

particularly prismatic slip, which has initially a large RSS (with a Schmid factor of ≈ 0.433) in this orientation. With the rotation of the crystal lattice due to twinning, the Schmid factor for prismatic slip decreases to nearly zero, and therefore slip activity that follows the twin plateau is dominated by pyramidal slip. The failure to capture possible activity of other slip systems in this point may result from the flow rule used in the model (Equation 3.6a), where a single slip rate drives a slip system from both parent and twinned orientations.

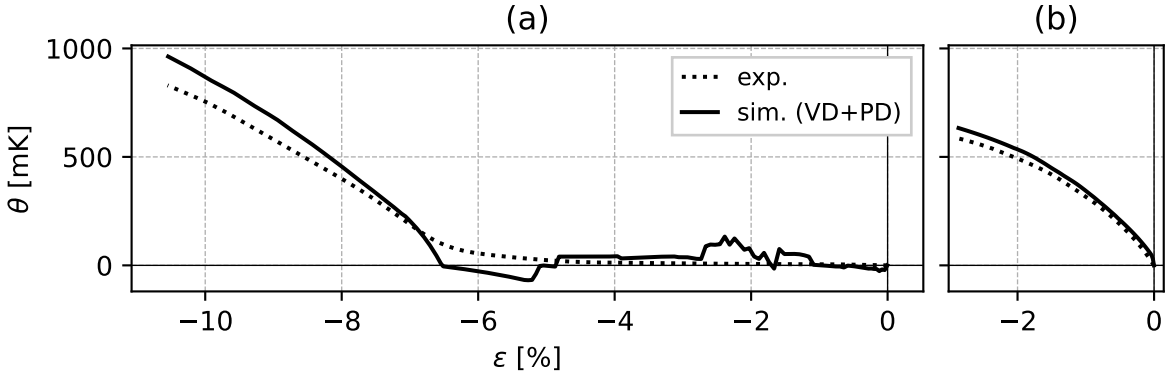


Figure 4.12. Temperature variations from single crystal compression simulations. (a) $c^{\perp}$ sample, (b) $c^{\parallel}$ sample.

Figure 4.12 shows the temperature variation curves for the single crystal compression tests. The VD+PD model closely matches the experimental temperature data, especially for the $c^{\parallel}$ sample (Figure 4.12b), while the $c^{\perp}$ sample (Figure 4.12a) shows a particular mismatch in the transition region between the twin plateau and the slip-dominated regime, specifically where the model predicts a slight temperature decrease. Here, it is important to note that the match in simulated temperature is a *consequence* of parameter calibration to combined stress and β measurements; the model is not explicitly calibrated to match the temperature data.

There are artificial temperature variations around the 2% strain mark in Figure 4.12a. These are due to suboptimal solutions to root-finding problem (see Section 3.2.2.1), meaning that at those time steps, the quasi-static equilibrium is not fully satisfied for the current set of material parameters.

The apparent Poisson's ratio of the observation surface for the single crystal compression tests is shown in Figure 4.13. It is calculated as

$$\nu_{\text{apparent}} = -\frac{\varepsilon_{yy}}{\varepsilon_{xx}}, \tag{4.1}$$

where ε_{xx} is the axial strain and ε_{yy} is the transverse strain.

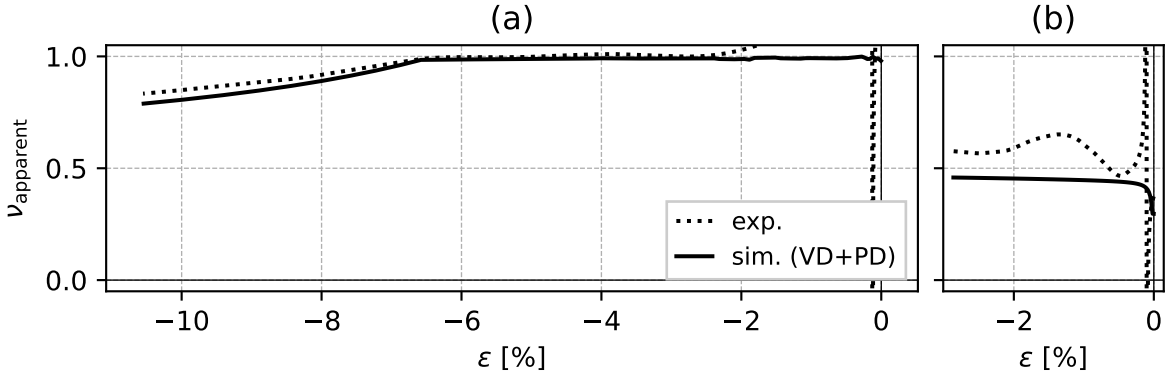


Figure 4.13. Apparent Poisson's ratio from single crystal compression simulations. (a) $c^{\perp}$ sample, (b) $c^{\parallel}$ sample.

For the $c^{\perp}$ sample, the model predicts an apparent Poisson's ratio of exactly 1.0 during the twin plateau, which is consistent with the experimental data. (Although the experimental ν_{apparent} value until 2% compressive strain appears to be larger than 1, that can be attributed to IRT-DIC measurement errors.) Following the transition to slip-dominated deformation, the Poisson's ratio drops to approximately 0.8, which is also in good agreement with the experimental data. For the $c^{\parallel}$ sample, the apparent Poisson's ratio predicted by the model is slightly below 0.5 (Figure 4.13b), while the experimentally measured value is approximately 0.55.

4.3.2. Mg AZ31 Polycrystal Simulation

The model parameters for Mg AZ31 were calibrated against the experimental data from sample A. The calibration process was similar to that for the single crystal case, though the manual calibration was more involved due to nonlinearities in the model's behavior. The process involved three main steps: (1) fitting the twin plateau yield

point by setting initial yield strengths for the slip and twin systems, (2) adjusting β by modifying the ratio of stored to dissipated yield strengths, and (3) scaling the saturation stress of the slip systems to match the hardening behavior in the slip-dominated regime. Once a close match was achieved, the parameters were further refined using the curve-fitting algorithm described in Section 3.4. The final calibrated parameters for the Mg AZ31 polycrystal are presented in Table 4.3.

Table 4.3. Parameter set used in the Mg AZ31 polycrystal simulation.

	PS			**PD**			**VD**		
Basal	σ_0	(MPa)	17.6	—			τ_0	(MPa)	0.0
	σ_∞	(MPa)	12.8	σ_∞	(MPa)	0.0	m	—	0.05
	h_α	(GPa)	186.1	h_α	(MPa)	0.0	$\dot{\gamma}_0$	(s^{-1})	1.0
	h_{ij}	(MPa)	0.5	—			—		
Prismatic	σ_0	(MPa)	0.5	—			τ_0	(MPa)	12.0
	σ_∞	(MPa)	22.3	σ_∞	(MPa)	52.0	m	—	0.05
	h_α	(GPa)	1.4	h_α	(GPa)	8.2	$\dot{\gamma}_0$	(s^{-1})	1.0
	h_{ij}	(MPa)	20.0	—			—		
Pyramidal	σ_0	(MPa)	23.0	—			τ_0	(MPa)	26.5
	σ_∞	(MPa)	60.5	σ_∞	(MPa)	488.5	m	—	0.05
	h_α	(GPa)	8.0	h_α	(GPa)	14.4	$\dot{\gamma}_0$	(s^{-1})	1.0
	h_{ij}	(MPa)	25.0	—			—		
Tensile twin	σ_0	(MPa)	0.8				τ_0	(MPa)	1.5
	k_β	(MPa)	7100	—			m	—	0.05
	k_{ij}	(GPa)	40.0				$\dot{\lambda}_0$	(s^{-1})	1.0

Figure 4.14 presents the simulated stress–strain response, β evolution, and activity rate plots for the Mg AZ31 polycrystal, alongside the experimental results from Section 4.1. As shown in Figure 4.14a, the simulated stress–strain curve reproduces the characteristic sigmoidal shape of rolled magnesium during compression–tension loading. The significant twin activity predicted during compression and subsequent load reversal (up to zero strain), shown in Figures 4.14d and e, confirms that the twinning–detwinning

model detailed in Section 3.2.1.2 is functioning as expected. The activity rate plot corresponding to reversed loading in Figure 4.14e indicates that the model correctly predicts the transition from detwinning to slip plasticity during tension, with only trace amounts of detwinning observed.

The simulated stress–strain curve shows an overall good fit compared to the experimental data, with the exception of the twin plateau. Here, the simulation predicts an early yield at 40 MPa and a more gradual hardening towards 100 MPa at 2% strain, instead of the sharp yield point at 80 MPa and nearly perfectly plastic behavior observed in the experiment. This discrepancy is likely due to the assumption of uniform deformation in all grains imposed by Taylor-type polycrystal averaging scheme. This constraint forces some grains to harden more and others less than they would in reality, preventing the model from reproducing a perfectly plastic response. The effect of Taylor averaging on hardening will be discussed in more detail in Section 5.3.4.

The activity rate plots in Figure 4.14d and e provide insight into the evolution of slip mechanisms during cyclic loading. Basal slip is observed to be active in both compression and tension, consistent with its low CRSS and ease of activation in magnesium alloys.

It is important to note that the average grain orientation in rolled Mg AZ31 closely resembles the ideal orientation of the $c^{\perp}$ single crystal sample (see Figure 4.4a in Section 4.2). As a result, during compression, tensile twinning is strongly favored in both the polycrystal and single crystal cases. This similarity also explains the suppression of prismatic slip during compression, as twinning reorients many grains, making prismatic slip becomes less favorable, analogous to the behavior in the $c^{\perp}$ single crystal simulation (Section 4.3.1). Upon load reversal and detwinning, grains are reoriented back to their initial orientation, which restores the favorability of prismatic slip during tension. This is reflected in the increased prismatic slip activity shown in Figure 4.14e, highlighting the strong influence of crystallographic texture on the activation of deformation mechanisms in magnesium alloys.

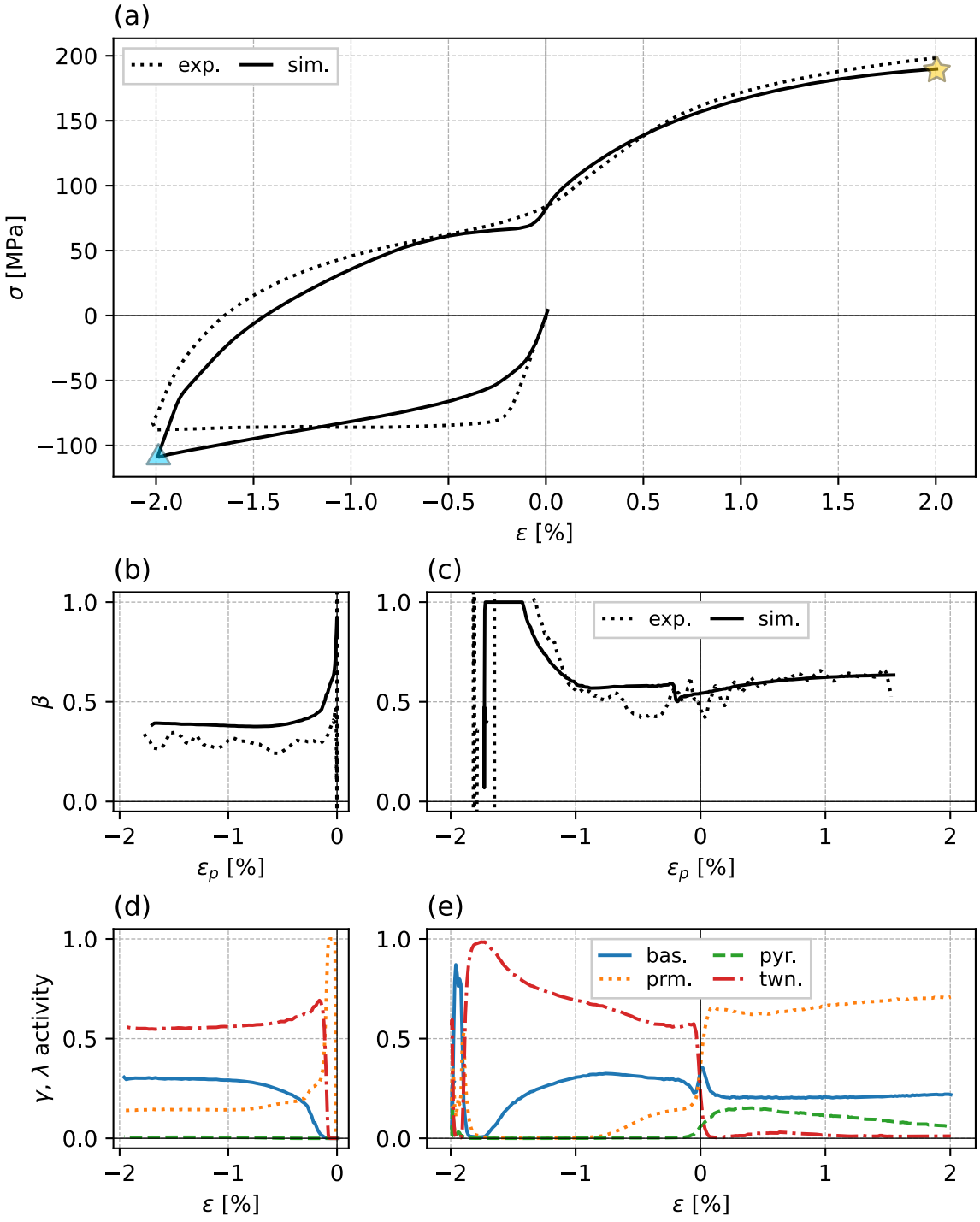


Figure 4.14. Polycrystal simulation results for Mg AZ31 sample A. (a) Stress–strain; (b) and (c) are β evolution, (d) and (e) are activity rates for compression (A0) and tension (A1) load segments. Activity rates are color coded to match the slip/twin system depictions in Figure 1.1.

The model also faithfully captures the overall dissipative behavior of AZ31. The β evolution curves in Figure 4.14b show a predicted nominal β value of 0.4 for twin-dominated deformation during compression, which closely matches the experimental value of 0.3. Similarly, the nominal β values of 0.5 for detwinning and 0.6 for slip-dominated deformation, shown in Figure 4.14c, agree well with the experimentally measured values.

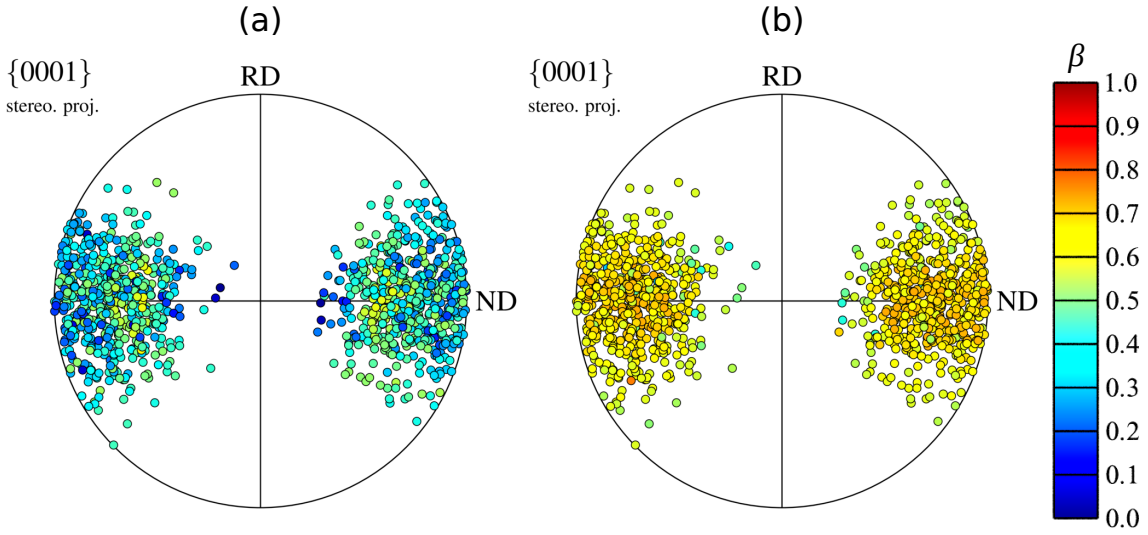


Figure 4.15. Per-grain β values at the end of (a) compression ramp; (b) tension ramp, shown on the pole figure of the Mg AZ31 polycrystal simulation.

Figure 4.15 displays pole figures of the polycrystal, with each grain orientation color-coded according to its β value, thereby providing a detailed view of the polycrystal's grain-level dissipative characteristics. Figure 4.15a, corresponding to the end of the compression ramp (blue triangle in Figure 4.14a), reveals that grains oriented close to the ideal rolling orientation (i.e., c-axis aligned with the normal direction, ND) and those with the largest misorientation angle (oriented closer to the transverse direction, TD) exhibit the lowest dissipation. The low β values in grains near the ideal rolling orientation are expected, as these grains undergo deformation primarily through twinning, which is experimentally found to be a low-dissipation process (Section 4.1). The low β values in grains with large misorientation angles can be attributed to the predominant activity of basal slip, which, according to the fitted parameters, functions

primarily as a plastic storage mechanism with minimal dissipation. Conversely, grains oriented at approximately 45°to the rolling direction (RD) exhibit the highest β values, indicating that these grains undergo deformation primarily through prismatic slip (see Figure 4.14d), which represents a more dissipative deformation process.

Figure 4.15b shows per-grain β values at the end of the tension ramp (yellow star in Figure 4.14a), where deformation occurs primarily through slip plasticity. The β values are consistently high (matching the nominal 0.6 value, see Figure 4.14c) compared to those at the end of compression, with the notable exception of the most misoriented grains (those oriented closest to TD, with β values around 0.4). This behavior is consistent with experimental observations, where slip-dominated deformation exhibits higher dissipation than twin-dominated deformation.

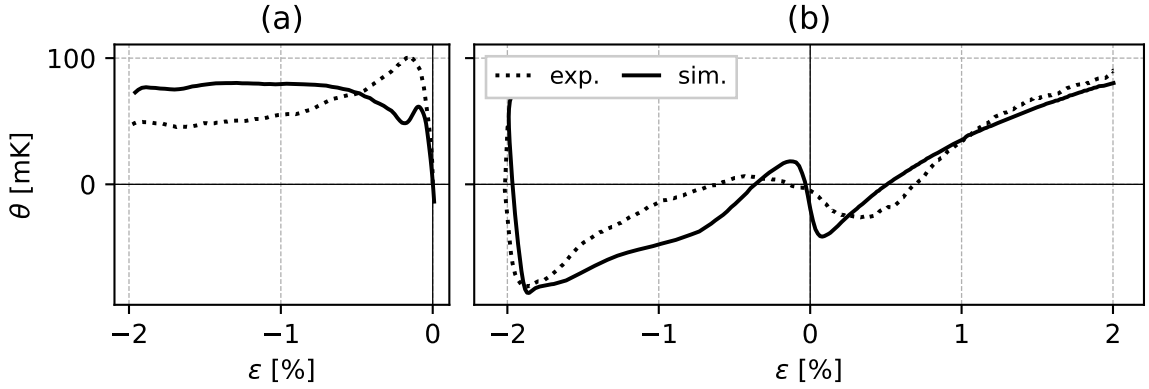


Figure 4.16. Temperature variation curves of Mg AZ31 polycrystal simulation for (a) compression (A0) and (b) tension (A1) load segments.

Another important result is the temperature variation shown in Figure 4.16. Figure 4.16a shows limited agreement with the experimental data during compression, exhibiting a steady-state temperature rise of 100 mK above the reference value instead of the experimentally observed 50 mK. This discrepancy likely results from the combined effects of mismatches in both σ and β. In contrast, the temperature variation during tension (Figure 4.16b) corresponds closely to the experimental measurements. The model captures a temperature drop due to thermoelasticity that occurs not only at the

start of load reversal but also during the transition from detwinning to slip plasticity. This observation supports the hypothesis that deformation is accommodated partially by elasticity once the twin systems are exhausted and until the stress rises to levels sufficient to activate slip systems.

Again, to reiterate, the match between simulated and experimental temperatures is not a result of an explicit calibration attempt to fit temperature data. Rather, it is an outcome of the model's thermomechanical consistency and the calibration process that incorporates mechanical and dissipative data.

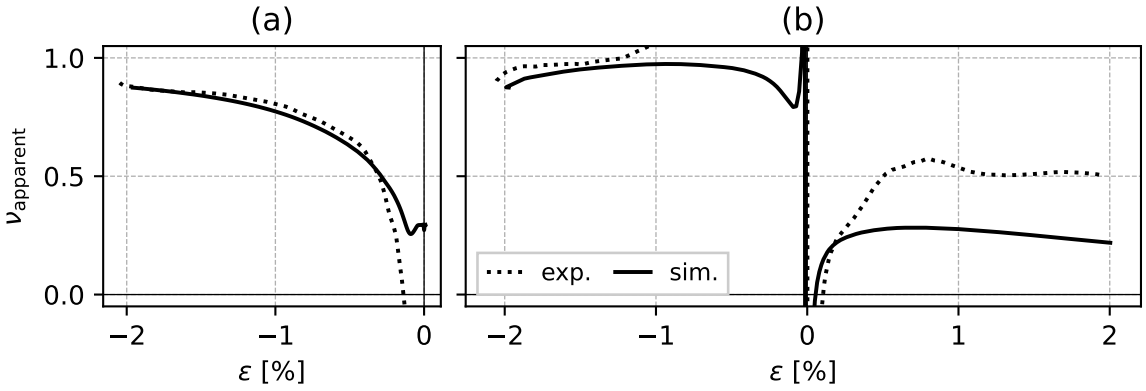


Figure 4.17. Apparent Poisson's ratio for Mg AZ31 polycrystal simulation for (a) compression (A0) and (b) tension (A1) load segments.

The apparent Poisson's ratio (ν_{apparent}) for the Mg AZ31 polycrystal simulation is presented in Figure 4.17, overlaid on the experimentally measured values. The experimental values are calculated from live-DIC experiment strain field averages, which were used to calibrate target crosshead positions (see Section 3.3.3.1). In compression, ν_{apparent} starts from the elastic value of 0.29, then gradually rises towards 1 (Figure 4.17a), and remains at that value during the detwinning that follows load reversal. These values are consistent with the experimental data, with the exception of values near zero strain where the Poisson's ratio is not well defined due to the low magnitude of strain and the low signal-to-noise ratio of DIC measurements. A ν_{apparent} of 1 during twinning/detwinning indicates the 2D nature of the deformation, which is extensively

documented in the literature [9, 10, 58, 59, 132].

When the material transitions into tension and switches to slip-dominated deformation, the apparent Poisson's ratio attains a value of approximately 0.3 for the simulation, whereas the experimental data shows a higher value of approximately 0.5 (Figure 4.17b). The simulated value appears to be close to the elastic Poisson's ratio of 0.29, however, (although not explicitly shown here) the apparent Poisson's ratio about the other axis (i.e., $-\frac{\varepsilon_{zz}}{\varepsilon_{xx}}$) is about 0.7. This means that the deformation is nearly isochoric and thus mostly plastic as expected.

During tension, the strain in rolled Mg AZ31 is primarily accommodated by macroscopic shear bands that follow the dynamically recrystallized off-texture grains [60]. This behavior is challenging to capture in the current model without knowledge of the local microtexture and grain structure.

5. DISCUSSION

5.1. Merits, Dependencies, and Features of the Experimental Data

Given that measured temperatures in this study are small (on the order of 10–100 mK), Figure 5.1 presents additional validation of experimental repeatability using two new polycrystalline samples (C and D) during the compressive loading stage. Sample C is compressed to the same average strain (2%) as samples A and B, while sample D is further loaded (to 2.6%) over the twin plateau. The overall consistency among all the samples is evident.

The plot uses time as the x-axis rather than strain because strain remains constant once loading is complete, and plotting temperature against strain after this point would show temperature decay over a vertical line. This temporal presentation provides clear evidence that measured temperatures reflect genuine physical phenomena. Specifically, temperatures show consistent decay once the physical stimulus (loading) ends (final points marked by dashed circles). Both the temperature decay and initial rise due to the thermoelastic effect remain consistent, even at relatively small measurement values (< 20 mK). The temperature rise during the initial thermoelastic phase shows close agreement among all samples, suggesting precision on the order of a few mK. This precision benefits from field-averaging the temperature data over 24,000 pixels (240×100) in the gage section (Figure 3.3a). This averaging improves measurement precision by reducing uncertainty, though at the expense of spatial resolution [133].

Temperature variation over the twin plateau is somewhat more pronounced. If the agreement during the elastic range indicates measurement precision, then twin-plateau variation must have a physical basis. This leads to the second topical contribution of Figure 5.1, which provides strain maps at the final loading point (computed using pre- and post-loading images from the macro-DIC line, Figure 3.1a). These maps show expected stochastic differences for a material that deforms through the initiation and

propagation of Lüders-like bands. In this case, the banded deformation is due to coordinated twinning, which forms abruptly in very sharp structures for this crystallographic texture. This has been previously studied in volumetric [10] and (using the microscopic line in Figure 3.1c) microscopic [59, 132] detail, with this setup.

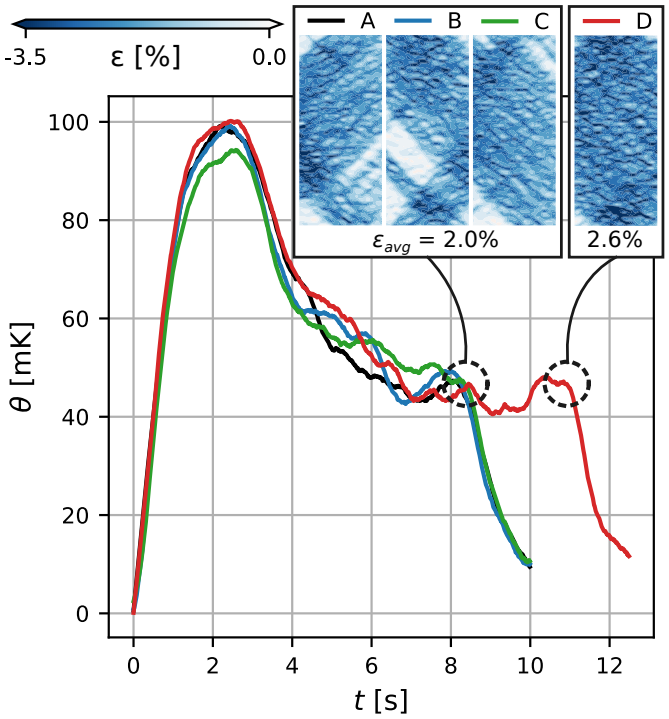


Figure 5.1. A multi-sample comparison of thermal data over the initial twin plateau for four samples A–D, coupled with the DIC-determined strain patterns at the end point of the experiments. A, B (previously considered) and C are loaded up to 2% average compressive strain whereas D is loaded up to 2.6%.

While band locations vary between samples, their strain content (namely, Lüders strain) is characteristic, provided to be around 2-2.5% by [53,58,59]. The $\mp$2% straining range chosen in the polycrystal experiment thus corresponds to an approximate filling of the gage section with twin-based deformation (the same strain range similarly implemented in previous studies [10, 59]). Variations in exact strain accommodation (in terms of location, timing, etc.) among samples A–D can therefore account for the larger spread of temperatures over the twin plateau compared to the elastic region, where deformation is more consistent among samples.

These observations serve two purposes. First, they corroborate the authenticity of the data. Second, while temperature variation over the twin plateau is more noticeable, it remains within a relatively narrow <10 mK corridor. Therefore, the twinning-plateau data can also be considered largely representative of the general nature of deformation, showing only limited sample dependence. Second, sample D, which is strained slightly above the characteristic Lüders strain of the bands, remains on the twin plateau at its final point (its stress is still at the same 85 MPa level, as shown in Figure 4.1a for samples A and B). In fact, for this texture, twinning remains the dominant mechanism with little hardening up to approximately 4% compressive strain [8, 118]. Beyond this point, twinning becomes largely exhausted, culminating in another transition to hard slip. Although that transition is outside this experiment range, the analogous heavy stress increase in that case suggests a sizable secondary thermoelastic effect as well.

5.2. The Importance of Energetic Characterization of Twinning

The deformation twinning mechanism in HCP metals like magnesium is a critical factor governing their anisotropic mechanical behavior. While crystallographic reorientation and strain accommodation have been extensively studied, the energetic characterization of twinning offers a powerful, yet often overlooked, avenue for deepening the understanding of this complex deformation mode. By quantifying the partitioning of plastic work into stored energy and dissipated heat, unique insights are gained into the underlying micromechanisms active during twinning.

Deformation twinning in HCP crystals occurs through highly localized simple shear of the crystal lattice across a twin plane. This shear transforms a portion of the crystal into a twin—a region with the same crystal structure but with a mirror-image orientation relationship to the parent matrix. Unlike dislocation-mediated plastic deformation, which involves the creation and movement of numerous dislocations and associated elastic strain fields, an idealized deformation twin forms with coherent twin boundaries. These boundaries are atomically sharp, low-energy interfaces with highly ordered atomic arrangements and minimal long-range elastic strain fields. Consequently,

an idealized twin is often considered completely dissipative, with no energy storage within the lattice, leading to a Taylor–Quinney coefficient (β) of 1.

However, the experimental findings presented in this thesis, particularly from the single-crystal compression tests, reveal a significant discrepancy with this idealized view. During the twin plateau of the $c^{\perp}$ sample, the measured Taylor–Quinney coefficient was found to be remarkably low, approaching zero (supported by similarly low β values for twin-dominated deformation in polycrystalline experiment). This suggests that nearly all plastic work expended during tensile twinning in magnesium is stored within the material rather than dissipated as heat. This stored energy primarily contributes to new twin boundary formation, lattice reorientation, and potentially dislocation generation associated with twin growth. This low β value provides critical evidence challenging simplistic views of plastic work partitioning and highlights the unique energetic signature of twinning.

Experimental evidence suggests that energy dissipation during twinning may not arise from the twin transformation itself but from secondary slip activity near twin boundaries. As twins nucleate and propagate, they introduce sharp discontinuities in the crystal lattice. To maintain compatibility between twinned and untwinned regions, localized slip activity initiates at or near twin boundaries. This slip, driven by stress concentrations and lattice distortions, forms geometrically necessary dislocations (GNDs) that contribute to heat generation through dissipation [106]. Therefore, the low β value observed in twin-dominated deformation could indicate that twinning is highly energy-storing, while the associated compatibility-driven slip represents the main source of the limited heat dissipation observed.

However, interpreting these results requires careful consideration of both the nuances of magnesium's twinning process and the thermal data collection procedures. Tensile twinning in magnesium activates readily, requiring exceptionally low CRSS compared to many slip systems. Consequently, the total plastic work for twin-mediated deformation is inherently low (see the W_a curve in Figure 4.7a). This low plastic work

magnitude makes accurate measurement and attribution of dissipated heat challenging, as signal-to-noise ratios in thermal measurements become limiting factors at these energy levels.

Beyond the experimental challenge of low signal-to-noise ratios, the interpretation of the Taylor–Quinney coefficient hinges critically on the assumption of uniform deformation within the measurement volume [134]. The process of twinning in magnesium often violates this assumption, as it can proceed through the formation and propagation of stochastic, localized "Lüders-like" bands. This inherent deformation non-uniformity creates a larger spread in temperature data during twinning compared to the more uniform elastic deformation regime (Figure 5.1). When localization becomes more severe, such as in the formation of shear bands, this issue is further exacerbated.

Research on other HCP metals has demonstrated that "apparent energy storage" ($\beta < 1$) can be a direct artifact of such non-uniform deformation, rather than a true microstructural energy storage phenomenon. In a study on zirconium, a sample that developed a shear band yielded a misleadingly low β value because the bulk temperature measurement averaged the intense, localized heat within the band with the cooler, surrounding material, thus underestimating the total heat dissipated [135]. Direct measurements from Kolsky bar tests in hafnium have quantified this effect, showing a temperature rise of 830 K within a shear band compared to only 590 K in a uniformly deforming region [136]. These findings underscore that a low measured β value must be interpreted with caution, as it may reflect a violation of the uniform deformation assumption rather than genuine energy storage, necessitating concurrent microstructural analysis to validate the interpretation.

5.3. Reflections on the Magnesium Crystal Plasticity Model

The crystal plasticity model developed in this thesis represents a substantial advancement toward thermodynamically consistent simulation of magnesium alloys with integrated thermal-mechanical coupling. By building upon a variational framework and

validating against an experimental dataset that uniquely combines mechanical testing with in-situ thermal measurements, the model successfully captures essential aspects of magnesium's deformation behavior. However, this evaluation reveals both the strengths of the variational approach and limitations that provide specific directions for future model refinement.

5.3.1. Thermomechanical Consistency through Variational Framework

A primary advantage of the model derives from its formulation within a variational framework. This approach applies to a broad class of materials exhibiting elastic-inelastic behavior where hardening can be described by internal state variables [36, 66]. This generality makes the framework especially well-suited for addressing the specific challenges posed by magnesium, providing fundamental advantages beyond computational convenience.

The framework offers two key benefits for magnesium alloy modeling. First, it guarantees thermodynamic consistency when the constitutive relations for hardening and rate dependency are defined as derivatives of thermodynamic potentials (i.e., the free energy and the dissipation pseudo-potential). This formulation ensures that the model respects the laws of thermodynamics by construction—a crucial feature for any model aiming to capture thermomechanical coupling. Importantly, this approach enables calculation of the history-dependent Taylor–Quinney coefficient as predicted by the model, without any prior assumptions [37, 39]. Since the evolution of β under deformation has been experimentally quantified in this work, this predictive capability allows for direct and rigorous validation of the model's thermomechanical response, extending validation beyond purely mechanical comparisons.

Second, the variational formulation provides an implicit viscoplastic update scheme that offers significant numerical advantages for magnesium alloys. Traditional explicit rate dependency models require a constitutive relation to be defined on increments, whereas the variational approach determines the updated state through incremental

energy minimization. This distinction is highly advantageous for viscoplastic models of materials like magnesium alloys that exhibit low strain-rate dependency.

Rate dependency models with power-law formulations can encounter numerical difficulties during the minimization process required to update internal variables. For magnesium, the characteristically low rate dependency exponent leads to nearly infinite hardening rates at very low strain rates, creating substantial numerical stability challenges. The variational framework, by allowing rate-independent dissipation potential formulations, enables efficient modeling of low-rate dependency materials through an implicit update procedure while maintaining rate dependency for consistency with established literature.

5.3.2. Adaptations and Future Directions for Dissipation Modeling

A key finding during model development was the insufficiency of a purely rate-dependent (VD) power-law dissipation potential to capture the observed energetic characteristics of magnesium, which is simply addressed by the inclusion of rate-independent (PD) terms in the dissipation potential. This pragmatic phenomenological solution was effective in reproducing the morphology of hardening and the measured evolution of β without compromising numerical stability, but it highlights the need for more sophisticated dissipation modeling within a unified structure. A more general approach to modeling the kinematics of plastic slip can be therefore achieved by extending the dissipation function given in Equation 3.18 with the following formulation [38]:

$$\phi^*_{\text{sl}}(\dot{\boldsymbol{\gamma}};\ \boldsymbol{\gamma}, T) = \sum_{\alpha=1}^{n_{\text{sl}}} \frac{\tau_0^{(\alpha)}(\boldsymbol{\gamma}, T)\dot{\gamma}_0^{(\alpha)}}{m+1} \left(\frac{\dot{\gamma}^{(\alpha)}}{\dot{\gamma}_0^{(\alpha)}} \right)^{m+1}, \tag{5.1}$$

where, constant $\tau_0^{(\alpha)}$ is replaced by the generic expression of $\tau_0^{(\alpha)}(\boldsymbol{\gamma}, T)$ for the reference stress. This term can be used to embed complex phenomena, including intricate hardening models (e.g., latent hardening) and more complex, physically-based theories of rate-dependency, such as Arrhenius-type thermal activation models [35, 71, 137]. A more relevant use case for magnesium alloys would be to link the reference stress of

twin systems to the accumulated slip strain, which would effectively simulate effects of dislocation activity on twin nucleation and growth [138–141].

5.3.3. Limitations in Modeling Latent Hardening Effects

Perhaps the most significant overlook of the current model is its simplified treatment of latent hardening. The model assumes that only deformation systems from the same family (e.g., basal–basal or twin–twin) interact with each other, and does so through a simple linear latent hardening law. This simplification prevents the model from capturing the full spectrum of thermomechanical responses observed in experiments, as it neglects the complex interactions between different families of systems. In many crystals, it is found that activity in one slip system hardens other systems more than it hardens itself, a phenomenon to which many intricacies in single-crystal behavior can be traced.

A more comprehensive approach can account for this interplay, for instance, through a plastic work potential in the form of $W_p(\Gamma)$, where hardening is governed by an effective slip strain, Γ, defined as

$$\Gamma = \left(\sum_{\alpha=1}^{n_{\text{sys}}} \sum_{\beta=1}^{n_{\text{sys}}} \mathcal{A} \gamma^{(\alpha)} \gamma^{(\beta)} \right)^{1/2} . \tag{5.2}$$

Here, the matrix of interaction coefficients, $\mathcal{A}$, explicitly models the hardening of system (α) due to activity on system (β). The ratio of the off-diagonal to diagonal components of $\mathcal{A}$ constitutes the *latent hardening ratio*, which quantifies the strength of these interactions [36].

However, implementing such a sophisticated formulation introduces a formidable practical challenge. For a material like magnesium with multiple slip and twin system families, this matrix becomes large, introducing a substantial number of material parameters that must be determined. This task is exceptionally difficult, as it is nearly impossible to design experiments that can cleanly isolate and measure the hardening interaction between two specific, different deformation mechanisms.

5.3.4. Implications of Taylor Approximation in Polycrystal Simulations

Taylor averaging in crystal plasticity, assumes that all individual grains within the polycrystalline aggregate experience the same macroscopic strain as the entire material (also called a Voigt model). This is like imagining all grains are perfectly bonded and deform together without any relative displacement at their boundaries. Because each grain has a different crystallographic orientation and thus different elastic and plastic anisotropy, maintaining a uniform strain across all grains requires different stress states in each grain. In other words, some grains will be stressed more than others to achieve the imposed deformation. The varying stress states at grain boundaries mean that static equilibrium (forces balancing at interfaces) is generally violated in this model. Since every grain is forced to deform by the same amount, even "soft" grains (those unfavorably oriented for easy slip) are strained, leading to a higher overall resistance to deformation. This results in the *stiffest possible response* for the aggregate, making the Taylor average an upper bound for the material's elastic moduli and yield strength. A useful analogy would be a chain of different springs connected in parallel. If one pulls the ends of the chain, all springs stretch by the same amount (uniform strain). The total force (stress) required is the sum of the forces from each spring, and the stiffer springs contribute more to the overall resistance.

In contrast, a uniform stress model (also called a Reuss model) assumes all individual grains within the polycrystalline aggregate experience the same macroscopic stress as the entire material. This implies that the material deforms in a way that minimizes the stress in each grain. To maintain a uniform stress, grains with different orientations will deform by different amounts. Grains that are "soft" will deform more easily and extensively than "hard" grains. The differing strain states between grains lead to incompatibility at grain boundaries. Since deformation preferentially occurs in the weakest paths (grains that can deform most easily under the applied stress), the overall resistance to deformation is minimized. This makes the Reuss average a lower bound for the material's effective elastic moduli and yield strength. The corresponding rheological analogy would be a chain of springs connected in series. If one wishes

to apply a force (stress) to the chain, that same force acts on every spring (uniform stress). However, each spring will stretch by a different amount, with the softer springs extending more. The total deformation (strain) is the sum of the individual stretches.

In practice, the deformation of polycrystalline materials lies between these two limiting bounds. Grains are indeed connected and must maintain compatibility across interfaces, but they also experience heterogeneous local stress and strain fields due to differences in crystallographic orientation, elastic properties, and slip system activity. Consequently, the actual mechanical behavior of polycrystalline materials, whether elastic or plastic, typically falls between the Voigt upper bound and the Reuss lower bound. More sophisticated modeling approaches, such as crystal plasticity finite element (CPFE) simulations, are designed to bridge the gap between these extreme assumptions by accounting for the complex elastic and plastic interactions between neighboring grains more realistically. These models capture both strain and stress localizations simultaneously, providing a more accurate representation of the heterogeneous deformation processes that govern polycrystalline material behavior.

Returning back to the polycrystal simulation of rolled Mg AZ31 in Section 4.3.2, the notable discrepancy between the experimental and simulated stress–strain curves during the twin plateau can be safely attributed to the artificial strain compatibility requirements of the Taylor approximation. Since all grains are assumed to experience the same macroscopic strain, regardless of their crystallographic orientation, when twinning is activated in favorably oriented grains, the imposed uniform strain necessitates that misoriented grains also accommodate an equivalent amount of deformation. (More precisely, favorably oriented and misoriented grains reach a middle ground in terms of deformation.) However, these misoriented grains may not be able to deform by twinning and must instead harden through alternative mechanisms. This ultimately leads to a stiffer aggregate response in the simulation compared to the actual material, where strain can localize by heterogeneous twin bands [9, 10, 58, 59, 132]. As a result, the simulated stress–strain curve during the twin plateau is unable to fit the perfectly plastic behavior seen in experiments.

To fit the overall mechanical response, the least-squares optimization algorithm used for parameter calibration compensates for this limitation by adjusting material parameters, which can result in overfitting. This is further evidenced by the initial yield stresses of basal slip being higher than, for example, those of prismatic slip (see σ_0 and τ_0 values for both in Table 4.3). Even though the basal slip is the most easily activated slip system in magnesium, the Taylor approximation forces the model to assign an unrealistically high CRSS to accommodate the nearly perfectly plastic behavior of the twin plateau.

6. CONCLUSION

This doctoral research was motivated by a persistent challenge in materials science: the accurate prediction of the complex, anisotropic, and often counter-intuitive mechanical behavior of magnesium alloys. Their promising strength-to-weight ratio is frequently offset by deformation characteristics dominated by mechanical twinning, a phenomenon that traditional plasticity models struggle to capture with high fidelity, particularly concerning its thermomechanical consequences. The central aim of this thesis was therefore to develop and validate a high-fidelity, multi-physics crystal plasticity model capable of describing not only the mechanical response but also the concurrent energy dissipation and storage in magnesium during plastic deformation. This was achieved by pioneering a dual approach that integrated novel, multi-modal experimental measurements with a thermodynamically consistent variational modeling framework.

The experimental findings revealed unique and consistent energetic signatures for the primary deformation mechanisms, with nuanced differences between the single-crystal and polycrystalline samples. In pure single-crystal magnesium, tensile twinning appeared to be an almost purely energy-storing process ($\beta \approx 0$), while in polycrystalline AZ31, twin-dominated deformation remained a low-dissipation process ($\beta \approx 0.3$). Conversely, dislocation-mediated deformation was substantially more dissipative in both materials. For pyramidal slip in the single crystal, β approached 0.5, and for the slip-dominated regime in the polycrystal, β reached approximately 0.6. The reversed loading tests on polycrystalline AZ31 also provided the first energetic characterization of detwinning, which exhibited an intermediate dissipation level ($\beta \approx 0.5$). Critically, these polycrystal tests captured a distinct secondary thermoelastic cooling effect during the transition from detwinning to slip plasticity, providing clear evidence of a deformation regime governed by elastic stretch before the activation of harder slip systems.

Building on this experimental foundation, a crystal plasticity model was developed within a variational viscoplasticity framework. This approach inherently ensures ther-

modynamic consistency, enabling prediction of the Taylor–Quinney coefficient for direct comparison with experimental data. The model incorporated a pseudo-slip formulation to account for twinning, detwinning, and retwinning processes. A critical advancement was the enhancement of the model's dissipation potential to include both rate-dependent (viscous) and rate-independent (plastic) dissipation terms. This modification proved essential for simultaneously capturing the experimentally observed stress-strain curves and the evolution of β without introducing numerical artifacts.

The validated model successfully reproduced three key aspects of magnesium's mechanical behavior: the characteristic sigmoidal stress-strain response, the evolution of slip and twin system activity, and the subtle thermal signatures observed under complex, non-monotonic loading conditions. This comprehensive validation demonstrates the model's capability to predict both mechanical and energetic responses, providing a powerful tool for understanding and designing magnesium alloy applications where accurate prediction of deformation behavior is critical.

6.1. Contributions to the Field

This research involved comprehensive experimental characterization that yielded a quasi-static thermomechanical dataset for magnesium and its light alloys under various loading conditions, including reversed loading. Fundamentally, the research provided crucial insight into dissipation mechanisms, confirming that deformation mechanisms in magnesium possess distinct energetic fingerprints. By quantifying the Taylor–Quinney coefficient for twinning, detwinning, and slip, this work establishes a physically-based benchmark for validating the energetic consistency of constitutive models. This approach provides an independent verification channel that can detect model deficiencies not apparent in mechanical data alone, offering the materials community a more rigorous validation protocol for constitutive model development. The development of a thermodynamically consistent crystal plasticity model validated against both mechanical and thermal data represents a significant step beyond traditional approaches, leading to a more physically grounded and predictive framework. For example, this

combined validation effort demonstrated that a simple power-law potential is insufficient to simultaneously capture the thermomechanical behavior of magnesium. The necessity of a combined rate-dependent and rate-independent dissipation potential offers a new phenomenological understanding of how energy is partitioned during plastic deformation.

6.2. Limitations of the Study

Despite these contributions, an honest assessment reveals several limitations that offer clear directions for refinement. A primary limitation stems from the use of a Taylor-type homogenization scheme in the polycrystal simulations. By enforcing uniform strain across all grains, the model could not fully capture the significant strain localization and heterogeneous deformation inherent to twinning, leading to a stiffer-than-observed response on the twin plateau. This was compounded by simplified constitutive relationships, including the treatment of latent hardening and the pseudo-slip representation of twinning, which is an abstraction of the complex morphology of discrete twin lamellae. On the experimental side, challenges arose from the extremely low plastic work associated with twinning, which complicates measuring the weak thermal signal. Additionally, the reliance on a zero-dimensional heat equation for energetic analysis assumes uniform deformation, an idealization that is tested by the formation of stochastic, Lüders-like twin bands.

6.3. Future Work

The findings and limitations of this thesis motivate several promising avenues for future research. The most immediate step involves advancing the modeling framework by implementing the developed constitutive model within a full-field simulation environment, such as CPFE models. This approach would overcome the limitations of Taylor averaging by explicitly resolving grain interactions and strain localization. Concurrently, the constitutive laws themselves require refinement, particularly through the incorporation of more sophisticated latent hardening models. The slip flow rule also

needs improvement, specifically by explicitly accounting for slip activity in both parent and twinned grains. Additionally, investigating discrete twin models or phase-field approaches would provide a more physically accurate representation of twin evolution.

The robustness of the model should also be tested against a broader range of experimental conditions, including different textures, higher strain rates, and elevated temperatures. Conducting tests at higher strain rates would be particularly valuable, as this would significantly increase the material's thermal output. Similarly, utilizing next-generation, high-sensitivity thermal cameras would increase the spatial or temporal resolution of the thermal signal. This enhanced temperature data would enable advanced infrared thermography analysis capable of spatially resolving heat sources. Moving beyond the current 0D energy balance equation to a full-field dissipation analysis would allow for more direct characterization of localized phenomena like twin bands, overcoming the limitations imposed by the uniform deformation assumption.

6.4. Concluding Remarks

This thesis has successfully advanced the state-of-the-art in modeling the notoriously complex behavior of magnesium alloys. By bridging the gap between mechanics and thermodynamics, this work has demonstrated that the integration of in-situ thermal measurements with a variationally consistent constitutive framework yields a model with significantly enhanced physical fidelity and predictive power. The research underscores a critical principle: for materials governed by complex, competing micro-mechanisms, a multi-physics approach is not merely beneficial, but essential for true understanding. The insights and methodologies developed herein not only deepen our knowledge of magnesium but also pave the way for the development of the next generation of predictive models for a wide range of advanced engineering materials.

REFERENCES

1. Oppedal, A., H. El Kadiri, C. Tomé, G. Kaschner, S. C. Vogel, J. Baird and M. Horstemeyer, "Effect of Dislocation Transmutation on Modeling Hardening Mechanisms by Twinning in Magnesium", *International Journal of Plasticity*, Vol. 30-31, pp. 41–61, 2012.

2. Zhang, J. and S. P. Joshi, "Phenomenological Crystal Plasticity Modeling and Detailed Micromechanical Investigations of Pure Magnesium", *Journal of the Mechanics and Physics of Solids*, Vol. 60, No. 5, pp. 945–972, 2012.

3. El Kadiri, H., C. D. Barrett, J. Wang and C. N. Tomé, "Why are $\{10\bar{1}2\}$ Twins Profuse in Magnesium?", *Acta Materialia*, Vol. 85, pp. 354–361, 2015.

4. Christian, J. W. and S. Mahajan, "Deformation Twinning", *Progress in Materials Science*, Vol. 39, No. 1, pp. 1–157, 1995.

5. Clausen, B., C. N. Tomé, D. W. Brown and S. R. Agnew, "Reorientation and Stress Relaxation Due to Twinning: Modeling and Experimental Characterization for Mg", *Acta Materialia*, Vol. 56, No. 11, pp. 2456–2468, 2008.

6. Hutchinson, J. W., "Elastic-Plastic Behaviour of Polycrystalline Metals and Composites", *Proceedings of the Royal Society of London. A. Mathematical and Physical Sciences*, Vol. 319, No. 1537, pp. 247–272, 1970.

7. Roters, F., P. Eisenlohr, L. Hantcherli, D. Tjahjanto, T. Bieler and D. Raabe, "Overview of Constitutive Laws, Kinematics, Homogenization and Multiscale Methods in Crystal Plasticity Finite-Element Modeling: Theory, Experiments, Applications", *Acta Materialia*, Vol. 58, No. 4, pp. 1152–1211, 2010.

8. Lou, X. Y., M. Li, R. K. Boger, S. R. Agnew and R. H. Wagoner, "Hardening Evolution of AZ31B Mg Sheet", *International Journal of Plasticity*, Vol. 23, No. 1,

pp. 44–86, 2007.

9. Aydıner, C. C. and M. A. Telemez, "Multiscale Deformation Heterogeneity in Twinning Magnesium Investigated with In Situ Image Correlation", *International Journal of Plasticity*, Vol. 56, pp. 203–218, 2014.

10. Kapan, E., N. Shafaghi, S. Uçar and C. C. Aydıner, "Texture-Dependent Character of Strain Heterogeneity in Magnesium AZ31 Under Reversed Loading", *Materials Science and Engineering: A*, Vol. 684, pp. 706–711, 2017.

11. Abdolvand, H. and M. R. Daymond, "Multi-Scale Modeling and Experimental Study of Twin Inception and Propagation in Hexagonal Close-Packed Materials Using a Crystal Plasticity Finite Element Approach; Part II: Local Behavior", *Journal of the Mechanics and Physics of Solids*, Vol. 61, No. 3, pp. 803–818, 2013.

12. Agnew, S. R. and O. Duygulu, "Plastic Anisotropy and the Role of Non-Basal Slip in Magnesium Alloy AZ31B", *International Journal of Plasticity*, Vol. 21, No. 6, pp. 1161–1193, 2005.

13. Cheng, J. and S. Ghosh, "Crystal Plasticity Finite Element Modeling of Discrete Twin Evolution in Polycrystalline Magnesium", *Journal of the Mechanics and Physics of Solids*, Vol. 99, pp. 512–538, 2017.

14. Hama, T., T. Suzuki, S. Hatakeyama, H. Fujimoto and H. Takuda, "Role of Twinning on the Stress and Strain Behaviors During Reverse Loading in Rolled Magnesium Alloy Sheets", *Materials Science and Engineering: A*, Vol. 725, pp. 8–18, 2018.

15. Mareau, C. and M. R. Daymond, "Micromechanical Modelling of Twinning in Polycrystalline Materials: Application to Magnesium", *International Journal of Plasticity*, Vol. 85, pp. 156–171, 2016.

16. Vidyasagar, A., A. D. Tutcuoglu and D. M. Kochmann, "Deformation Patterning

in Finite-Strain Crystal Plasticity by Spectral Homogenization with Application to Magnesium", *Computer Methods in Applied Mechanics and Engineering*, Vol. 335, pp. 584–609, 2018.

17. Wang, H., P. D. Wu, J. Wang and C. N. Tomé, "A Crystal Plasticity Model for Hexagonal Close Packed (HCP) Crystals Including Twinning and De-Twinning Mechanisms", *International Journal of Plasticity*, Vol. 49, pp. 36–52, 2013.

18. Asaro, R. J., "Crystal Plasticity", *Journal of Applied Mechanics*, Vol. 50, No. 4b, pp. 921–934, 1983.

19. Hama, T., N. Kitamura and H. Takuda, "Effect of Twinning and Detwinning on Inelastic Behavior During Unloading in a Magnesium Alloy Sheet", *Materials Science and Engineering: A*, Vol. 583, pp. 232–241, 2013.

20. Jain, A., O. Duygulu, D. W. Brown, C. N. Tomé and S. R. Agnew, "Grain Size Effects on the Tensile Properties and Deformation Mechanisms of a Magnesium Alloy, AZ31B, Sheet", *Materials Science and Engineering: A*, Vol. 486, No. 1, pp. 545–555, 2008.

21. Agnew, S., C. Tomé, D. Brown, T. Holden and S. Vogel, "Study of Slip Mechanisms in a Magnesium Alloy by Neutron Diffraction and Modeling", *Scripta Materialia*, Vol. 48, No. 8, pp. 1003–1008, 2003.

22. Agnew, S. R., D. W. Brown and C. N. Tomé, "Validating a Polycrystal Model for the Elastoplastic Response of Magnesium Alloy AZ31 Using In Situ Neutron Diffraction", *Acta Materialia*, Vol. 54, No. 18, pp. 4841–4852, 2006.

23. Muránsky, O., M. Barnett, D. Carr, S. Vogel and E. Oliver, "Investigation of Deformation Twinning in a Fine-Grained and Coarse-Grained ZM20 Mg Alloy: Combined In Situ Neutron Diffraction and Acoustic Emission", *Acta Materialia*, Vol. 58, No. 5, pp. 1503–1517, 2010.

24. Lee, S. Y., H. Wang, M. A. Gharghouri, G. Nayyeri, W. Woo, E. Shin, P. D. Wu, W. J. Poole, W. Wu and K. An, "Deformation Behavior of Solid-Solution-Strengthened Mg–9 wt.% Al Alloy: In Situ Neutron Diffraction and Elastic–Viscoplastic Self-Consistent Modeling", *Acta Materialia*, Vol. 73, pp. 139–148, 2014.

25. Wu, W., H. Qiao, K. An, X. Guo, P. Wu and P. K. Liaw, "Investigation of Deformation Dynamics in a Wrought Magnesium Alloy", *International Journal of Plasticity*, Vol. 62, pp. 105–120, 2014.

26. Wang, H., B. Clausen, L. Capolungo, I. J. Beyerlein, J. Wang and C. N. Tomé, "Stress and Strain Relaxation in Magnesium AZ31 Rolled Plate: *In-situ* Neutron Measurement and Elastic Viscoplastic Polycrystal Modeling", *International Journal of Plasticity*, Vol. 79, pp. 275–292, 2016.

27. Qiao, H., M. R. Barnett and P. D. Wu, "Modeling of Twin Formation, Propagation and Growth in a Mg Single Crystal Based on Crystal Plasticity Finite Element Method", *International Journal of Plasticity*, Vol. 86, pp. 70–92, 2016.

28. Máthis, K., G. Csiszár, J. Čapek, J. Gubicza, B. Clausen, P. Lukáš, A. Vinogradov and S. R. Agnew, "Effect of the Loading Mode on the Evolution of the Deformation Mechanisms in Randomly Textured Magnesium Polycrystals – Comparison of Experimental and Modeling Results", *International Journal of Plasticity*, Vol. 72, pp. 127–150, 2015.

29. Kelley, E. and W. Hosford, "Plane-Strain Compression of Magnesium and Magnesium Alloy Crystals", *Transactions of the Metallurgical Society of AIME*, Vol. 242, No. 1, pp. 5–13, 1968.

30. Homayonifar, M. and J. Mosler, "On the Coupling of Plastic Slip and Deformation-Induced Twinning in Magnesium: A Variationally Consistent Approach Based on Energy Minimization", *International Journal of Plasticity*, Vol. 27, No. 7, pp.

983–1003, 2011.

31. Homayonifar, M. and J. Mosler, "Efficient Modeling of Microstructure Evolution in Magnesium by Energy Minimization", *International Journal of Plasticity*, Vol. 28, No. 1, pp. 1–20, 2012.

32. Mosler, J. and M. Homayonifar, "Variational Constitutive Updates for Microstructure Evolution in HCP Metals", *GAMM-Mitteilungen*, Vol. 35, No. 1, pp. 43–58, 2012.

33. Chang, Y. and D. M. Kochmann, "A Variational Constitutive Model for Slip-Twinning Interactions in HCP Metals: Application to Single- and Polycrystalline Magnesium", *International Journal of Plasticity*, Vol. 73, pp. 39–61, 2015.

34. Becker, R. and J. T. Lloyd, "A Reduced-Order Crystal Model for HCP Metals: Application to Mg", *Mechanics of Materials*, Vol. 98, pp. 98–110, 2016.

35. Hollenweger, Y. and D. M. Kochmann, "An Efficient Temperature-Dependent Crystal Plasticity Framework for Pure Magnesium with Emphasis on the Competition Between Slip and Twinning", *International Journal of Plasticity*, Vol. 159, p. 103448, 2022.

36. Ortiz, M. and L. Stainier, "The Variational Formulation of Viscoplastic Constitutive Updates", *Computer Methods in Applied Mechanics and Engineering*, Vol. 171, No. 3-4, pp. 419–444, 1999.

37. Yang, Q., L. Stainier and M. Ortiz, "A Variational Formulation of the Coupled Thermo-Mechanical Boundary-Value Problem for General Dissipative Solids", *Journal of the Mechanics and Physics of Solids*, Vol. 54, No. 2, pp. 401–424, 2006.

38. Stainier, L., "A Variational Approach to Modeling Coupled Thermo-Mechanical Nonlinear Dissipative Behaviors", *Advances in Applied Mechanics*, Vol. 46, pp. 69–126, Elsevier, 2013.

39. Stainier, L. and M. Ortiz, "Study and Validation of a Variational Theory of Thermo-Mechanical Coupling in Finite Visco-Plasticity", *International Journal of Solids and Structures*, Vol. 47, No. 5, pp. 705–715, 2010.

40. Bartels, A., T. Bartel, M. Canadija and J. Mosler, "On the Thermomechanical Coupling in Dissipative Materials: A Variational Approach for Generalized Standard Materials", *Journal of the Mechanics and Physics of Solids*, Vol. 82, pp. 218–234, 2015.

41. Taylor, G., "Plastic Strain in Metals", *J. Inst. Met.*, Vol. 62, pp. 307–324, 1938.

42. Kleiner, S. and P. Uggowitzer, "Mechanical Anisotropy of Extruded Mg–6% Al–1% Zn Alloy", *Materials Science and Engineering: A*, Vol. 379, No. 1-2, pp. 258–263, 2004.

43. Lee, M.-G., R. Wagoner, J. Lee, K. Chung and H. Kim, "Constitutive Modeling for Anisotropic/Asymmetric Hardening Behavior of Magnesium Alloy Sheets", *International Journal of Plasticity*, Vol. 24, No. 4, pp. 545–582, 2008.

44. Lee, S. and M. Gharghouri, "Pseudoelastic Behavior of Magnesium Alloy During Twinning-Dominated Cyclic Deformation", *Materials Science and Engineering: A*, Vol. 572, pp. 98–102, 2013.

45. Wang, F. and S. R. Agnew, "Dislocation Transmutation by Tension Twinning in Magnesium Alloy AZ31", *International Journal of Plasticity*, Vol. 81, pp. 63–86, 2016.

46. Wu, L., A. Jain, D. Brown, G. Stoica, S. Agnew, B. Clausen, D. Fielden and P. Liaw, "Twinning–Detwinning Behavior During the Strain-Controlled Low-Cycle Fatigue Testing of a Wrought Magnesium Alloy, ZK60A", *Acta Materialia*, Vol. 56, No. 4, pp. 688–695, 2008.

47. Aydıner, C. C., J. V. Bernier, B. Clausen, U. Lienert, C. N. Tomé and D. W.

Brown, "Evolution of Stress in Individual Grains and Twins in a Magnesium Alloy Aggregate", *Physical Review B*, Vol. 80, No. 2, p. 024113, 2009.

48. Drozdenko, D., J. Bohlen, S. Yi, P. Minárik, F. Chmelík and P. Dobroň, "Investigating a Twinning–Detwinning Process in Wrought Mg Alloys by the Acoustic Emission Technique", *Acta Materialia*, Vol. 110, pp. 103–113, 2016.

49. Hazeli, K., J. Cuadra, P. Vanniamparambil and A. Kontsos, "In Situ Identification of Twin-Related Bands Near Yielding in a Magnesium Alloy", *Scripta Materialia*, Vol. 68, No. 1, pp. 83–86, 2013.

50. Mo, C. and A. Kontsos, "Twinning Contributions to Strain Localizations in Magnesium Alloys", *Materials Science and Engineering: A*, Vol. 722, pp. 206–215, 2018.

51. Grédiac, M., F. Sur and B. Blaysat, "The Grid Method for In-Plane Displacement and Strain Measurement: A Review and Analysis", *Strain*, Vol. 52, No. 3, pp. 205–243, 2016.

52. Schreier, H., J.-J. Orteu and M. A. Sutton, *Image Correlation for Shape, Motion and Deformation Measurements*, Springer US, Boston, MA, 2009.

53. Anten, K. and B. Scholtes, "Formation of Macroscopic Twin Bands and Inhomogeneous Deformation During Cyclic Tension-Compression Loading of the Mg-Wrought Alloy AZ31", *Materials Science and Engineering: A*, Vol. 746, pp. 217–228, 2019.

54. Efstathiou, C., H. Sehitoglu and J. Lambros, "Multiscale Strain Measurements of Plastically Deforming Polycrystalline Titanium: Role of Deformation Heterogeneities", *International Journal of Plasticity*, Vol. 26, No. 1, pp. 93–106, 2010.

55. Chen, Z. and S. Daly, "Deformation Twin Identification in Magnesium Through Clustering and Computer Vision", *Materials Science and Engineering: A*, Vol.

736, pp. 61–75, 2018.

56. Martin, G., C. W. Sinclair and J.-H. Schmitt, "Plastic Strain Heterogeneities in an Mg–1Zn–0.5Nd Alloy", *Scripta Materialia*, Vol. 68, No. 9, pp. 695–698, 2013.

57. Orozco-Caballero, A., D. Lunt, J. D. Robson and J. a. Quinta da Fonseca, "How Magnesium Accommodates Local Deformation Incompatibility: A High-Resolution Digital Image Correlation Study", *Acta Materialia*, Vol. 133, pp. 367–379, 2017.

58. Özdür, N. A., I. B. Üçel, J. Yang and C. C. Aydıner, "Residual Intensity as a Morphological Identifier of Twinning Fields in Microscopic Image Correlation", *Experimental Mechanics*, Vol. 61, No. 3, pp. 499–514, 2021.

59. Shafaghi, N., E. Kapan and C. C. Aydıner, "Cyclic Strain Heterogeneity and Damage Formation in Rolled Magnesium Via In Situ Microscopic Image Correlation", *Experimental Mechanics*, Vol. 60, No. 6, pp. 735–751, 2020.

60. Üçel, I. B., E. Kapan, O. Türkoğlu and C. C. Aydıner, "In Situ Investigation of Strain Heterogeneity and Microstructural Shear Bands in Rolled Magnesium AZ31", *International Journal of Plasticity*, Vol. 118, pp. 233–251, 2019.

61. Githens, A., S. Ganesan, Z. Chen, J. Allison, V. Sundararaghavan and S. Daly, "Characterizing Microscale Deformation Mechanisms and Macroscopic Tensile Properties of a High Strength Magnesium Rare-Earth Alloy: A Combined Experimental and Crystal Plasticity Approach", *Acta Materialia*, Vol. 186, pp. 77–94, 2020.

62. Ghosh, S. and K. Bhattacharya, "Influence of Thermomechanical Loads on the Energetics of Precipitation in Magnesium Aluminum Alloys", *Acta Materialia*, Vol. 193, pp. 28–39, 2020.

63. Wu, P. D., X. Q. Guo, H. Qiao and D. J. Lloyd, "A Constitutive Model of Twin Nucleation, Propagation and Growth in Magnesium Crystals", *Materials Science and Engineering: A*, Vol. 625, pp. 140–145, 2015.

64. Yasi, J. A., T. Nogaret, D. R. Trinkle, Y. Qi, L. G. Hector and W. A. Curtin, "Basal and Prism Dislocation Cores in Magnesium: Comparison of First-Principles and Embedded-Atom-Potential Methods Predictions", *Modelling and Simulation in Materials Science and Engineering*, Vol. 17, No. 5, p. 055012, 2009.

65. Buey, D., L. G. Hector and M. Ghazisaeidi, "Core Structure and Solute Strengthening of Second-Order Pyramidal ⟨c+a⟩ Dislocations in Mg-Y Alloys", *Acta Materialia*, Vol. 147, pp. 1–9, 2018.

66. Halphen, B. and Q. Son Nguyen, "Sur les matériaux standard généralisés", *Journal de Mécanique*, Vol. 14, pp. 39–63, 1975.

67. Stainier, L., Q. Yang and M. Ortiz, "On the Variational Formulation of Nonlinear Coupled Thermomechanical Constitutive Equations and Updates", *COMPLAS 2005,VIII International Conference on Computational Plasticity*, Barcelona, Spain, 2005.

68. Ocegueda, E. and K. Bhattacharya, "Phase-Field Modeling of Deformation Twinning and Dislocation Slip Interaction in Polycrystalline Solids", P. Maier, S. Barela, V. M. Miller and N. R. Neelameggham (Editors), *Magnesium Technology 2022*, pp. 305–313, Springer International Publishing, Cham, 2022.

69. Jain, A. and S. R. Agnew, "Modeling the Temperature Dependent Effect of Twinning on the Behavior of Magnesium Alloy AZ31B Sheet", *Materials Science and Engineering: A*, Vol. 462, No. 1, pp. 29–36, 2007.

70. Chapuis, A. and J. H. Driver, "Temperature Dependency of Slip and Twinning in Plane Strain Compressed Magnesium Single Crystals", *Acta Materialia*, Vol. 59, No. 5, pp. 1986–1994, 2011.

71. Liu, Q., A. Roy and V. V. Silberschmidt, "Temperature-Dependent Crystal-Plasticity Model for Magnesium: A Bottom-Up Approach", *Mechanics of Materials*,

Vol. 113, pp. 44–56, 2017.

72. Bong, H. J., J. Lee and M.-G. Lee, "Modeling Crystal Plasticity with an Enhanced Twinning–Detwinning Model to Simulate Cyclic Behavior of AZ31B Magnesium Alloy at Various Temperatures", *International Journal of Plasticity*, Vol. 150, p. 103190, 2022.

73. Ardeljan, M., I. J. Beyerlein, B. A. McWilliams and M. Knezevic, "Strain Rate and Temperature Sensitive Multi-Level Crystal Plasticity Model for Large Plastic Deformation Behavior: Application to AZ31 Magnesium Alloy", *International Journal of Plasticity*, Vol. 83, pp. 90–109, 2016.

74. Wang, H., P. D. Wu, C. N. Tomé and Y. Huang, "A Finite Strain Elastic–Viscoplastic Self-Consistent Model for Polycrystalline Materials", *Journal of the Mechanics and Physics of Solids*, Vol. 58, No. 4, pp. 594–612, 2010.

75. Lebensohn, R. A. and C. N. Tomé, "A Self-Consistent Anisotropic Approach for the Simulation of Plastic Deformation and Texture Development of Polycrystals: Application to Zirconium Alloys", *Acta Metallurgica et Materialia*, Vol. 41, No. 9, pp. 2611–2624, 1993.

76. Proust, G., C. N. Tomé and G. C. Kaschner, "Modeling Texture, Twinning and Hardening Evolution During Deformation of Hexagonal Materials", *Acta Materialia*, Vol. 55, No. 6, pp. 2137–2148, 2007.

77. Wang, H., B. Raeisinia, P. D. Wu, S. R. Agnew and C. N. Tomé, "Evaluation of Self-Consistent Polycrystal Plasticity Models for Magnesium Alloy AZ31B Sheet", *International Journal of Solids and Structures*, Vol. 47, No. 21, pp. 2905–2917, 2010.

78. Abdolvand, H. and M. R. Daymond, "Internal Strain and Texture Development During Twinning: Comparing Neutron Diffraction Measurements with Crystal

Plasticity Finite-Element Approaches", *Acta Materialia*, Vol. 60, No. 5, pp. 2240–2248, 2012.

79. Cheng, J., H. Jong Bong, H. Qiao, X. Hu, X. Sun, S. Ghosh and P. Wu, "Comparison of Three State-of-the-Art Crystal Plasticity Based Deformation Twinning Models for Magnesium Alloys", *Computational Materials Science*, Vol. 210, p. 111480, 2022.

80. Ardeljan, M. and M. Knezevic, "Explicit Modeling of Double Twinning in AZ31 Using Crystal Plasticity Finite Elements for Predicting the Mechanical Fields for Twin Variant Selection and Fracture Analyses", *Acta Materialia*, Vol. 157, pp. 339–354, 2018.

81. Eisenlohr, P., M. Diehl, R. A. Lebensohn and F. Roters, "A Spectral Method Solution to Crystal Elasto-Viscoplasticity at Finite Strains", *International Journal of Plasticity*, Vol. 46, pp. 37–53, 2013.

82. Lebensohn, R. A., "N-Site Modeling of a 3D Viscoplastic Polycrystal Using Fast Fourier Transform", *Acta Materialia*, Vol. 49, No. 14, pp. 2723–2737, 2001.

83. Cheng, J. and S. Ghosh, "A Crystal Plasticity FE Model for Deformation with Twin Nucleation in Magnesium Alloys", *International Journal of Plasticity*, Vol. 67, pp. 148–170, 2015.

84. Ghosh, S. and J. Cheng, "Adaptive Multi-Time-Domain Subcycling for Crystal Plasticity FE Modeling of Discrete Twin Evolution", *Computational Mechanics*, Vol. 61, No. 1-2, pp. 33–54, 2018.

85. Kalidindi, S. R., "Incorporation of Deformation Twinning in Crystal Plasticity Models", *Journal of the Mechanics and Physics of Solids*, Vol. 46, No. 2, pp. 267–290, 1998.

86. Staroselsky, A. and L. Anand, "A Constitutive Model for HCP Materials Deforming

by Slip and Twinning: Application to Magnesium Alloy AZ31B", *International Journal of Plasticity*, Vol. 19, No. 10, pp. 1843–1864, 2003.

87. Ardeljan, M., R. J. McCabe, I. J. Beyerlein and M. Knezevic, "Explicit Incorporation of Deformation Twins into Crystal Plasticity Finite Element Models", *Computer Methods in Applied Mechanics and Engineering*, Vol. 295, pp. 396–413, 2015.

88. Beyerlein, I. J. and C. N. Tomé, "A Probabilistic Twin Nucleation Model for HCP Polycrystalline Metals", *Proceedings of the Royal Society A: Mathematical, Physical and Engineering Sciences*, Vol. 466, No. 2121, pp. 2517–2544, 2010.

89. Cheng, J., X. Hu, H. Jong Bong, S. Ghosh and X. Sun, "A Finite Element Formulation for Deformation Twinning Induced Strain Localization in Polycrystal Magnesium Alloys", *Computational Materials Science*, Vol. 190, p. 110323, 2021.

90. Kasemer, M. and P. Dawson, "A Finite Element Methodology to Incorporate Kinematic Activation of Discrete Deformation Twins in a Crystal Plasticity Framework", *Computer Methods in Applied Mechanics and Engineering*, Vol. 358, p. 112653, 2020.

91. Taylor, G. I. and H. Quinney, "The Latent Energy Remaining in a Metal After Cold Working", *Proceedings of the Royal Society of London. Series A, Containing Papers of a Mathematical and Physical Character*, Vol. 143, No. 849, pp. 307–326, 1934.

92. Rittel, D., L. Zhang and S. Osovski, "The Dependence of the Taylor–Quinney Coefficient on the Dynamic Loading Mode", *Journal of the Mechanics and Physics of Solids*, Vol. 107, pp. 96–114, 2017.

93. Chrysochoos, A., "Infrared Thermography Applied to the Analysis of Material Behavior: A Brief Overview", *Quantitative InfraRed Thermography Journal*, Vol. 9,

No. 2, pp. 193–208, 2012.

94. Chrysochoos, A. and H. Louche, "An Infrared Image Processing to Analyse the Calorific Effects Accompanying Strain Localisation", *International Journal of Engineering Science*, Vol. 38, No. 16, pp. 1759–1788, 2000.

95. Benaarbia, A., A. Chrysochoos and G. Robert, "Kinetics of Stored and Dissipated Energies Associated with Cyclic Loadings of Dry Polyamide 6.6 Specimens", *Polymer Testing*, Vol. 34, pp. 155–167, 2014.

96. Chrysochoos, A. and G. Martin, "Tensile Test Microcalorimetry for Thermomechanical Behaviour Law Analysis", *Materials Science and Engineering: A*, Vol. 108, pp. 25–32, 1989.

97. Bodelot, L., L. Sabatier, E. Charkaluk and P. Dufrénoy, "Experimental Setup for Fully Coupled Kinematic and Thermal Measurements at the Microstructure Scale of an AISI 316L Steel", *Materials Science and Engineering: A*, Vol. 501, No. 1, pp. 52–60, 2009.

98. Seghir, R., E. Charkaluk, P. Dufrénoy and L. Bodelot, "Thermomechanical Couplings in Crystalline Plasticity Under Fatigue Loading", *Procedia Engineering*, Vol. 2, No. 1, pp. 1155–1164, 2010.

99. Charkaluk, E., R. Seghir, L. Bodelot, J.-F. Witz and P. Dufrénoy, "Microplasticity in Polycrystals: A Thermomechanical Experimental Perspective", *Experimental Mechanics*, Vol. 55, No. 4, pp. 741–752, 2015.

100. Guo, S., Y. Zhou, H. Zhang, Z. Yan, W. Wang, K. Sun and Y. Li, "Thermographic Analysis of the Fatigue Heating Process for AZ31B Magnesium Alloy", *Materials & Design (1980-2015)*, Vol. 65, pp. 1172–1180, 2015.

101. Wang, Z. N., H. X. Zhang, Z. F. Yan, Z. Q. Xu, X. J. Wang and W. X. Wang, "Cyclic Hardening/Softening Behaviour in AZ31B Magnesium Alloy Based on

Infrared Thermography", *Materials Science and Technology*, Vol. 33, No. 2, pp. 181–188, 2017.

102. Zhang, H. X., G. H. Wu, Z. F. Yan, S. F. Guo, P. D. Chen and W. X. Wang, "An Experimental Analysis of Fatigue Behavior of AZ31B Magnesium Alloy Welded Joint Based on Infrared Thermography", *Materials & Design*, Vol. 55, pp. 785–791, 2014.

103. Xu, Z., H. Zhang, Z. Yan, F. Liu, P. K. Liaw and W. Wang, "Three-Point-Bending Fatigue Behavior of AZ31B Magnesium Alloy Based on Infrared Thermography Technology", *International Journal of Fatigue*, Vol. 95, pp. 156–167, 2017.

104. Ghosh, D., O. T. Kingstedt and G. Ravichandran, "Plastic Work to Heat Conversion During High-Strain Rate Deformation of Mg and Mg Alloy", *Metallurgical and Materials Transactions A*, Vol. 48, No. 1, pp. 14–19, 2017.

105. Kingstedt, O. T. and J. T. Lloyd, "On the Conversion of Plastic Work to Heat in Mg Alloy AZ31B for Dislocation Slip and Twinning Deformation", *Mechanics of Materials*, Vol. 134, pp. 176–184, 2019.

106. Eisenlohr, A., I. Gutierrez-Urrutia and D. Raabe, "Adiabatic Temperature Increase Associated with Deformation Twinning and Dislocation Plasticity", *Acta Materialia*, Vol. 60, No. 9, pp. 3994–4004, 2012.

107. Cheng, J., J. Shen, R. K. Mishra and S. Ghosh, "Discrete Twin Evolution in Mg Alloys Using a Novel Crystal Plasticity Finite Element Model", *Acta Materialia*, Vol. 149, pp. 142–153, 2018.

108. Hosford, W. F., *The Mechanics of Crystals and Textured Polycrystals*, Oxford Univ. Press, New York Oxford, 1993.

109. Chang, Y., J. T. Lloyd, R. Becker and D. M. Kochmann, "Modeling Microstructure Evolution in Magnesium: Comparison of Detailed and Reduced-Order Kinematic

Models", *Mechanics of Materials*, Vol. 108, pp. 40–57, 2017.

110. Stainier, L., "Consistent Incremental Approximation of Dissipation Pseudo-Potentials in the Variational Formulation of Thermo-Mechanical Constitutive Updates", *Mechanics Research Communications*, Vol. 38, No. 4, pp. 315–319, 2011.

111. Bertsekas, D. P., "Projected Newton Methods for Optimization Problems with Simple Constraints", *SIAM Journal on Control and Optimization*, Vol. 20, No. 2, pp. 221–246, 1982.

112. Gill, P. E., W. Murray and M. H. Wright, *Practical Optimization*, Fifteenth Edition, Elsevier, Academic Press, Amsterdam Heidelberg, 2006.

113. Gill, P. E. and W. Murray, "Newton-Type Methods for Unconstrained and Linearly Constrained Optimization", *Mathematical Programming*, Vol. 7, No. 1, pp. 311–350, 1974.

114. Virtanen, P., R. Gommers, T. E. Oliphant, M. Haberland, T. Reddy, D. Cournapeau, E. Burovski, P. Peterson, W. Weckesser, J. Bright, S. J. Van Der Walt, M. Brett, J. Wilson, K. J. Millman, N. Mayorov, A. R. J. Nelson, E. Jones, R. Kern, E. Larson, C. J. Carey, I. Polat, Y. Feng, E. W. Moore, J. VanderPlas, D. Laxalde, J. Perktold, R. Cimrman, I. Henriksen, E. A. Quintero, C. R. Harris, A. M. Archibald, A. H. Ribeiro, F. Pedregosa, P. Van Mulbregt, SciPy 1.0 Contributors, A. Vijaykumar, A. P. Bardelli, A. Rothberg, A. Hilboll, A. Kloeckner, A. Scopatz, A. Lee, A. Rokem, C. N. Woods, C. Fulton, C. Masson, C. Häggström, C. Fitzgerald, D. A. Nicholson, D. R. Hagen, D. V. Pasechnik, E. Olivetti, E. Martin, E. Wieser, F. Silva, F. Lenders, F. Wilhelm, G. Young, G. A. Price, G.-L. Ingold, G. E. Allen, G. R. Lee, H. Audren, I. Probst, J. P. Dietrich, J. Silterra, J. T. Webber, J. Slavič, J. Nothman, J. Buchner, J. Kulick, J. L. Schönberger, J. V. De Miranda Cardoso, J. Reimer, J. Harrington, J. L. C. Rodríguez, J. Nunez-Iglesias, J. Kuczynski, K. Tritz, M. Thoma, M. Newville, M. Kümmerer, M. Bolingbroke, M. Tartre,

M. Pak, N. J. Smith, N. Nowaczyk, N. Shebanov, O. Pavlyk, P. A. Brodtkorb, P. Lee, R. T. McGibbon, R. Feldbauer, S. Lewis, S. Tygier, S. Sievert, S. Vigna, S. Peterson, S. More, T. Pudlik, T. Oshima, T. J. Pingel, T. P. Robitaille, T. Spura, T. R. Jones, T. Cera, T. Leslie, T. Zito, T. Krauss, U. Upadhyay, Y. O. Halchenko and Y. Vázquez-Baeza, "SciPy 1.0: Fundamental Algorithms for Scientific Computing in Python", *Nature Methods*, Vol. 17, No. 3, pp. 261–272, 2020.

115. Pan, B., "Full-Field Strain Measurement Using a Two-Dimensional Savitzky-Golay Digital Differentiator in Digital Image Correlation", *Optical Engineering*, Vol. 46, No. 3, p. 033601, 2007.

116. Pan, B., K. Li and W. Tong, "Fast, Robust and Accurate Digital Image Correlation Calculation Without Redundant Computations", *Experimental Mechanics*, Vol. 53, No. 7, pp. 1277–1289, 2013.

117. Gong, W., R. Zheng, S. Harjo, T. Kawasaki, K. Aizawa and N. Tsuji, "*In-situ* Observation of Twinning and Detwinning in AZ31 Alloy", *Journal of Magnesium and Alloys*, Vol. 10, No. 12, pp. 3418–3432, 2022.

118. Wu, P. D., X. Q. Guo, H. Qiao, S. R. Agnew, D. J. Lloyd and J. D. Embury, "On the Rapid Hardening and Exhaustion of Twinning in Magnesium Alloy", *Acta Materialia*, Vol. 122, pp. 369–377, 2017.

119. Erman, S. C., L. Stainier and C. C. Aydıner, "Guiding Severely Anisotropic Twinning Bands in Magnesium: An in Situ Investigation by Full-Field Microscopic Image Correlation", *Materials Today Communications*, Vol. 35, p. 106203, 2023.

120. Freund, L. B. and S. Suresh, *Thin Film Materials: Stress, Defect Formation and Surface Evolution*, Cambridge University Press, Cambridge, 2004.

121. Bergman, T. L., A. S. Lavine, F. P. Incropera and D. P. DeWitt, *Fundamentals of*

Heat and Mass Transfer, Seventh Edition, Wiley, Hoboken, NJ, 2011.

122. Garlea, E., M. Radovic and P. Liaw, "High-Temperature Dependency of Elastic Mechanical Behavior of Two Wrought Magnesium Alloys AZ31B and ZK60A Studied by Resonant Ultrasound Spectroscopy", *Materials Science and Engineering: A*, Vol. 758, pp. 86–95, 2019.

123. Lee, S., H. J. Ham, S. Y. Kwon, S. W. Kim and C. M. Suh, "Thermal Conductivity of Magnesium Alloys in the Temperature Range from -125 °C to 400 °C", *International Journal of Thermophysics*, Vol. 34, No. 12, pp. 2343–2350, 2013.

124. Berthel, B., A. Chrysochoos, B. Wattrisse and A. Galtier, "Infrared Image Processing for the Calorimetric Analysis of Fatigue Phenomena", *Experimental Mechanics*, Vol. 48, No. 1, pp. 79–90, 2008.

125. Quey, R., P. R. Dawson and F. Barbe, "Large-Scale 3D Random Polycrystals for the Finite Element Method: Generation, Meshing and Remeshing", *Computer Methods in Applied Mechanics and Engineering*, Vol. 200, No. 17, pp. 1729–1745, 2011.

126. Styczynski, A., C. Hartig, J. Bohlen and D. Letzig, "Cold Rolling Textures in AZ31 Wrought Magnesium Alloy", *Scripta Materialia*, Vol. 50, No. 7, pp. 943–947, 2004.

127. Moré, J. J., "The Levenberg-Marquardt Algorithm: Implementation and Theory", G. A. Watson (Editor), *Numerical Analysis*, Vol. 630, pp. 105–116, Springer Berlin Heidelberg, Berlin, Heidelberg, 1978.

128. Özdür, N. A., S. C. Erman, L. Stainier, R. Seghir and C. C. Aydıner, "Thermomechanical Couplings of Twinning Magnesium Over a Reversed Load Path", *Materials Today Communications*, Vol. 46, p. 112563, 2025.

129. Chrysochoos, A. and F. Belmahjoub, "Thermographic Analysis of Thermomechan-

ical Couplings", *Archives of Mechanics*, Vol. 44, No. 1, pp. 55–68, 1992.

130. Doudard, C., S. Calloch, F. Hild and S. Roux, "Identification of Heat Source Fields from Infrared Thermography: Determination of 'Self-Heating' in a Dual-Phase Steel by Using a Dog Bone Sample", *Mechanics of Materials*, Vol. 42, No. 1, pp. 55–62, 2010.

131. Rosakis, P., A. J. Rosakis, G. Ravichandran and J. Hodowany, "A Thermodynamic Internal Variable Model for the Partition of Plastic Work into Heat and Stored Energy in Metals", *Journal of the Mechanics and Physics of Solids*, Vol. 48, No. 3, pp. 581–607, 2000.

132. Erman, S. C. and C. C. Aydıner, "Coordinated Twinning Bands in Magnesium at the Existence of Stress Raisers via In Situ Microscopic Image Correlation", M.-T. Lin, C. Furlong, C.-H. Hwang, M. Naraghi and F. DelRio (Editors), *Advancements in Optical Methods, Digital Image Correlation & Micro-and Nanomechanics, Volume 4*, pp. 63–69, Springer International Publishing, Cham, 2023.

133. Türkoğlu, O. and C. Aydıner, "An Exploration of Grain-Averaged Stress Measurement Using Partial Unloads with In situ Microscopic Image Correlation", *Experimental Mechanics*, Vol. 64, No. 5, pp. 655–674, 2024.

134. Macdougall, D., "Determination of the Plastic Work Converted to Heat Using Radiometry", *Experimental Mechanics*, Vol. 40, No. 3, pp. 298–306, 2000.

135. Padilla, H., C. Smith, J. Lambros, A. Beaudoin and I. Robertson, "Effects of Deformation Twinning on Energy Dissipation in High Rate Deformed Zirconium", *Metallurgical and Materials Transactions A*, Vol. 38, No. 12, pp. 2916–2927, 2007.

136. Subhash, G., G. Ravichandran and B. J. Pletka, "Plastic Deformation of Hafnium Under Uniaxial Compression", *Metallurgical and Materials Transactions A*, Vol. 28, No. 7, pp. 1479–1487, 1997.

137. Wang, W., J. Liu and A. K. Soh, "Crystal Plasticity Modeling of Strain Rate and Temperature Sensitivities in Magnesium", *Acta Mechanica*, Vol. 230, No. 6, pp. 2071–2086, 2019.

138. Beyerlein, I. J., R. J. McCabe and C. N. Tomé, "Effect of Microstructure on the Nucleation of Deformation Twins in Polycrystalline High-Purity Magnesium: A Multi-Scale Modeling Study", *Journal of the Mechanics and Physics of Solids*, Vol. 59, No. 5, pp. 988–1003, 2011.

139. Abdolvand, H. and M. R. Daymond, "Multi-Scale Modeling and Experimental Study of Twin Inception and Propagation in Hexagonal Close-Packed Materials Using a Crystal Plasticity Finite Element Approach–Part I: Average Behavior", *Journal of the Mechanics and Physics of Solids*, Vol. 61, No. 3, pp. 783–802, 2013.

140. Ardeljan, M., I. J. Beyerlein and M. Knezevic, "Effect of Dislocation Density-Twin Interactions on Twin Growth in AZ31 as Revealed by Explicit Crystal Plasticity Finite Element Modeling", *International Journal of Plasticity*, Vol. 99, pp. 81–101, 2017.

141. Paudel, Y., D. Giri, M. W. Priddy, C. D. Barrett, K. Inal, M. A. Tschopp, H. Rhee and H. El Kadiri, "A Review on Capturing Twin Nucleation in Crystal Plasticity for Hexagonal Metals", *Metals*, Vol. 11, No. 9, p. 1373, 2021.

142. Maquin, F. and F. Pierron, "Heat Dissipation Measurements in Low Stress Cyclic Loading of Metallic Materials: From Internal Friction to Micro-Plasticity", *Mechanics of Materials*, Vol. 41, No. 8, pp. 928–942, 2009.

APPENDIX A: THE 0D HEAT EQUATION

This chapter details the derivation of the zero-dimensional (0D) heat equation, a simplified model for estimating the volume-averaged energy balance terms—specifically the dissipated and stored components of mechanical work—from experimental data. The formulation, adapted from seminal works [94, 129, 142] is grounded in continuum thermodynamics principles.

The derivation begins with the local forms of the first and second laws of thermodynamics governing continuous media. For quasi-static mechanical tests employed in this thesis, small strain formulation is assumed, and the kinematic description given in Equation 3.4 therefore holds.

The first law (energy conservation) states:

$$\dot{U} = \boldsymbol{\sigma} : \dot{\boldsymbol{\varepsilon}} + \rho r - \nabla \cdot \boldsymbol{q}, \tag{A.1}$$

where, U is the internal energy density. Right-hand side terms represent the sources of energy change: stress power $\boldsymbol{\sigma} : \dot{\boldsymbol{\varepsilon}}$ (work done by the Cauchy stress tensor $\boldsymbol{\sigma}$ on strain rate $\dot{\boldsymbol{\varepsilon}}$), volumetric heat supply ρr from internal sources, and conductive heat flux $-\nabla \cdot \boldsymbol{q}$, where $\boldsymbol{q}$ is the heat flux vector.

The second law (Clausius–Duhem inequality) introduces concepts of entropy and irreversibility:

$$\rho \dot{\eta} \geq \rho \frac{r}{T} - \nabla \cdot \left(\frac{\boldsymbol{q}}{T} \right), \tag{A.2}$$

where η is specific entropy and T is absolute temperature.

By introducing the Helmholtz free-energy density potential,

$$\psi = U - \rho \eta T, \tag{A.3}$$

and noting its rate form,

$$\dot{\psi} = \dot{U} - \rho \eta \dot{T} - \rho \dot{\eta} T, \tag{A.4}$$

first and second laws of thermodynamics can be combined. (The tacit assumption here is that for quasi-static loading, the material time derivative of temperature is approximated by the partial time derivative, $\frac{dT}{dt} \approx \frac{\partial T}{\partial t}$, and the convective term $\boldsymbol{v} \cdot \nabla T$ is neglected.) The Clausius–Duhem inequality can then be rewritten to define the total dissipation $\mathcal{D}$:

$$\mathcal{D} = \boldsymbol{\sigma} : \dot{\boldsymbol{\varepsilon}} - \dot{\psi} - \rho\eta\dot{T} - \frac{\boldsymbol{q} \cdot \nabla T}{T} \geq 0. \tag{A.5}$$

The total dissipation is composed of two parts: the intrinsic (or mechanical) dissipation, $\mathcal{D}_{\text{int}}$, and the thermal dissipation, $\mathcal{D}_{\text{the}}$, both of which must be strictly non-negative:

$$\mathcal{D}_{\text{int}} = \boldsymbol{\sigma} : \dot{\boldsymbol{\varepsilon}} - \dot{\psi} - \rho\eta\dot{T} \geq 0 \tag{A.6}$$

$$\mathcal{D}_{\text{the}} = -\frac{\boldsymbol{q} \cdot \nabla T}{T} \geq 0. \tag{A.7}$$

The material state is assumed to be defined by a set of observable and internal variables, $\boldsymbol{Z} = \{Z^{(k)}\}$, the free-energy density potential assumes the form $\psi = \psi(\boldsymbol{\varepsilon}, T, \boldsymbol{Z})$. Furthermore, assuming no explicit dependency of ψ on $\boldsymbol{\varepsilon}_{\text{pl}}$, meaning that ψ depends on $\boldsymbol{\varepsilon}_{\text{pl}}$ only through $\boldsymbol{Z}$, the free-energy density potential takes the form $\psi = \psi(\boldsymbol{\varepsilon}_{\text{el}}, T, \boldsymbol{Z})$.

Substituting Equation A.4 back into the first law given by Equation A.1, the general form of the local heat equation can be derived:

$$-T\frac{\partial^2\psi}{\partial T^2}\dot{T} + \nabla \cdot \boldsymbol{q} = \boldsymbol{\sigma} : \dot{\boldsymbol{\varepsilon}} - \frac{\partial\psi}{\partial\boldsymbol{\varepsilon}_{\text{el}}} : \dot{\boldsymbol{\varepsilon}}_{\text{el}} - \frac{\partial\psi}{\partial\boldsymbol{Z}} \cdot \dot{\boldsymbol{Z}} + T\frac{\partial^2\psi}{\partial T\partial\boldsymbol{\varepsilon}_{\text{el}}} \cdot \dot{\boldsymbol{\varepsilon}}_{\text{el}} + T\frac{\partial^2\psi}{\partial T\partial\boldsymbol{Z}} \cdot \dot{\boldsymbol{Z}} + \rho r. \tag{A.8}$$

Recalling the equilibrium equations given in Equation 3.11, the stress tensor $\boldsymbol{\sigma}$ and the thermodynamic forces $\boldsymbol{Y}$ associated with internal variables are said to be derived from the free-energy density potential. Further noting that $-T\frac{\partial^2\psi}{\partial T^2} = \rho C$, the heat equation can be expressed in a simpler form:

$$\rho C\dot{T} + \nabla \cdot \boldsymbol{q} = \boldsymbol{\sigma} : \dot{\boldsymbol{\varepsilon}}_{\text{pl}} + \boldsymbol{Y} \cdot \dot{\boldsymbol{Z}} + T\frac{\partial\boldsymbol{\sigma}}{\partial T} : \dot{\boldsymbol{\varepsilon}}_{\text{el}} - T\frac{\partial\boldsymbol{Y}}{\partial T} \cdot \dot{\boldsymbol{Z}} + \rho r. \tag{A.9}$$

Here, $\rho C\dot{T}$ represents heat absorption, $\nabla \cdot \boldsymbol{q}$ is heat loss due to conduction, $\mathcal{D}_{\text{int}} = \boldsymbol{\sigma} : \dot{\boldsymbol{\varepsilon}}_{\text{pl}} + \boldsymbol{Y} \cdot \dot{\boldsymbol{Z}}$ is the intrinsic dissipation, and $T\frac{\partial\boldsymbol{\sigma}}{\partial T} : \dot{\boldsymbol{\varepsilon}}_{\text{el}} - T\frac{\partial\boldsymbol{Y}}{\partial T} \cdot \dot{\boldsymbol{Z}}$ represents thermomechanical couplings. It is assumed that C remains approximately constant around the initial equilibrium temperature T_0.

In Equation A.9, volumetric heat supply ρr term can be ignored. Heat flux follows Fourier's law, $\boldsymbol{q} = -k\nabla T$, where the thermal conductivity k is assumed to be isotropic and homogeneous. Thus, $\nabla \cdot \boldsymbol{q} = -k\Delta T$. For the self-heating ranges considered in this thesis, the thermodynamic forces $\boldsymbol{Y}$ can be safely assumed to be independent of temperature, i.e., $\frac{\partial \boldsymbol{Y}}{\partial T} = 0$; so thermomechanical coupling reduces to the thermoelastic effect only.

Further defining the temperature variation from the initial state as $\theta = T - T_0$, Equation A.9 yields a more specialized form:

$$\rho C\dot{\theta} - k\Delta\theta = \mathcal{D}_{\text{int}} + T\frac{\partial \boldsymbol{\sigma}}{\partial T} : \dot{\boldsymbol{\varepsilon}}_{\text{el}}. \tag{A.10}$$

Here, Equation A.10 represents the classical heat equation for elasto-plasticity.

For linear-isotropic thermoelasticity, as defined in Equation 3.14, and noting that bulk modulus is $\kappa = 3\lambda + 2\mu$, the thermoelasic coupling term, (W_{the}, using the notation defined in Section 3.3.4) can be expressed as:

$$W_{the} = T\frac{\partial \boldsymbol{\sigma}}{\partial T} : \dot{\boldsymbol{\varepsilon}}_{\text{el}} = -3\kappa\alpha_{\text{th}}\,\text{tr}(\dot{\boldsymbol{\varepsilon}}_{\text{el}}). \tag{A.11}$$

For a uniaxial stress state, this expression further reduces to:

$$\begin{aligned} W_{the} =& -3\kappa\alpha_{\text{th}}\dot{\varepsilon}_{\text{el}} \\ =& \alpha_{\text{th}}T(\dot{\sigma} + 9\kappa\alpha_{\text{th}}\dot{\theta}). \end{aligned} \tag{A.12}$$

The transition from the general heat equation to a practical experimental tool requires addressing a fundamental challenge: obtaining accurate spatial derivatives of temperature from experimental data. In experimental practice, calculating the Laplacian term $k\Delta\theta$ from noisy thermal imaging data proves extremely challenging. The 0D approach circumvents this difficulty by averaging the heat equation over the sample's gage volume and modeling heat losses phenomenologically [94, 129].

Assuming that near thermal equilibrium conditions, both the radial thermal transfer through radiation and convection within the air, as well as the axial thermal dissipation through conduction within the specimen, can be accurately represented

using linear relationships with temperature. This results in:

$$k\Delta\theta \approx \rho C \frac{\theta}{\tau_{\text{eq}}}, \tag{A.13}$$

where τ_{eq} is a time constant that characterizes the heat losses (both conductive and convective) from the gage section.

Finally, expressing the intrinsic dissipation as a fraction of the plastic work rate, $\mathcal{D}_{\text{int}} \approx \beta\sigma\dot{\varepsilon}_p$, where β is the Taylor–Quinney coefficient, the following 0D heat equation is obtained:

$$\beta\sigma\dot{\varepsilon}_p - \alpha_{\text{th}} T(\dot{\sigma} + 9\kappa\alpha_{\text{th}}\dot{\theta}) = \rho C \left(\dot{\theta} + \frac{\theta}{\tau_{\text{eq}}}\right), \tag{A.14}$$

which is the energy balance equation (Equation 3.37) used in experimental analysis throughout this thesis.

APPENDIX B: COPYRIGHTS

All figures and illustrations in this thesis belong to the author. Visuals generated as part of this thesis, for which copyright has been transferred to the publishing house, have been included in accordance with the publisher's policy on the reuse of author-produced text and graphics, as detailed on the publisher's website.